Final Report

FDOT Contract No.: BED31-977-01
UF Contract No.: AWD12174

Use of 3D Seismic Waveform Tomography with SPT-Source for Geotechnical Site Characterization

Principal Investigators:
Khiem Tran, Ph.D.
Scott Wasman, Ph.D.

Researchers:
Bingkun Yang
Ruoyu Chen

Department of Civil and Coastal Engineering
Engineering School of Sustainable Infrastructure and Environment
University of Florida
P.O. Box 116580
Gainesville, Florida 32611-6580

Developed for the

Dino Jameson, P.E., Project Manager

March 2025

DISCLAIMER

The opinions, findings, and conclusions expressed in this publication are those of the authors and not necessarily those of the Florida Department of Transportation or the U.S. Department of Transportation.

Prepared in cooperation with the State of Florida Department of Transportation and the U.S. Department of Transportation.

SI (MODERN METRIC) CONVERSION FACTORS (from FHWA)

APPROXIMATE CONVERSIONS TO SI UNITS

SYMBOL	WHEN YOU KNOW	MULTIPLY BY	TO FIND	SYMBOL
LENGTH				
in	inches	25.4	millimeters	mm
ft	feet	0.305	meters	m
yd	yards	0.914	meters	m
mi	miles	1.61	kilometers	km

SYMBOL	WHEN YOU KNOW	MULTIPLY BY	TO FIND	SYMBOL
AREA				
in^2	square inches	645.2	square millimeters	mm^2
ft^2	square feet	0.093	square meters	m^2
yd^2	square yard	0.836	square meters	m^2
ac	acres	0.405	hectares	ha
mi^2	square miles	2.59	square kilometers	km^2

SYMBOL	WHEN YOU KNOW	MULTIPLY BY	TO FIND	SYMBOL
VOLUME				
fl oz	fluid ounces	29.57	milliliters	mL
gal	gallons	3.785	liters	L
ft^3	cubic feet	0.028	cubic meters	m^3
yd^3	cubic yards	0.765	cubic meters	m^3
NOTE: volumes greater than 1000 L shall be shown in m^3				

SYMBOL	WHEN YOU KNOW	MULTIPLY BY	TO FIND	SYMBOL
MASS				
oz	ounces	28.35	grams	g
lb	pounds	0.454	kilograms	kg
T	short tons (2000 lb)	0.907	megagrams (or "metric ton")	Mg (or "t")

SYMBOL	WHEN YOU KNOW	MULTIPLY BY	TO FIND	SYMBOL
TEMPERATURE (exact degrees)				
°F	Fahrenheit	5 (F-32)/9 or (F-32)/1.8	Celsius	°C

SYMBOL	WHEN YOU KNOW	MULTIPLY BY	TO FIND	SYMBOL
ILLUMINATION				
fc	foot-candles	10.76	lux	lx
fl	foot-Lamberts	3.426	candela/m^2	cd/m^2

SYMBOL	WHEN YOU KNOW	MULTIPLY BY	TO FIND	SYMBOL
FORCE and PRESSURE or STRESS				
Lbf*	poundforce	4.45	newtons	N
kip	kip force	1000	pounds	lbf
lbf/in^2	poundforce per square inch	6.89	kilopascals	kPa

APPROXIMATE CONVERSIONS TO SI UNITS

SYMBOL	WHEN YOU KNOW	MULTIPLY BY	TO FIND	SYMBOL
LENGTH				
mm	millimeters	0.039	inches	in
m	meters	3.28	feet	ft
m	meters	1.09	yards	yd
km	kilometers	0.621	miles	mi

SYMBOL	WHEN YOU KNOW	MULTIPLY BY	TO FIND	SYMBOL
AREA				
mm^2	square millimeters	0.0016	square inches	in^2
m^2	square meters	10.764	square feet	ft^2
m^2	square meters	1.195	square yards	yd^2
ha	hectares	2.47	acres	ac
km^2	square kilometers	0.386	square miles	mi^2

SYMBOL	WHEN YOU KNOW	MULTIPLY BY	TO FIND	SYMBOL
VOLUME				
mL	milliliters	0.034	fluid ounces	fl oz
L	liters	0.264	gallons	gal
m^3	cubic meters	35.314	cubic feet	ft^3
m^3	cubic meters	1.307	cubic yards	yd^3

SYMBOL	WHEN YOU KNOW	MULTIPLY BY	TO FIND	SYMBOL
MASS				
g	grams	0.035	ounces	oz
kg	kilograms	2.202	pounds	lb
Mg (or "t")	megagrams (or "metric ton")	1.103	short tons (2000 lb)	T

SYMBOL	WHEN YOU KNOW	MULTIPLY BY	TO FIND	SYMBOL
TEMPERATURE (exact degrees)				
°C	Celsius	1.8C+32	Fahrenheit	°F

SYMBOL	WHEN YOU KNOW	MULTIPLY BY	TO FIND	SYMBOL
ILLUMINATION				
lx	lux	0.0929	foot-candles	fc
cd/m^2	$candela/m^2$	0.2919	foot-Lamberts	fl

SYMBOL	WHEN YOU KNOW	MULTIPLY BY	TO FIND	SYMBOL
FORCE and PRESSURE or STRESS				
N	newtons	0.225	poundforce	lbf
kPa	kilopascals	0.145	poundforce per square inch	lbf/in^2

*SI is the symbol for International System of Units. Appropriate rounding should be made to comply with Section 4 of ASTM E380.
(Revised March 2003)

TECHNICAL REPORT DOCUMENTATION PAGE

1. Report No.	2. Government Accession No.	3. Recipient's Catalog No.

4. Title and Subtitle Use of 3D Seismic Waveform Tomography with SPT-Source for Geotechnical Site Characterization	5. Report Date March 2025
	6. Performing Organization Code
7. Authors Khiem Tran, Bingkun Yang, Scott Wasman, and Ruoyu Chen	8. Performing Organization Report No.
9. Performing Organization Name and Address University of Florida – Dept. of Civil and Coastal Engineering Engineering School of Sustainable Infrastructure and Environment 365 Weil Hall – P.O. Box 116580 Gainesville, FL 32611-6580	10. Work Unit No. (TRAIS)
	11. Contract or Grant No. BED31-977-01
12. Sponsoring Agency Name and Address Florida Department of Transportation 605 Suwannee Street, MS 30 Tallahassee, FL 32399	13. Type of Report and Period Covered Final Report 4/1/2022 – 03/31/2025
	14. Sponsoring Agency Code

15. Supplementary Notes

16. Abstract

The shallow subsurface across much of Florida consists of weathered, karst limestone, a spatially variable and porous stratigraphy that significantly impacts the design and load capacity of deep foundations. Therefore, obtaining detailed information on soil and rock variability is essential for safe and resilient foundation construction. Traditional invasive testing methods, such as the standard penetration test (SPT), cone penetrometer test (CPT), and coring, only sample a small volume of material near the device's tip, leaving voids or anomalies beyond boreholes undetected. To address this limitation, this project developed a novel SPT-seismic method capable of characterizing large subsurface volumes using a single SPT. The method involves recording seismic waves generated by SPT blows at depth using a 2D geophone grid on the ground surface. These signals are then analyzed via 3D full-waveform inversion (3D FWI) to produce a high-resolution 3D S-wave velocity (V_s) profile around the borehole. To validate its effectiveness, the method was tested at three Florida sites featuring karst limestone. Results demonstrated that subsurface properties were mapped in 2 ft-pixel resolution across a large 3D domain, extending up to 60 ft from the borehole to any depth reached during SPT. Multiple voids at depths of 15 to 60 ft were successfully detected and confirmed by SPT data. Additionally, the inverted V_s profiles showed strong agreement with SPT-N values across all sites. These findings highlight the SPT-seismic method as a powerful tool for geotechnical site investigations, offering high-resolution imaging with minimal invasiveness. Its ability to characterize large 3D subsurface volumes from a single SPT represents a significant advancement in site characterization, particularly for deep foundation design. Standalone GUI software for 3D SPT-seismic FWI analysis has been developed and transferred to FDOT for future applications.

17. Key Words 3D Full Waveform Inversion, SPT-seismic, Void detection, Geotechnical Site Characterization, Graphical User Interface	18. Distribution Statement No restrictions.

19. Security Classif. (of this report) Unclassified	20. Security Classif. (of this page) Unclassified	21. No. of Pages 140	22. Price

Form DOT F 1700.7 (8-72) Reproduction of completed page authorized

ACKNOWLEDGMENTS

The researchers would like to thank the Florida Department of Transportation (FDOT) for the financial support to carry out this research and the State Materials Office in Gainesville for providing access and assisting with many of the field tests.

EXECUTIVE SUMMARY

Deep site characterization at high resolution is essential for the efficient design and construction of transportation infrastructure, as unanticipated subsurface conditions can cause significant challenges during and after construction. Current FDOT practices rely on standard penetration test (SPT) data, which investigate less than 0.1% of soil and rock under a structure, leaving the spatial variability of subsurface materials—common in Florida's karst limestone—largely unresolved. This variability, including cavities, weak zones, and dipping layers, can necessitate changes in foundation type or size, particularly for large-diameter, non-redundant drilled shafts.

Non-invasive geophysical methods offer extensive subsurface coverage at a lower cost compared to invasive tests. However, surface-based seismic techniques, such as 2D and 3D full-waveform inversion (FWI), face limitations in resolution and depth. Specifically, surface-based FWI experiences a decline in resolution and accuracy with increasing depth, as the data are predominantly influenced by Rayleigh wave components that travel horizontally near the surface, with only limited contributions from body wave components at greater depths. To overcome these challenges, a novel SPT-seismic FWI technique has been introduced. This approach captures body wave energy at depth, enabling high-resolution 3D imaging down to 150 feet, all without the need for dedicated geophysical boreholes.

The primary objective of this project was to develop a robust 3D SPT-seismic full-waveform inversion (FWI) algorithm and an accompanying graphical user interface (GUI) module for advanced geotechnical site characterization. The developed algorithm enables high-resolution 3D imaging of subsurface structures to any standard penetration test (SPT) depth, extending to 150

feet. The GUI module is designed for user-friendly applications and has been transferred to the Florida Department of Transportation (FDOT) for future site investigations.

The developed SPT-seismic method offers several significant advantages. First, in-depth seismic waveform data are acquired directly from SPT testing, eliminating the need for additional geophysical boreholes. Second, unlike surface-based seismic data dominated by surface waves, the in-depth SPT source generates rich body wave data, enabling higher resolution imaging at greater depths through multiple waveforms converging on the same spatial point. Third, this method requires a smaller test area on the ground surface compared to traditional seismic techniques, making it particularly suitable for constrained environments such as urban areas, right-of-way, or even underwater settings (e.g., using hydrophones). Additionally, standard SPT borehole testing (e.g., N-values, tube sampling, and coring) can be conducted simultaneously for verification and correlation with seismic results, ensuring comprehensive soil and rock property assessments for design purposes.

The method has been validated through field experiments at three test sites in Florida: Newberry, Bell, and Kanapaha. At each site, data acquisition involved deploying 72 vertical geophones with a resonance frequency of 4.5 Hz across a 6 × 12 grid with 10-ft spacing. Seismic energy was generated by a 140-lb SPT hammer dropped from a height of 30 inches onto the top of the SPT rod above the ground surface. The impact transferred energy to the SPT spoon at the rod’s end, functioning as an in-depth seismic source. A seismic trigger mounted on the SPT rod synchronized data recording for each hammer strike. Field results demonstrate the 3D SPT-seismic FWI method effectively resolves subsurface S-wave velocity (V_s) structures with high resolution and detects voids and anomalies of various sizes and depths. The subsurface profiles are characterized in 2 ft-pixels over a large 3D domain up to 60 ft away from the borehole to any depths reached during SPT. The inverted V_s profiles closely align with results from SPT, confirming their accuracy in identifying voids and limestone layer depths.

The SPT-seismic method's ability of characterizing soil and rock in a 3D domain around a SPT borehole is significantly important for efficient design of deep foundations. It allows using a single SPT at the center of a pile group to characterize the entire volume of materials supporting all piles in the group. The method can help reduce the cost of invasive tests, as well as minimize the risk of pile failure or collapse due to unexpected site conditions. A standalone GUI software module for the 3D SPT-seismic FWI method has been developed and transferred to FDOT for future uses in geotechnical site characterization. Applications include sinkhole investigations, assessing variable site conditions, delineating problematic soils, and correlating geophysical results with engineering parameters (SPT-N value) for foundation design.

TABLE OF CONTENTS

Page

Table of Contents

LIST OF FIGURES

Chapter 1 – INTRODUCTION

1.1 Background

Geotechnical site investigations are critical for the design and construction of foundations, which support heavy loads from superstructures like bridges, buildings, and roadways. Depending on the magnitude of the loads and the subsurface conditions, foundations may range from shallow systems near the surface to deep foundations extending over 150 feet, such as drilled shafts or pile groups. These deep foundations rely on the surrounding and underlying soil or rock for load bearing through skin friction and tip resistance. However, uncertainties in subsurface conditions, such as the presence of voids, weak zones, or variable material properties, pose significant challenges to foundation design and construction (Salgado, 2022). A void near or beneath a pile group, for instance, can lead to foundation failure or even collapse.

Subsurface conditions are typically evaluated using invasive methods like the standard penetration test (SPT), cone penetration test (CPT) or rock coring (Mahmoud, 2013; Robertson, 2016; Wazoh, 2014). While these tests provide reliable data within the borehole, they cannot detect voids or anomalies located outside the borehole. As a result, multiple invasive tests are often required for the design of large pile groups, especially at sites with high spatial variability. However, the time and costs associated with these tests can become prohibitive.

Surface-based geophysical methods, such as seismic tomography (Nolet, 1987; Rawlinson et al., 2010), electrical resistivity (ER) (Banton et al., 1997; Farooq et al., 2012), and ground-penetrating radar (GPR) (Jol, 2009; Wai-Lok Lai et al., 2018), are often employed to supplement invasive techniques by providing a broader view of subsurface conditions. Among these, seismic methods are particularly valued for their ability to derive engineering properties (e.g., S-wave and P-wave velocities, Young's modulus, and shear modulus) and achieve higher resolution with depth. Full-waveform inversion (FWI) techniques (Mirzanejad & Tran, 2019; Tran et al., 2013; Tran & Sperry, 2018) have proven effective for producing 2D and 3D velocity profiles at meter-scale resolution to depths of approximately 20 meters and for detecting shallow voids less than 10 meters deep (Mirzanejad et al., 2020b; Tran et al., 2013). Despite these advantages, surface-based methods are limited by their ability to detect deeper voids due to the attenuation of seismic energy and the dominance of Rayleigh waves near the surface. Voids located deeper than five void diameters are typically undetectable by surface-based seismic techniques.

Borehole-based seismic methods offer improved resolution and depth of investigation compared to surface-based approaches. Cross-hole seismic FWI techniques (Pratt & Shipp, 1999; Wang & Rao, 2006; Zhou & Greenhalgh, 2003) have demonstrated exceptional capabilities for characterizing materials between boreholes. However, these methods require multiple boreholes for 3D characterization, making them expensive and logistically challenging.

To address these limitations, a novel SPT-seismic method has been developed in this pro, combining the benefits of SPT testing with 3D FWI for deep site characterization (Mirzanejad et al., 2020b). In this approach, seismic wavefields are generated as the SPT hammer strikes the drill rod and sampler at various depths. These wavefields, dominated by body waves, are recorded using a 2D grid of geophones on the ground surface. Unlike surface-based sources that generate predominantly Rayleigh waves, the SPT-seismic method produces body waves that originate from within the rock mass and travel through deeper volumes of material before arriving at the surface. By inverting these body wave data, the method provides higher-resolution imaging and greater accuracy at depths beyond the reach of surface-based techniques.

The SPT-seismic method leverages the time-domain 3D FWI algorithm, previously developed under the FDOT-funded project BDV31-977-82. This algorithm, based on Gauss-Newton optimization (GN-FWI) (Tran et al., 2019), achieves robust convergence and detailed subsurface imaging. However, its high memory requirements (>1.0 TB of RAM) have limited its use to specialized computing systems. To overcome this challenge, the algorithm has been adapted into a hybrid time-frequency domain approach in this project. Forward wave simulations are conducted in the time domain, while inversion is performed in the frequency domain, significantly reducing memory requirements by storing data for only a few dominant frequencies. This modification allows the inversion to run on standard desktop computers, significantly reducing the memory requirements while maintaining accuracy. The algorithm has been successfully tested on synthetic datasets and further optimized and validated using field experimental data.

This SPT-seismic method enables high-resolution imaging of subsurface conditions over large volumes, detecting voids, characterizing soil and rock properties, and supporting the design of safe, efficient foundations. Its applications include sinkhole investigations, assessing variable site conditions, delineating problematic soils, and correlating geophysical results with engineering parameters for foundation design.

1.2 Motivation and outline of the study

For advanced geotechnical site characterization, we have developed a 3D SPT-seismic full-waveform inversion (FWI) method that integrates SPT testing with advanced seismic imaging. The seismic waves generated by the SPT hammer impact are used as in-depth sources, producing body waves that travel through the subsurface and are recorded by surface geophones (Tran et al., 2024). Unlike surface-based methods, which are dominated by surface waves and have limited resolution at depth, this approach leverages body waves originating from various depths, enabling accurate imaging of subsurface structures over large volumes. This method significantly reduces the need for multiple boreholes and overcomes the depth limitations of traditional surface-based techniques. Additionally, parametric studies and field experiments ensure the optimization of test configurations and the reliability of the method under varied geologic conditions.

The 3D SPT-seismic FWI method was first developed and validated using synthetic data (Chapter 2). Test configurations and SPT sampling intervals were subsequently analyzed to optimize both field testing and data processing strategies (Chapter 3). The method was then applied to field experiments conducted at three sites in Florida, with results verified against invasive tests (SPT) to ensure accuracy (Chapter 4). Finally, a user-friendly GUI software for the 3D FWI with SPT-source method was developed, along with a comprehensive user manual, to support future applications by FDOT (Chapter 5).

Chapter 2 – OPTIMIZATION OF 3D SPT- SEISMIC FWI COMPUTATIONAL ALGORITHM (TASK 1)

2.1 Introduction

This task focuses on enhancing the time-domain 3D FWI algorithm (previously developed under the FDOT-funded project BDV31-977-82) to make it compatible with regular desktop computers. To address the RAM limitations, the algorithm has been transformed from a purely time-domain approach into a hybrid time-frequency domain framework. In this approach, forward wave simulations are performed in the time domain, while the inversion process is carried out in the frequency domain. By storing data for only a few dominant frequencies, rather than thousands of time steps, the required memory is significantly reduced. This method assumes that a limited number of key frequency components can effectively represent the waveforms across the filtered frequency bandwidth. The newly developed time-frequency 3D FWI algorithm has been successfully tested using synthetic datasets based on realistic soil and rock profiles containing embedded voids.

2.2 3D Seismic-SPT FWI algorithm

The 3D FWI method has been enhanced to utilize the advantages of a hybrid time-frequency domain approach. Forward wave simulations are performed in the time domain, enabling the simultaneous generation of wavefields at multiple frequencies without requiring an inverse matrix solver. The inversion process is then carried out using only a few selected dominant frequencies, significantly reducing the required computer memory (RAM).

2.2.1 Forward simulation in time domain

Three-dimensional elastic wave propagation is modelled by a set of the first-order linear partial differential equations for isotropic materials (Equations 2-1 to 2-9). The first three equations govern the particle velocity vector, and the remaining equations govern the stress tensor:

$$\dot{v_x} = \frac{1}{\rho}\left(\frac{\partial \sigma_{xx}}{\partial x} + \frac{\partial \sigma_{xy}}{\partial y} + \frac{\partial \sigma_{xz}}{\partial z}\right) + f_x \tag{2-1}$$

$$\dot{v_y} = \frac{1}{\rho}\left(\frac{\partial \sigma_{xy}}{\partial x} + \frac{\partial \sigma_{yy}}{\partial y} + \frac{\partial \sigma_{yz}}{\partial z}\right) + f_y \tag{2-2}$$

$$\dot{v_z} = \frac{1}{\rho}\left(\frac{\partial \sigma_{xz}}{\partial x} + \frac{\partial \sigma_{yz}}{\partial y} + \frac{\partial \sigma_{zz}}{\partial z}\right) + f_z \tag{2-3}$$

$$\dot{\sigma}_{\mathrm{xx}} = (\lambda + 2\mu)\frac{\partial v_x}{\partial x} + \lambda\left(\frac{\partial v_y}{\partial y} + \frac{\partial v_z}{\partial z}\right) \tag{2-4}$$

$$\dot{\sigma}_{yy} = (\lambda + 2\mu)\frac{\partial v_y}{\partial y} + \lambda\left(\frac{\partial v_x}{\partial x} + \frac{\partial v_z}{\partial z}\right) \tag{2-5}$$

$$\dot{\sigma}_{zz} = (\lambda + 2\mu)\frac{\partial v_z}{\partial z} + \lambda\left(\frac{\partial v_x}{\partial x} + \frac{\partial v_y}{\partial y}\right) \tag{2-6}$$

$$\dot{\sigma}_{\mathrm{xy}} = \mu\left(\frac{\partial v_x}{\partial y} + \frac{\partial v_y}{\partial x}\right) \tag{2-7}$$

$$\dot{\sigma}_{\mathrm{xz}} = \mu\left(\frac{\partial v_x}{\partial z} + \frac{\partial v_z}{\partial x}\right) \tag{2-8}$$

$$\dot{\sigma}_{\mathrm{yz}} = \mu\left(\frac{\partial v_y}{\partial z} + \frac{\partial v_z}{\partial y}\right) \tag{2-9}$$

Where the over-dot denotes the time derivative, (v_x, v_y, v_z) is the particle velocity vector, (f_x, f_y, f_z) is the body force vector, $(\sigma_{xx}, \sigma_{yy}, \sigma_{zz}, \sigma_{xy}, \sigma_{xz}, \sigma_{yz})$ is the stress tensor, ρ is the mass density and μ, λ are Lamé's coefficients. Lamé's coefficients are calculated from S-wave and P-wave velocities (V_s and V_p) as:

$$\lambda = \rho V_P^2 - 2\rho V_s^2,\ \mu = \rho V_s^2 \tag{2-10}$$

Derivatives are discretized by using center finite differences. Assuming the equations are verified at the nodes, discretization leads to a velocity-stress staggered-grid as shown in Figure 2.1. The advantages of this technique include: (i) source insertion can be expressed by velocity or stress; (ii) a stable and accurate representation for a planar free-surface boundary is easily implemented; (iii) the algorithm can be conveniently implemented on scalar, vector, or parallel computers; (iv) signal filtering and boundary truncation can be implemented with minimum effort; and (v) wavefields at multiple frequencies can be generated simultaneously in the time-domain.

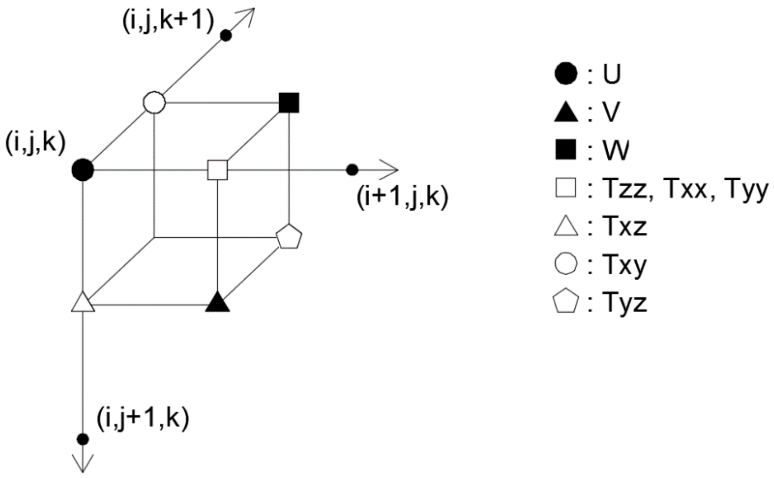

Figure 2.1. Staggered 3-D grid

With each time step, stresses and velocities are updated to simulate wave propagation. This is done by converting Equations 2-1 to 2-9 into their finite difference forms (Equations 2-11 through 2-19). The explicit numerical scheme for calculating velocities and stresses is as follows:

$$\begin{aligned} U^{n+\frac{1}{2}}_{i,j,k} = U^{n-\frac{1}{2}}_{i,j,k} &+ B_{i,j,k}\frac{\Delta t}{\Delta x}\left(Txx^{n}_{i+\frac{1}{2},j,k} - Txx^{n}_{i-\frac{1}{2},j,k}\right) \\ &+ B_{i,j,k}\frac{\Delta t}{\Delta y}\left(Txy^{n}_{i,j,k+\frac{1}{2}} - Txy^{n}_{i,j,k-\frac{1}{2}}\right) \\ &+ B_{i,j,k}\frac{\Delta t}{\Delta z}\left(Txz^{n}_{i,j+\frac{1}{2},k} - Txz^{n}_{i,j-\frac{1}{2},k}\right) \end{aligned} \tag{2-11}$$

$$\begin{aligned} V^{n+\frac{1}{2}}_{i+\frac{1}{2},j+\frac{1}{2},k} = V^{n-\frac{1}{2}}_{i+\frac{1}{2},j+\frac{1}{2},k} &+ B_{i+\frac{1}{2},j+\frac{1}{2},k}\frac{\Delta t}{\Delta x}\left(Txz^{n}_{i+1\,,j+\frac{1}{2},k} - Txz^{n}_{i,j+\frac{1}{2},k}\right) \\ &+ B_{i+\frac{1}{2},j+\frac{1}{2},k}\frac{\Delta t}{\Delta y}\left(Tyz^{n}_{i+\frac{1}{2},j+\frac{1}{2},k+\frac{1}{2}} - Tyz^{n}_{i+\frac{1}{2},j+\frac{1}{2},k-\frac{1}{2}}\right) \\ &+ B_{i+\frac{1}{2},j+\frac{1}{2},k}\frac{\Delta t}{\Delta z}\left(Tzz^{n}_{i+\frac{1}{2},j+1,k} - Tzz^{n}_{i+\frac{1}{2},j,k}\right) \end{aligned} \tag{2-12}$$

$$\begin{aligned} W^{n+\frac{1}{2}}_{i+\frac{1}{2},j,k+\frac{1}{2}} = W^{n-\frac{1}{2}}_{i+\frac{1}{2},j,k+\frac{1}{2}} &+ B_{i+\frac{1}{2},j,k+\frac{1}{2}}\frac{\Delta t}{\Delta x}\left(Txy^{n}_{i+1\,,j,k+\frac{1}{2}} - Txy^{n}_{i,j,k+\frac{1}{2}}\right) \\ &+ B_{i+\frac{1}{2},j,k+\frac{1}{2}}\frac{\Delta t}{\Delta y}\left(Tyy^{n}_{i+\frac{1}{2},j,k+1} - Tyy^{n}_{i+\frac{1}{2},j,k}\right) \\ &+ B_{i+\frac{1}{2},j,k+\frac{1}{2}}\frac{\Delta t}{\Delta z}\left(Tyz^{n}_{i+\frac{1}{2},j+\frac{1}{2},k+\frac{1}{2}} - Tyz^{n}_{i+\frac{1}{2},j-\frac{1}{2},k+\frac{1}{2}}\right) \end{aligned} \tag{2-13}$$

$$\begin{aligned} Txx^{n+1}_{i+\frac{1}{2},j,k} = Txx^{n}_{i+\frac{1}{2},j,k} &+ (L+2M)_{i+\frac{1}{2},j,k}\frac{\Delta t}{\Delta x}\left(U^{n+\frac{1}{2}}_{i+1\,,j,k} - U^{n+\frac{1}{2}}_{i,j,k}\right) \\ &+ L_{i+\frac{1}{2},j,k}\frac{\Delta t}{\Delta y}\left(W^{n+\frac{1}{2}}_{i+\frac{1}{2},j,k+\frac{1}{2}} - W^{n+\frac{1}{2}}_{i+\frac{1}{2},j,k-\frac{1}{2}}\right) \\ &+ L_{i+\frac{1}{2},j,k}\frac{\Delta t}{\Delta z}\left(V^{n+\frac{1}{2}}_{i+\frac{1}{2},j+\frac{1}{2},k} - V^{n+\frac{1}{2}}_{i+\frac{1}{2},j-\frac{1}{2},k}\right) \end{aligned} \tag{2-14}$$

$$\begin{aligned} Tyy^{n+1}_{i+\frac{1}{2},j,k} &= Tyy^{n}_{i+\frac{1}{2},j,k} + (L+2M)_{i+\frac{1}{2},j,k}\frac{\Delta t}{\Delta y}\left(W^{n+\frac{1}{2}}_{i+\frac{1}{2},j,k+\frac{1}{2}} - W^{n+\frac{1}{2}}_{i+\frac{1}{2},j,k-\frac{1}{2}}\right) \\ &\quad + L_{i+\frac{1}{2},j,k}\frac{\Delta t}{\Delta x}\left(U^{n+\frac{1}{2}}_{i+1,j,k} - U^{n+\frac{1}{2}}_{i,j,k}\right) + L_{i+\frac{1}{2},j,k}\frac{\Delta t}{\Delta z}\left(V^{n+\frac{1}{2}}_{i+\frac{1}{2},j+\frac{1}{2},k} - V^{n+\frac{1}{2}}_{i+\frac{1}{2},j-\frac{1}{2},k}\right) \end{aligned} \tag{2-15}$$

$$\begin{aligned} Tzz^{n+1}_{i+\frac{1}{2},j,k} &= Tzz^{n}_{i+\frac{1}{2},j,k} + (L+2M)_{i+\frac{1}{2},j,k}\frac{\Delta t}{\Delta z}\left(V^{n+\frac{1}{2}}_{i+\frac{1}{2},j+\frac{1}{2},k} - V^{n+\frac{1}{2}}_{i+\frac{1}{2},j-\frac{1}{2},k}\right) \\ &\quad + L_{i+\frac{1}{2},j,k}\frac{\Delta t}{\Delta x}\left(U^{n+\frac{1}{2}}_{i+1,j,k} - U^{n+\frac{1}{2}}_{i,j,k}\right) + L_{i+\frac{1}{2},j,k}\frac{\Delta t}{\Delta y}\left(W^{n+\frac{1}{2}}_{i+\frac{1}{2},j,k+\frac{1}{2}} - W^{n+\frac{1}{2}}_{i+\frac{1}{2},j,k-\frac{1}{2}}\right) \end{aligned} \tag{2-16}$$

$$\begin{aligned} Txy^{n+1}_{i,j,k+\frac{1}{2}} &= Txy^{n}_{i,j,k+\frac{1}{2}} + M_{i,j,k+\frac{1}{2}}\frac{\Delta t}{\Delta y}\left(U^{n+\frac{1}{2}}_{i,j,k+1} - U^{n+\frac{1}{2}}_{i,j,k}\right) \\ &\quad + M_{i,j,k+\frac{1}{2}}\frac{\Delta t}{\Delta x}\left(W^{n+\frac{1}{2}}_{i+\frac{1}{2},j,k+\frac{1}{2}} - W^{n+\frac{1}{2}}_{i-\frac{1}{2},j,k+\frac{1}{2}}\right) \end{aligned} \tag{2-17}$$

$$\begin{aligned} Txz^{n+1}_{i,j+\frac{1}{2},k} &= Txz^{n}_{i,j+\frac{1}{2},k} + M_{i,j+\frac{1}{2},k}\frac{\Delta t}{\Delta z}\left(U^{n+\frac{1}{2}}_{i,j+1,k} - U^{n+\frac{1}{2}}_{i,j,k}\right) \\ &\quad + M_{i,j+\frac{1}{2},k}\frac{\Delta t}{\Delta x}\left(V^{n+\frac{1}{2}}_{i+\frac{1}{2},j+\frac{1}{2},k} - V^{n+\frac{1}{2}}_{i-\frac{1}{2},j+\frac{1}{2},k}\right) \end{aligned} \tag{2-18}$$

$$\begin{aligned} Tyz^{n+1}_{i+\frac{1}{2},j+\frac{1}{2},k+\frac{1}{2}} &= Tyz^{n}_{i+\frac{1}{2},j+\frac{1}{2},k+\frac{1}{2}} + M_{i+\frac{1}{2},j+\frac{1}{2},k+\frac{1}{2}}\frac{\Delta t}{\Delta z}\left(W^{n+\frac{1}{2}}_{i+\frac{1}{2},j+1,k+\frac{1}{2}} - W^{n+\frac{1}{2}}_{i+\frac{1}{2},j,k+\frac{1}{2}}\right) \\ &\quad + M_{i+\frac{1}{2},j+\frac{1}{2},k+\frac{1}{2}}\frac{\Delta t}{\Delta y}\left(V^{n+\frac{1}{2}}_{i+\frac{1}{2},j+\frac{1}{2},k+1} - V^{n+\frac{1}{2}}_{i+\frac{1}{2},j+\frac{1}{2},k}\right) \end{aligned} \tag{2-19}$$

where i, j, k are the indicial location of the current point in the x, z, and y directions, respectively; n represents the current time step while $U, V,$ and W are the particle velocities in the x, z, and y directions (v_x, v_y, v_z). B is the reciprocal of the density at the location indicated by the indices and T represent the stress component (e.g., $\sigma_{xx}, \sigma_{yy}, \sigma_{zz}, \sigma_{xy}, \sigma_{xz}, \sigma_{yz}$) in each direction. M and L are the Lame's coefficients mentioned earlier.

In order to maintain stability of the simulation, the time interval (sampling rate) Δt must satisfy the Courant-Friedrichs-Levy (CFL) stability criterion. The numerical stability condition for this explicit scheme is:

$$v_{\max} \Delta t \sqrt{\frac{1}{\Delta x^2 + \Delta y^2 + \Delta z^2}} \leq 1 \tag{2-20}$$

Where v_{max} is the maximum P-wave velocity of the medium, and Δx, Δy and Δz is the grid spacing selected to satisfy at least ten points per minimum expected wavelength to avoid numerical dispersion or:

$$\Delta\mathrm{x}, \Delta\mathrm{y}, \Delta\mathrm{z} \ \leq \mathrm{dh} = \frac{\lambda_{min}}{10} \tag{2-21}$$

Where $\lambda_{min} = \frac{v_{ave}}{f_{max}}$, v_{ave} is the average S-wave velocity in the media, f_{max} is the maximum frequency of the source. During inversion, Δt is allowed to change due to different v_{max} values, which ensures that the measured wave fields are interpolated to the same sampling rate for comparison to the estimated wave fields at every iteration. Note, using a fixed small sampling rate will maintain stability of the simulation through iterations, but it will increase the required computing time.

Special conditions are required at the boundaries of the modeled domain when simulating wave propagation with finite difference equations. A model without boundary conditions will have boundaries that act like rigid walls, i.e., all incoming waves will be reflect off of the boundary back into the domain. These reflections do not accurately represent the infinite media, from which data is collected in the field. An ideal model will allow the wave to pass through the boundary without any reflection. For the domain, a free-surface boundary condition is applied on the top boundary (surface), while perfectly matched layers (PML) (Komatitsch & Martin, 2007) are applied at the other boundaries (i.e., sides and bottom). The PML attenuates any waves near the boundary and the dampening effect is carried out by extending the staggered grid beyond the modelled domain.

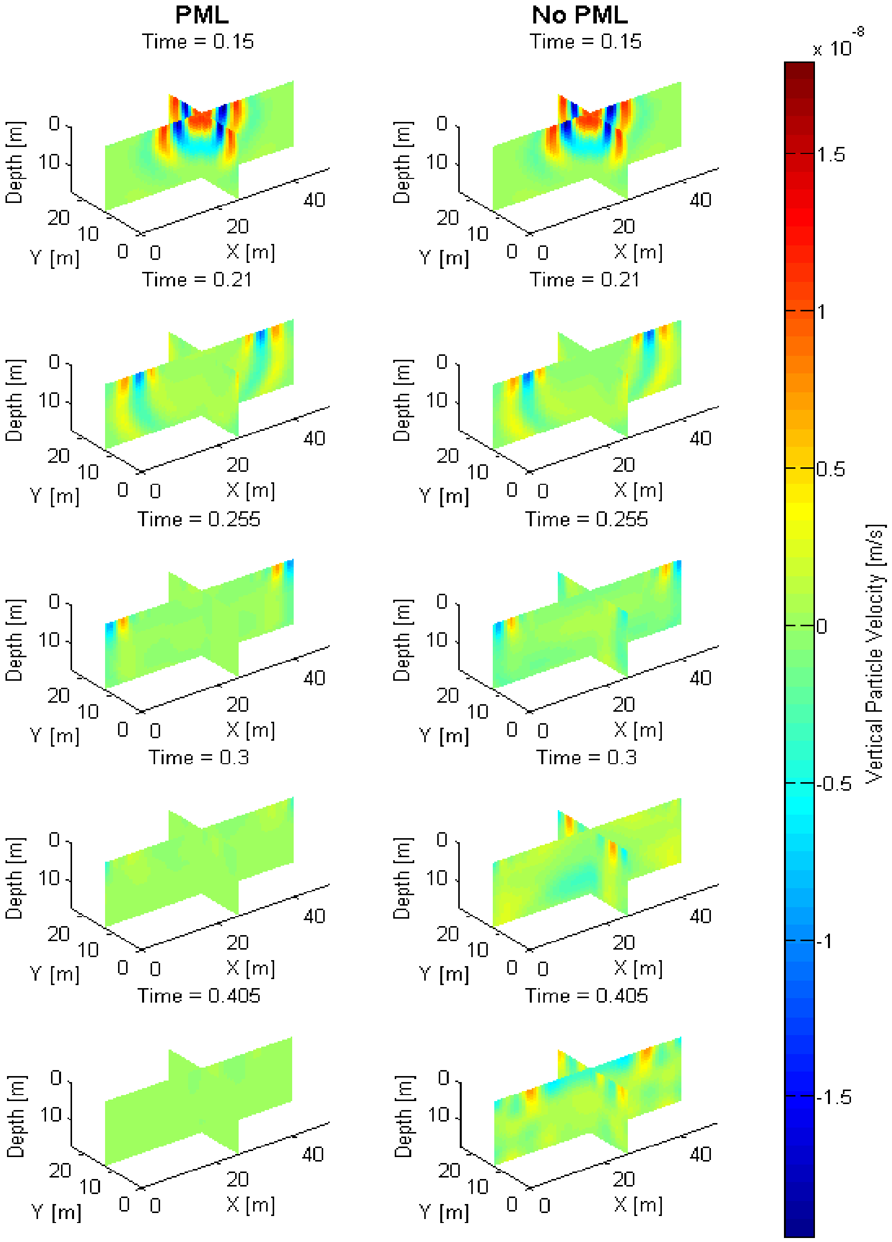

Figure 2.2. 3D wave propagation with and without the perfectly matched layer (PML) boundary truncation

As an example, Figure 2.2 shows 3D wave propagation in a homogeneous medium with (left) and without (right) the PML conditions. The source is located on the free surface (depth z = 0). With the implementation of the PML, almost no reflected signals from boundaries are observed (Figure 2.2, left column), whereas large, reflected signals from boundaries are seen after 0.3 s (Figure 2.2, right column) without the PML.

2.2.2 Gauss-Newton inversion in frequency-domain

To save computer RAM, the inversion is conducted in the frequency-domain. Time-domain wavefields and Jacobian elements obtained from the forward wave simulation (one shot at a time) are converted into the frequency-domain. The time-domain components are replaced by those from the next shot simulation. The frequency-domain components (wavefields and Jacobian matrix) are stored for all shots at only three frequencies, instead of thousands of time steps. This reduces the required RAM by about 90%. Using the approach of Butzer et al., (2013) based on the discrete Fourier transformation, signals are converted from the time domain to frequency domain as:

$$\tilde{u}(\mathbf{x},\omega) = \sum_{l=1}^{nt} \exp(\sqrt{-1}\omega l\Delta t) u(\mathbf{x}, l\Delta t)\Delta t \tag{2-22}$$

where $\tilde{u}(x,\omega)$ is the frequency-domain signal for the sampled location x = (x, y, z) and frequency ω, u(x, lΔt) is the time domain signal and time t = lΔt, Δt is the time sampling, and nt is the number of time steps. Each sampled location x is a receiver for wavefield or cells for Jacobian components. Equation 2-22 is used for all signals (estimated and measured wavefields, Jacobian matrix elements) in following Equations 2-23 to 2-25. Both real and imaginary components of the transformed signals are used. It is noted that $\tilde{u}(x, \omega)$ is the sum of time-domain data over time (e.g., stacking to improve signals), and thus it allows to analyze several SPT-blows at a similar depth (in case of low energy signals emitted from deep rock).

The optimization method minimizes the residual between estimated and observed (measured) waveform data, which is defined as:

$$\Delta\tilde{\boldsymbol{d}}_{s,r}=\tilde{\boldsymbol{F}}_{s,r}(m)-\tilde{\boldsymbol{d}}_{s,r} \tag{2-23}$$

where s and r denote the shot and receiver numbers, respectively. The vector $\tilde{\boldsymbol{F}}_{s,r}(m)$ is the frequency-domain estimated data associated with the model m (V_s and V_p of all cells), and obtained from the forward simulation. The vector $\tilde{\boldsymbol{d}}_{s,r}(m)$ is the frequency-domain observed waveform data for field testing.

The least-squares error E(m) is used for minimization of the residual as:

$$E(m)=\frac{1}{2}\left\|\Delta\tilde{\boldsymbol{d}}\right\|^2=\frac{1}{2}\Delta\tilde{\boldsymbol{d}}^t\Delta\tilde{\boldsymbol{d}}, \text{ and } \Delta\tilde{\boldsymbol{d}}=\left\{\Delta\tilde{\boldsymbol{d}}_{s,r}, s=1..NS, r=1\ldots NR\right\} \tag{2-24}$$

where t denotes the matrix transpose, NS and NR are shot and receiver numbers, respectively. $\Delta\tilde{\boldsymbol{d}}$ is the residual for all shots and receivers, which are placed in a 2-D uniform grid on the ground surface. The size of the vector $\Delta\tilde{\boldsymbol{d}}_{s,r}$ is 2 ×NF × NS × NR, where NF is the number of frequencies. The factor of 2 is for the real and imaginary components for each frequency.

By minimizing the error E(m), the model m at iteration (n+1) is updated from the previous iteration as:

$$m^{n+1}=m^n - \alpha^n\left[\tilde{J}^t\tilde{J}+\lambda_1 P^t P+\lambda_2 I^t I\right]^{-1} \tilde{J}^t\Delta\tilde{\boldsymbol{d}} \tag{2-25}$$

where the Jacobian matrix $\tilde{J}$ is the frequency-domain partial derivative wavefield with respect to individual parameters (V_s and V_p of cells). The time-domain partial derivative wavefield J is calculated based on the convolution of the virtual source with reciprocal wavefields (Tran et al., 2019) and then converted to the frequency-domain $\tilde{J}$. The number of forward simulations required for the calculation of Jacobian J is NS+NR. I is the identity matrix, and matrix P is determined via a 3D Laplacian operator with its elements of either 1, -6 or 0. Coefficients $\lambda_1$and $\lambda_2$are 0.02 and 0.0005 times of the maximum value of $\tilde{J}^t\tilde{J}$, respectively, as suggested by Tran et al. (2019). The term ($\lambda_1 P^t P + \lambda_2 I^t I$) in Equation 2-25 improves the invertibility of the approximate Hessian matrix ($Ha = \tilde{J}^t\tilde{J}$), and regularizes the inversion by constraining the model roughness (e.g., tying a cell to its six adjacent cells and larger λ_1 producing smoother models). The step length α^n is fixed at 1.0 in this study.

2.3 Results

The developed time-frequency 3D FWI algorithm of SPT-seismic data was first tested on a synthetic experiment with known V_s and V_p profiles to evaluate its accuracy, before applying to field experiments (Task 3). The synthetic experiment includes simulation of SPT-seismic data and inversion of the data to extract V_s and V_p for comparison to their true values.

2.3.1 Synthetic experiment on a small model (20.4 m × 18 m × 18 m)

The time-frequency 3D FWI algorithm of SPT-seismic data was first tested on a synthetic experiment. For this synthetic experiment, a challenging velocity model representing a variable subsurface profile with V_s of 200 m/s for the top layer and 400 m/s for the lower half space, with twice V_s for the V_p profile was used as the true model (Figure 2.3). Furthermore, a buried void of 3 m × 3.75 m × 3.75 m (depth × length × width) was placed at 15 m depth and 1.0 m away from the source line (or SPT location). It was placed to simulate a deep void that would not be found with an actual SPT. The void was assumed to be filled with air with V_s of 0 m/s and V_p of 300 m/s. A mass density of 1,800 kg/m3 is assumed for the whole medium, as a typical value for general soils.

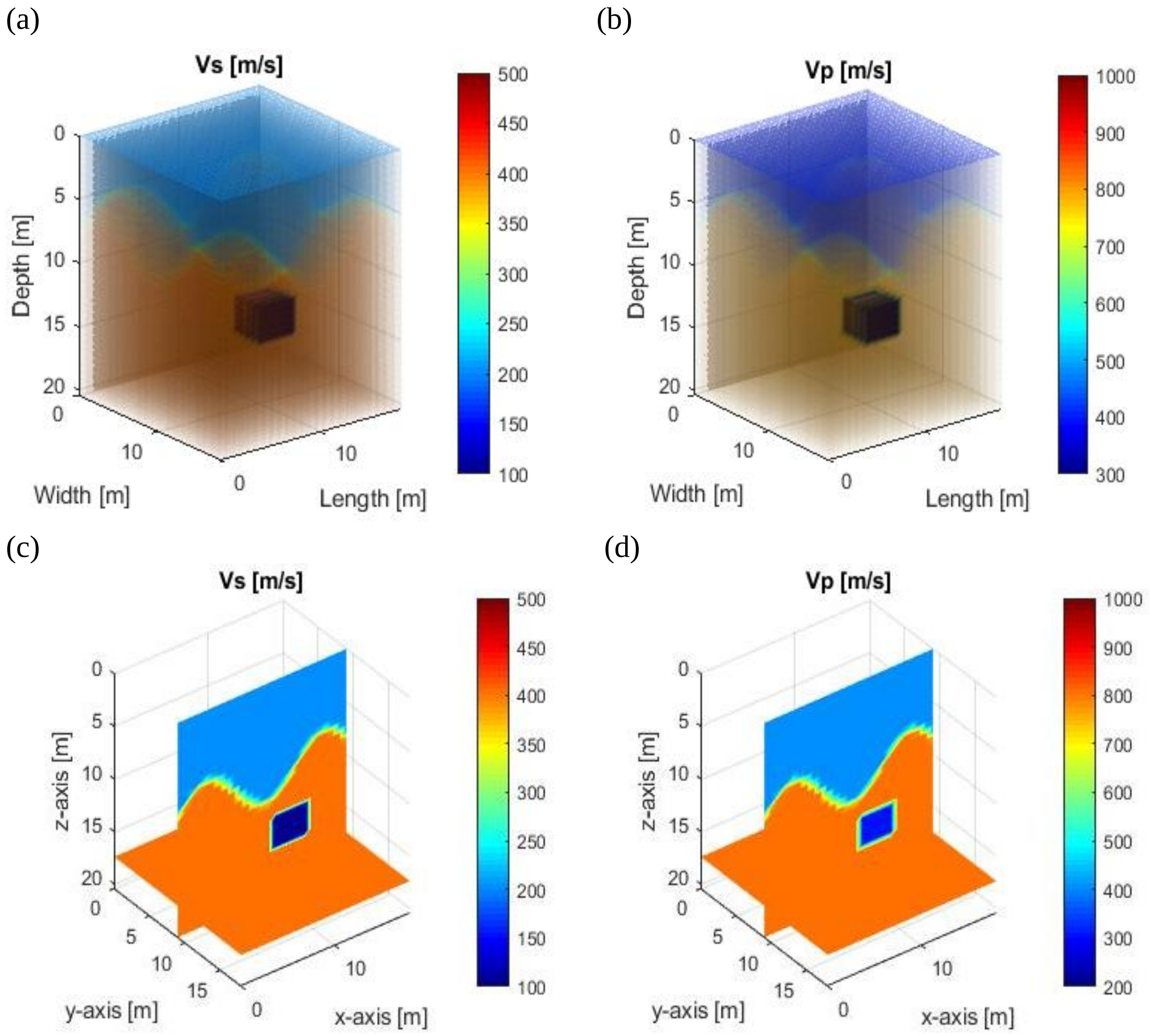

Figure 2.3. Synthetic model with a void at 15 m depth: (a) the 3D rendering V_s model; (b) the 3D rendering V_p model; (c) the 2D cross-section view of V_s model; (d) the 2D cross-section view of V_p model

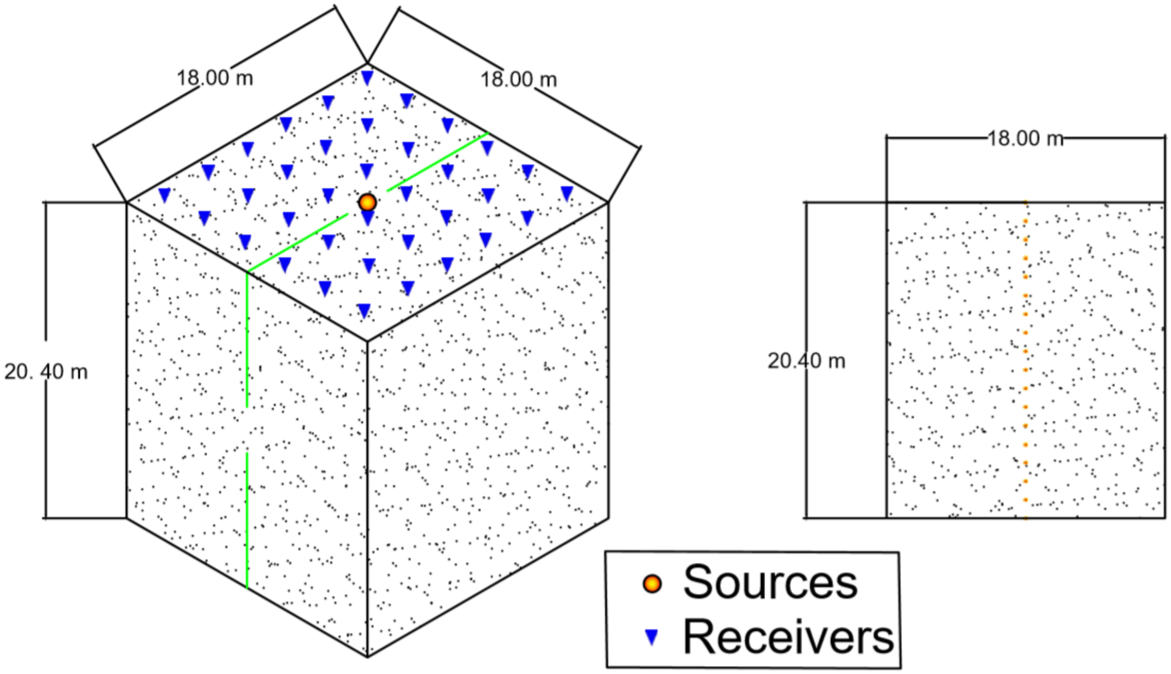

Figure 2.4. Test configuration: 36 receivers with spacing interval of 3.0 m, 18 sources with spacing interval of 1.2 m

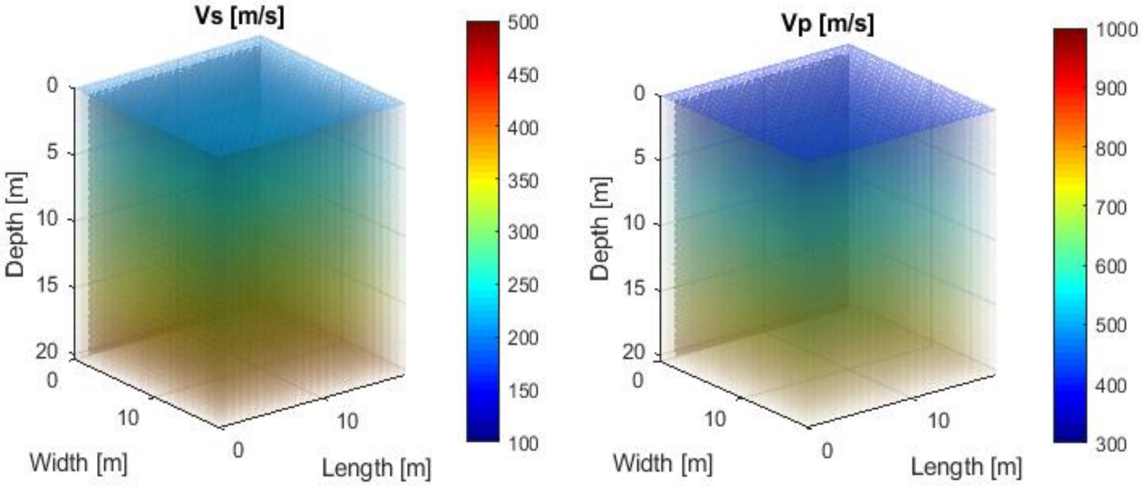

Figure 2.5. Initial model used for inversion

The test configurations are shown in Figures 2.4. A 2D array of 6 × 6 receivers at 3-m spacing (10 ft) was placed on the free surface, and a linear array of 18 sources at 1.2-m spacing was placed along a vertical line at the center. Shown in Figure 2.5 is the initial model used for inversion. A linearly increasing velocity model of 200 m/s at the ground surface to 400 m/s at the half space for the V_s and twice of that for the V_p was used as the initial model.

Two inversions were conducted in order of increasing frequency data. The first inversion began with the initial model (Figure 2.5), using data at three frequencies of 15, 20, and 25 Hz. The second inversion ran with data at three frequencies of 30, 35, and 40 Hz, using the result of the first inversion as the input velocity model. Shown in Figure 2.6 is the variation of the normalized least-squares error with iterations for both stages of frequency inversion. The error decreased continuously during the first stage from 1.0 at the start of the lower frequency stage to about 0.02 at the end of 100 iterations. The inversion algorithm was subsequently able to reduce the mismatch and reduced the error from 1.0 to 0.2 at the end of the second stage of an additional 100 iterations.

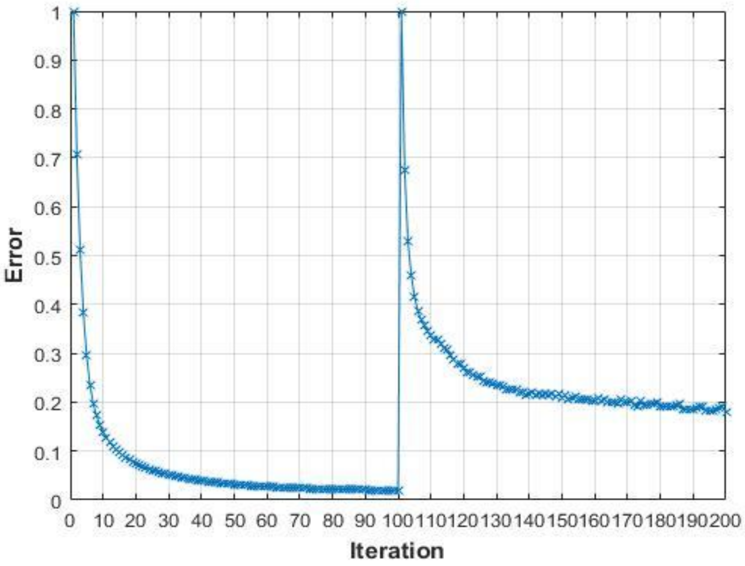

Figure 2.6. Normalized least-squares error for both runs

Shown in Fig. 2.7 is a sampled waveform comparison between the observed data from the true model and estimated data associated with the initial model and the final inverted model at iteration 200. Figure 2.7a shows the discrepancy between observed and estimated data. This is due to the fact that estimated data is computed from the initial model (Figure 2.2) with no void and layer interface. Figure 2.7b shows the excellent match between observed and estimated data, because the model is significantly updated toward the true model during inversion. The waveform match improved substantially during inversion. Phase and amplitudes are matched perfectly at the end, indicating the success of the inversion algorithm that vectored towards the global minimum.

The excellent match of observed and estimated data shows that a few dominant frequency components could well represent waveforms for the entire filtered frequency bandwidth. Matching data at 6 frequencies (15, 20, 25, 30, 35, and 40 Hz) allows matching the waveforms in the time-domain for the entire filtered bandwidth from 10 to 50 Hz. In other words, there is a lot of redundant information in the time-domain waveforms, and only a few frequencies are needed for analysis to recover the true model.

Shown in Figure 2.8 is the final inverted result. Both V_s and V_p profiles are well characterized. The existence of two separate layers is clearly observed, and the variable layer interface is well imaged. More importantly, the location and overall shape of the deep void is successfully identified. This synthetic result shows the advantage of using the in-depth source data (e.g., generated by a SPT-drill rod and spoon) for characterization of materials around the SPT boring and offline anomalies/voids.

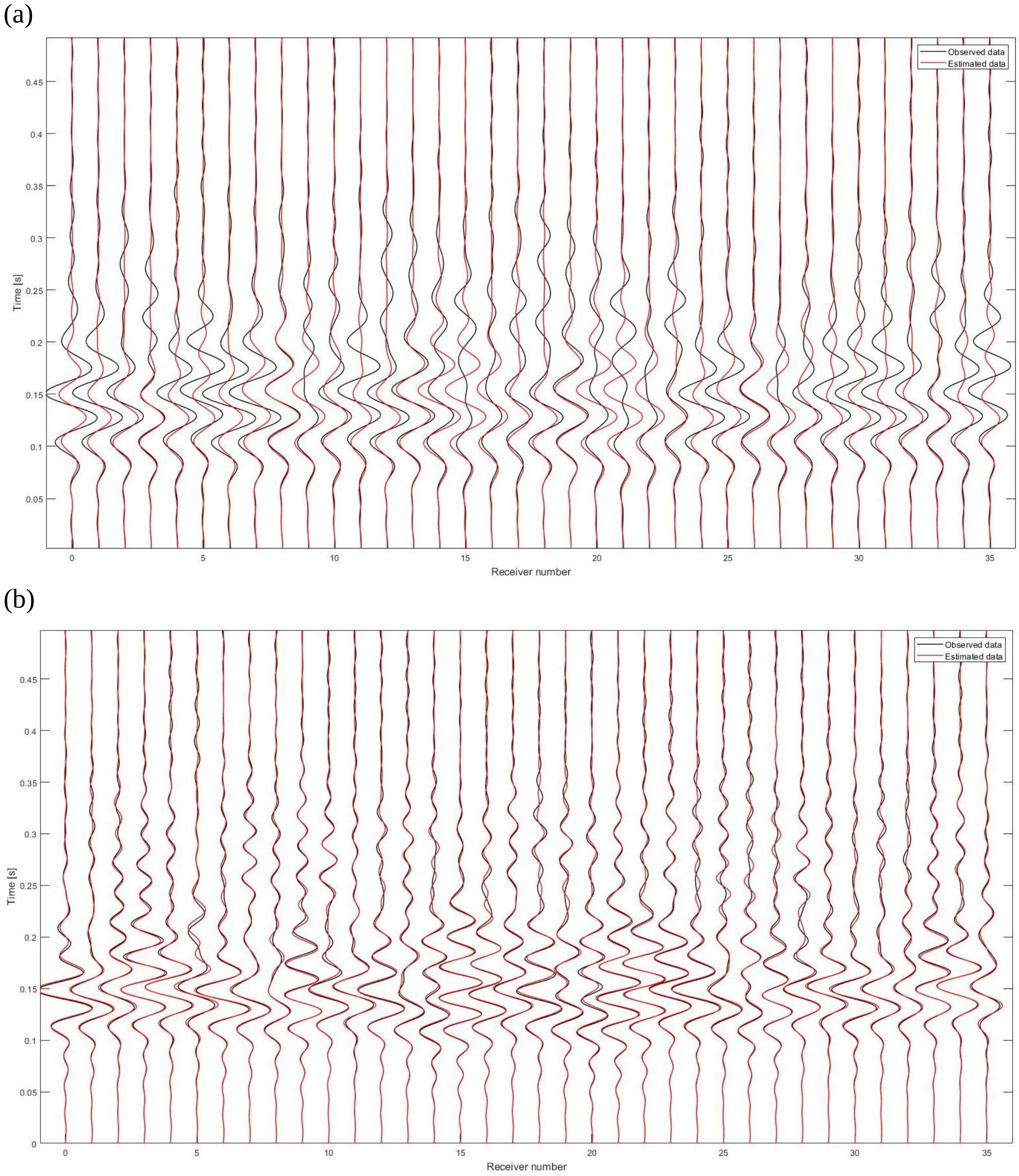

Figure 2.7. Waveform comparison for a shot at 18-m depth: (a) observed data and estimated data associated with the initial model; (b) observed data and estimated data associated with the final inverted model

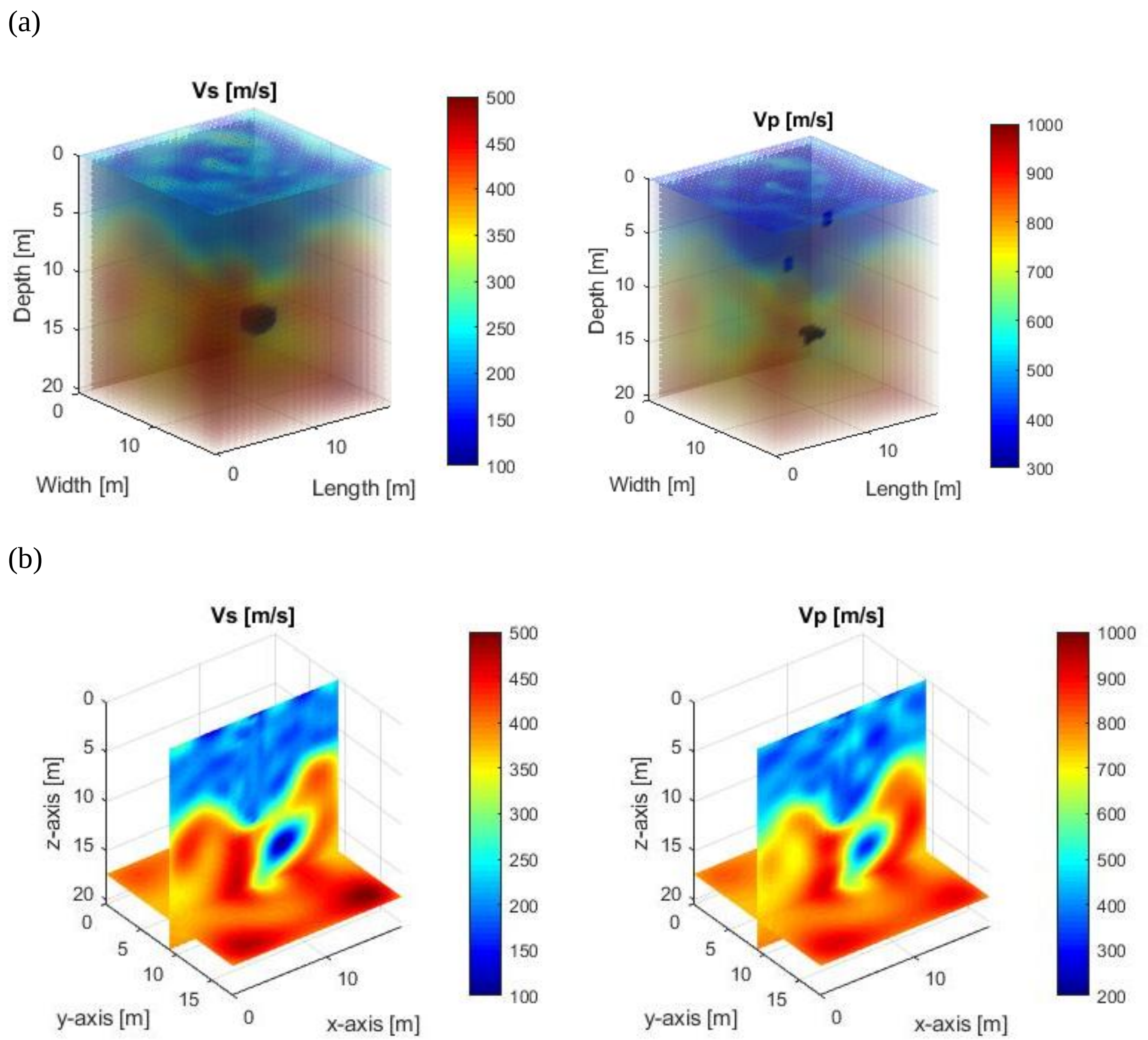

Figure 2.8. Small model: (a) 3D rendering of inverted V_s and V_p; (b) 2D cross-section view of inverted V_s and V_p

2.3.2 Synthetic experiment on a large model (30 m × 24 m × 24 m)

The 3D FWI algorithm was further tested on a large model with a deep void. For this synthetic experiment, a model of 30 m × 24 m × 24 m (depth × length × width) representing a variable subsurface profile was used as the true model (Figure 2.9). It has V_s of 200 m/s for the top layer and 400 m/s for the lower half space, with twice V_s for the V_p profile. A void of 3 m × 3.75 m × 3.75 m (height × length × width) was buried at 18 to 21 m depth and 2.5 m away from the source line. This offline void would not be found during an actual SPT. The void was assumed to be filled with air with V_s of 0 m/s and V_p of 300 m/s. A mass density of 1,800 kg/m^3 is assumed to be for the whole medium, as a typical value for general soils.

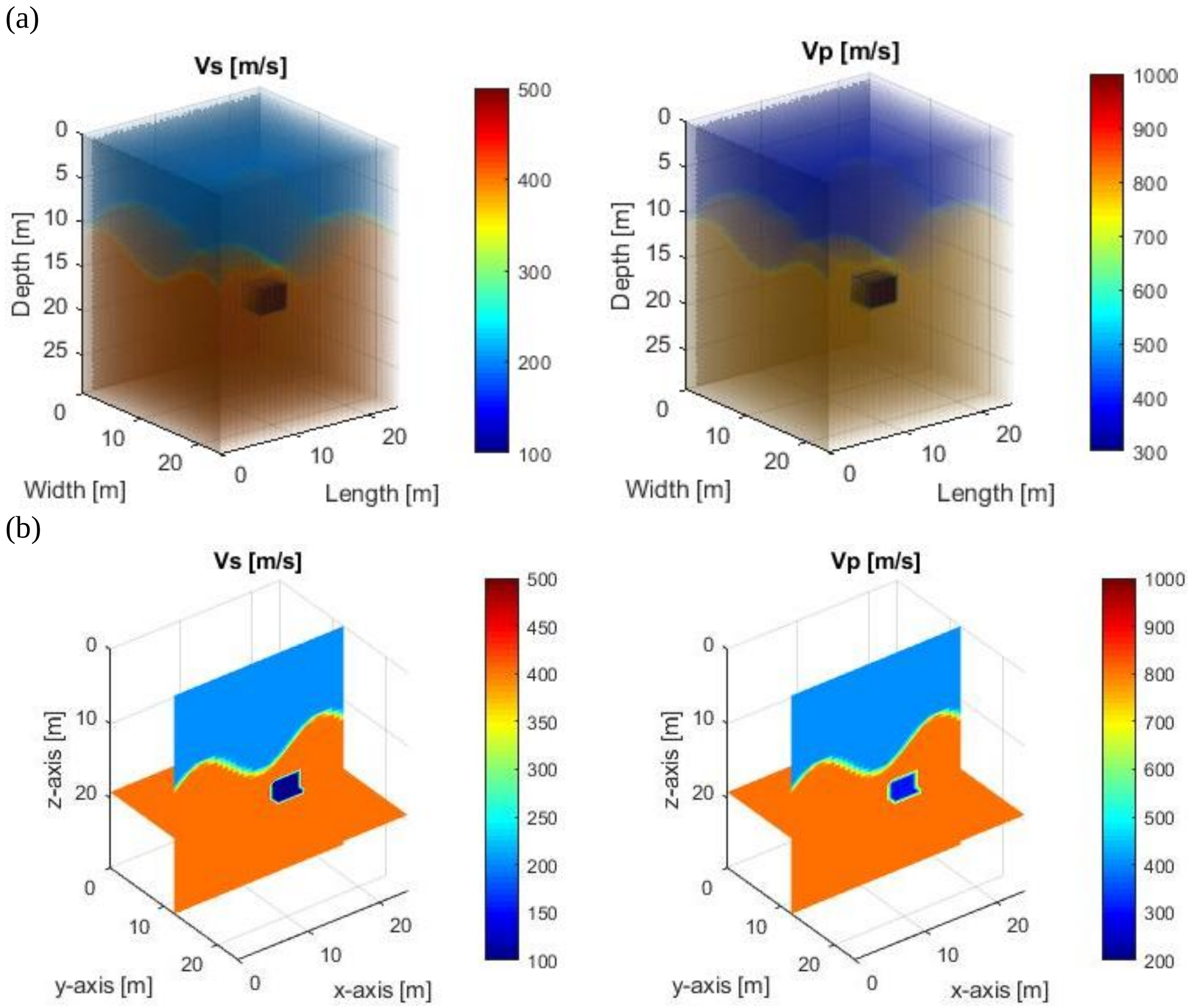

Figure 2.9. Large synthetic model with a deep void: (a) 3D rendering of true V_s and V_p; (b) 2D cross-section view of true V_s and V_p

For waveform simulation and analyses, the test configuration (Figure 2.10) consists of 64 receivers located in an 8×8 grid of 3-m spacing on the free surface, and 25 sources located from 0 to 30-m depth at 1.2-m spacing along the center line of the model. A linearly increasing velocity model of 200 m/s at the ground surface to 400 m/s at half space for the V_s and twice of that for the V_p was used as the initial model (Figure 2.11).

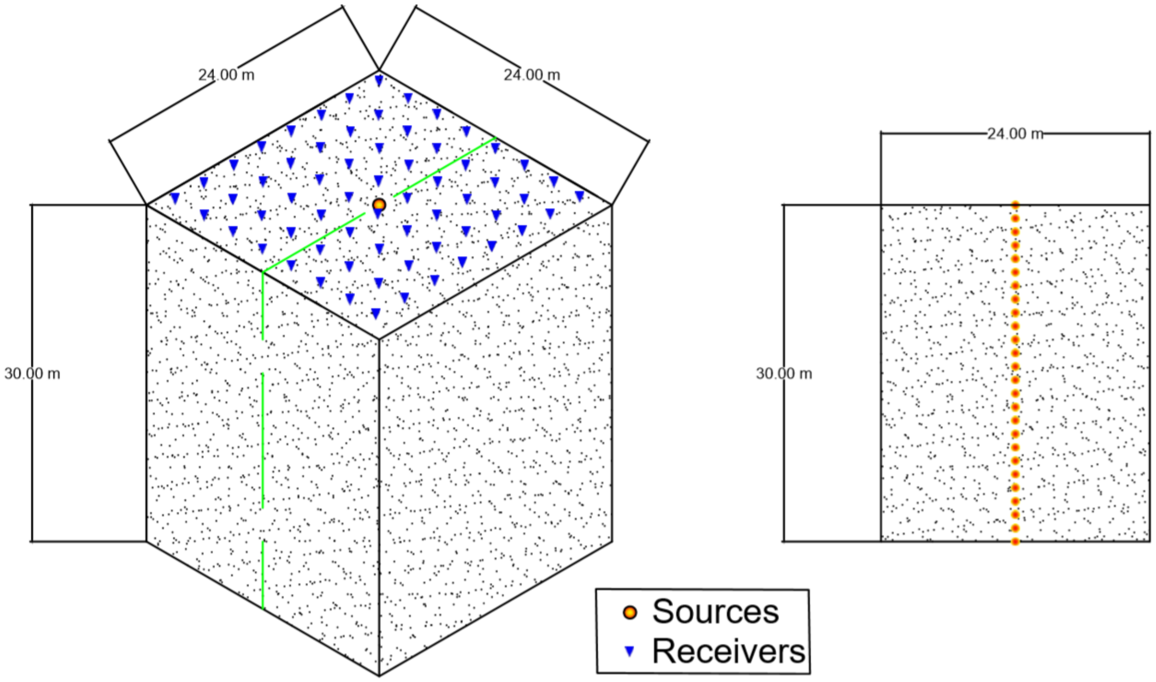

Figure 2.10. Test configuration: 64 receivers with spacing interval of 3.0 m and 25 sources with spacing interval of 1.2 m

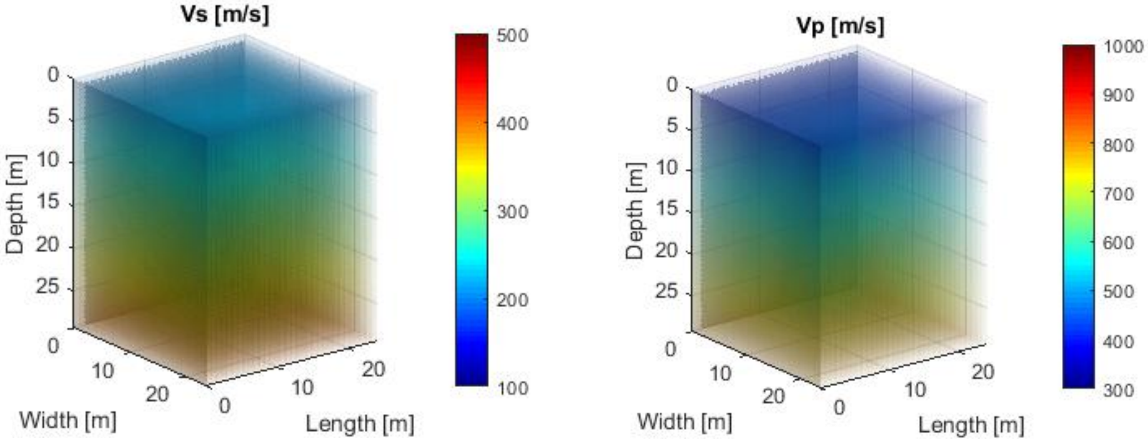

Figure 2.11. Initial model used for inversion

Same as the previous analyses, two inversions were conducted for this large model. The first inversion began with the initial model (Figure 2.11), using data at three frequencies of 15, 20 and 25 Hz. The second inversion ran with data at three frequencies of 30, 35 and 40 Hz, using the result of the first inversion as the input velocity model.

The normalized least-squares error of iterations for both stages of frequency inversion are shown in Figure 2.12. The error decreased continuously during the first stage from 1.0 at the start of the lower frequency stage to about 0.02 at the end of the first stage. The inversion algorithm was subsequently able to reduce the mismatch and reduced the error from 1.0 to 0.15 at the end of the second stage.

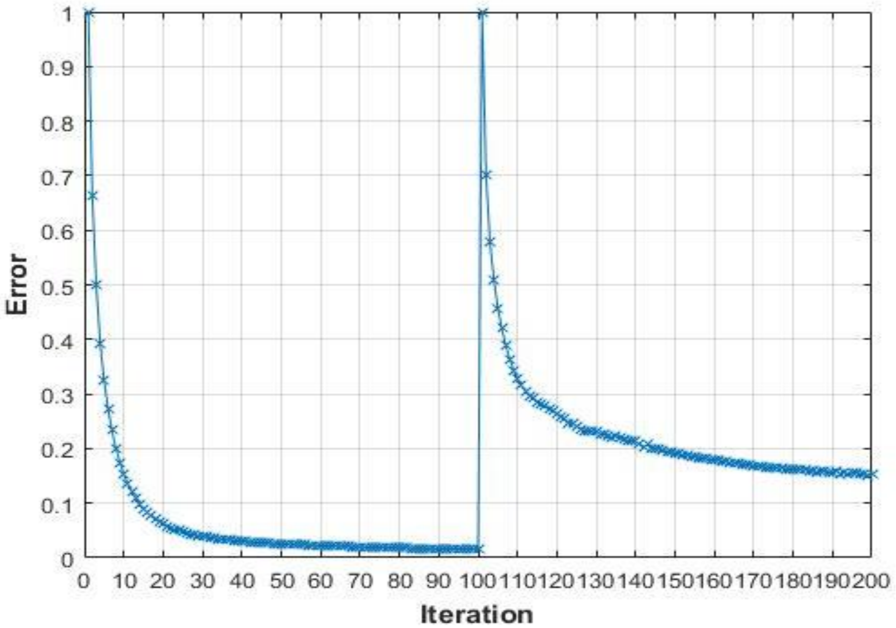

Figure 2.12. Normalized least-squares error for both inversion runs

Figure 2.13 compares the observed data from the true model and estimated data associated with the initial model and the final inverted model at iteration 200. Figure 2.13a shows the discrepancy between observed and estimated data. This is due to estimated data is computed from the initial model (Figure 2.11) with no void and layer interface. Figure 2.13b shows the excellent match between observed and estimated data, because the model is significantly updated toward the true model during inversion. The waveform match improved substantially during inversion. Phase and amplitudes are matched perfectly at the end, indicating the success of the inversion algorithm that vectored towards the global minimum. Again, the excellent match of observed and estimated data shows that a few dominant frequency components provide information for the entire frequency bandwidth.

Shown in Figure 2.14 is the final inverted result. Both V_s and V_p profiles are well characterized in 3D domain within 12 m (40 ft) around the source line (SPT boring) to 30 m depth (100 ft). The two separate layers are recovered, and the variable layer interface are accurately imaged within the entire test area of 24 m × 24 m (80 ft × 80 ft). The offline void is identified with accurate location and shape. The results show the excellent capability of the time-frequency 3D FWI algorithm for characterizing materials around the SPT boring and offline anomalies/voids.

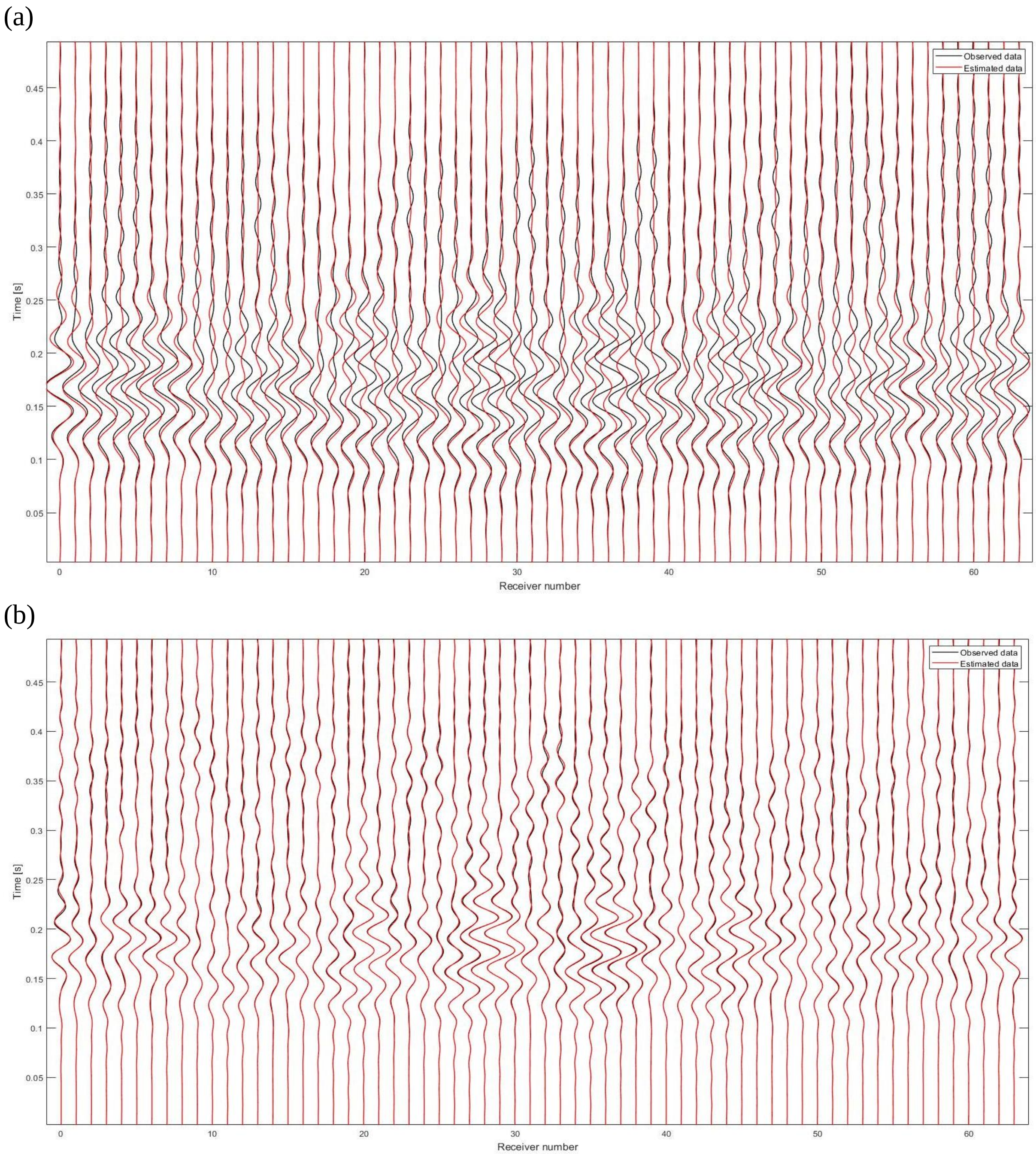

Figure 2.13. Waveform comparison for the 20th shot: (a) observed data and estimated data associated with the initial model; (b) observed data and estimated data associated with the final inverted model

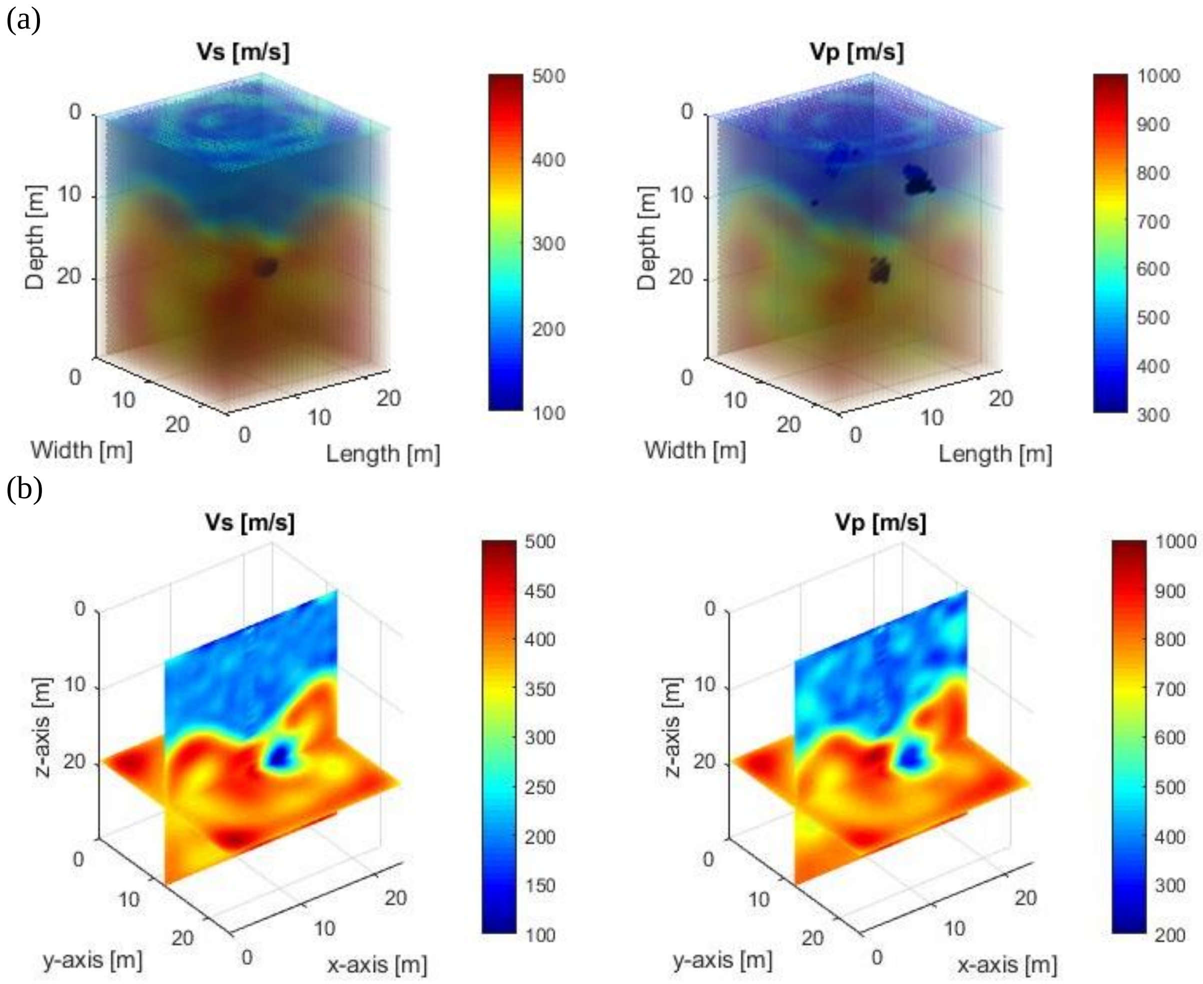

Figure 2.14. Large model: (a) 3D rendering of inverted V_s and V_p; (b) 2D cross-section view of inverted V_s and V_p

2.4 Conclusion

In this task, an advanced 3D SPT-seismic FWI algorithm is developed. Specifically, the forward wave simulation is done in the time-domain, while inversion is conducted in the frequency-domain. There are several advantages of this combined time-frequency approach. First, the wavefields are simulated at multiple frequencies simultaneously without an inverse matrix solver. Second, only a few frequency components are stored for each inversion analysis to significantly reduce the required computer RAM by 90%, allowing the algorithm to run on a standard desktop computer (8 cores, 128 GB RAM). Finally, the frequency-domain data was the sum of time-domain data over time (e.g., stacking to improve signals), allowing analysis of several SPT-blows at a similar depth. This is particularly important for cases of low energy signals in deep rock.

Before being applied to field experimental data, the developed algorithm was tested on two synthetic models (computational data) in this task. Both models represented the typical Florida geology with soils over highly variable limestone, together with embedded voids at 50 ft and 65 ft depths. Waveform data were generated using a 2D grid of sensors at 10-ft spacing on the surface and in-depth sources at 4-ft spacing along a vertical source line (e.g., SPT boring). The waveform data were then analyzed as if they were collected from field experiments. Results were then compared to the true models for assessment of the algorithm's accuracy.

Based on results of two synthetic experiments, the 3D SPT-seismic FWI algorithm showed excellent capabilities for characterizing materials around the SPT boring and offline voids or anomalies. Material properties (V_s, V_p) were well characterized in the 3D domain within 40 ft around the source line (SPT boring) to the depth of 100 ft (or SPT depth). In both experiments, the location and overall shape of deep voids were identified, and the variable layer interfaces were well imaged. The next steps were to optimize the algorithm to minimize field testing and data analyzing efforts (Task 2) and verify it on field experimental data (Task 3).

Chapter 3 – OPTIMIZATION OF FIELD-TESTING CONFIGURATIONS (TASK 2)

3.1 Introduction

The advanced 3D SPT-seismic FWI algorithm has been developed in Task 1. This task is to identify the optimal test configurations (receiver number and spacing, and source interval) for characterizing subsurface profiles in 3D domain with a single SPT. To achieve this, a number of parametric studies were performed with two synthetic (computational) models. For each model, a number of test configurations with different receiver spacings and SPT sampling intervals are used to simulate time-domain wavefields. The wavefields are then converted to frequency domain and used for inversion analyses in order of increasing frequencies. Using low-frequency data requires a less detailed initial model and introducing high-frequency data gradually helps improve resolution of layering, anomalies, properties, etc. By examining the accuracy of inversion results from various test configurations, we can identify the optimal test configurations and SPT sampling intervals to minimize efforts of field testing and data analysis. Test configurations and required SPT sampling intervals identified in this task will be applied in field experiments in Task 3.

For the parametric studies, two synthetic models (hypothetical soil/rock profiles) were designed to represent the typical Florida geological condition with soils underlain by variable bedrock. The two models cover surface areas of 60 × 60 ft and 80 × 80 ft, respectively, and depths up to 100 ft. For each model, a range of test configurations were tested. For the smaller model, four configurations were investigated with receiver grids of 4 × 4, 6 × 6, each with two SPT sampling intervals of 2 and 4 ft. For the larger model of 80 × 80 ft surface area, four configurations were investigated with receiver grids of 4 × 4, 6 × 6, 8 × 8, and 10 ×10, with one SPT sampling interval of 4 ft. The accuracy and resolution of inverted profiles were compared among the simulations to identify the optimal test configurations.

3.2 Model of 60×60-ft surface area

3.2.1 Test configuration and analyses

The developed 3D SPT-Seismic FWI algorithm was first tested on a model of 20.4 × 18 × 18 m (68 × 60 × 60 ft), (depth × length × width). The velocity model representing a variable subsurface profile with V_s of 200 m/s for the top layer and 400 m/s for the lower half space, with twice V_s for V_p profile was used as the true model (Figure 3.1). Furthermore, a buried void of 3 × 3.75 × 3.75 m (depth × length × width) was placed at 15 m depth (50 ft) and 1.0 m away from the source line (or SPT location). It was placed to simulate a deep void that would not be found with an actual SPT. The void was assumed to be filled with air with V_s of 0 m/s and V_p of 300 m/s.

Four test configurations (Figures 3.2 to 3.5) were analyzed to investigate the optimal number and spacing interval of receivers and sampling interval of SPT blows that enabled a successful recovery of the subsurface features including the embedded void. The tests were carried out with an increasing number of receivers and sources. Figures 3.2 and 3.3 show the sparse configuration including 16 receivers of 4 × 4 grid at 4.5 m (15 ft) spacing, and source intervals of 1.2 m (4 ft) and 0.6 m (2 ft), respectively. Figures 3.4 and 3.5 show the dense configuration including 36 receivers of 6 × 6 grid at 4.5 m (10 ft) spacing, and source intervals of 1.2 m (4 ft) and 0.6 m (2 ft).

Analyses were done in the same fashion for all four test configurations. A linearly increasing velocity model of 200 m/s at the ground surface to 400 m/s at the half space for V_s and twice of that for V_p was used as the initial model (Figure 3.6). For each test configuration, two inversion runs were conducted with increasing frequency data. The first run began with the initial model (Figure 3.6), using data at three frequencies of 15, 20 and 25 Hz. The second run continued with data at three frequencies of 30, 35 and 40 Hz, using the result of the first run as the input velocity model. Both runs stopped after 100 iterations. It is noted that the 6 frequencies selected for analyses are based on the typical frequency range (10 to 40 Hz) of seismic data induced by SPT hammers.

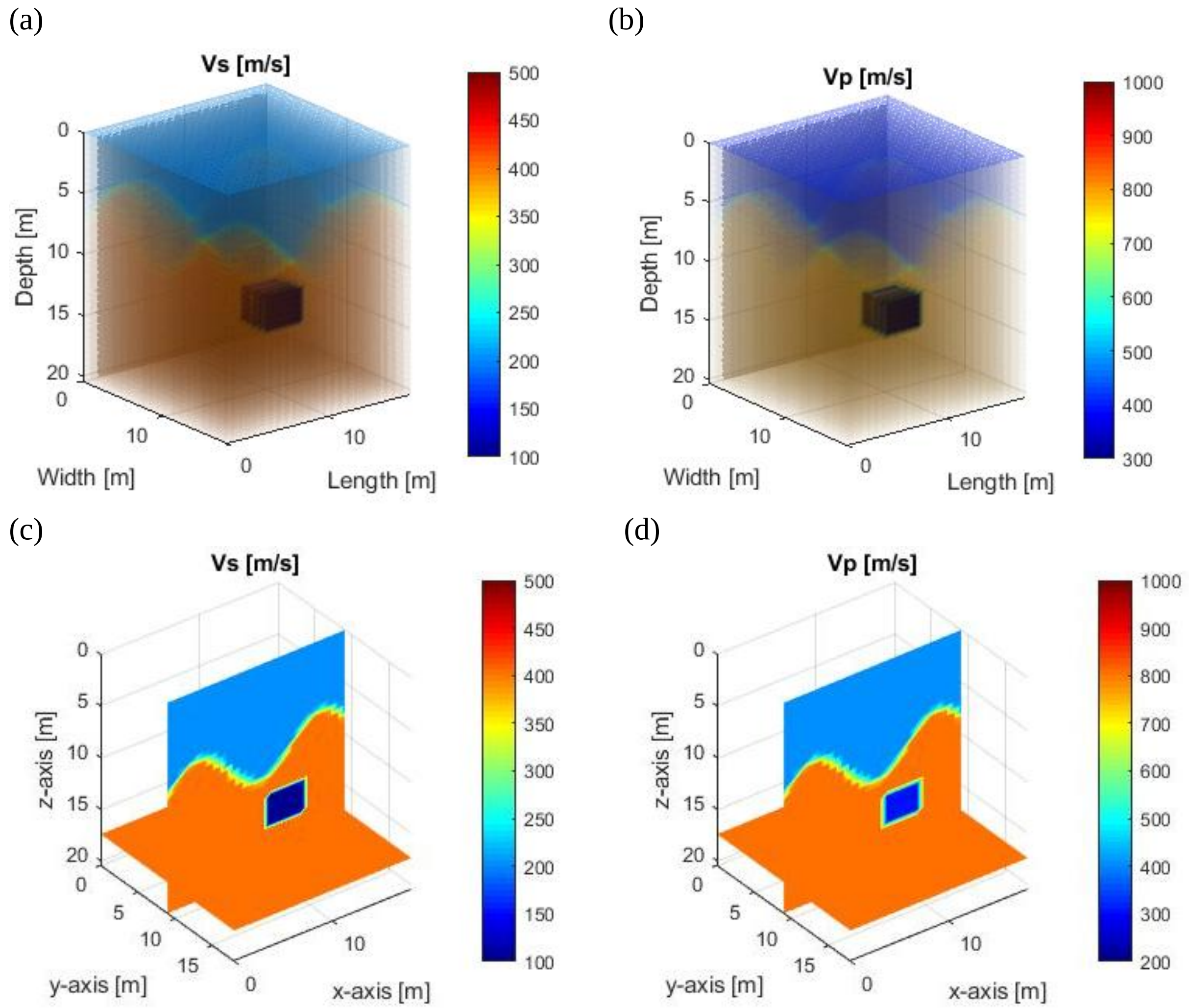

Figure 3.1. Smaller synthetic model with a deep void: (a) 3D rendering of V_s; (b) 3D rendering of V_p model; (c) 2D cross-section view of V_s; (d) 2D cross-section view of V_p

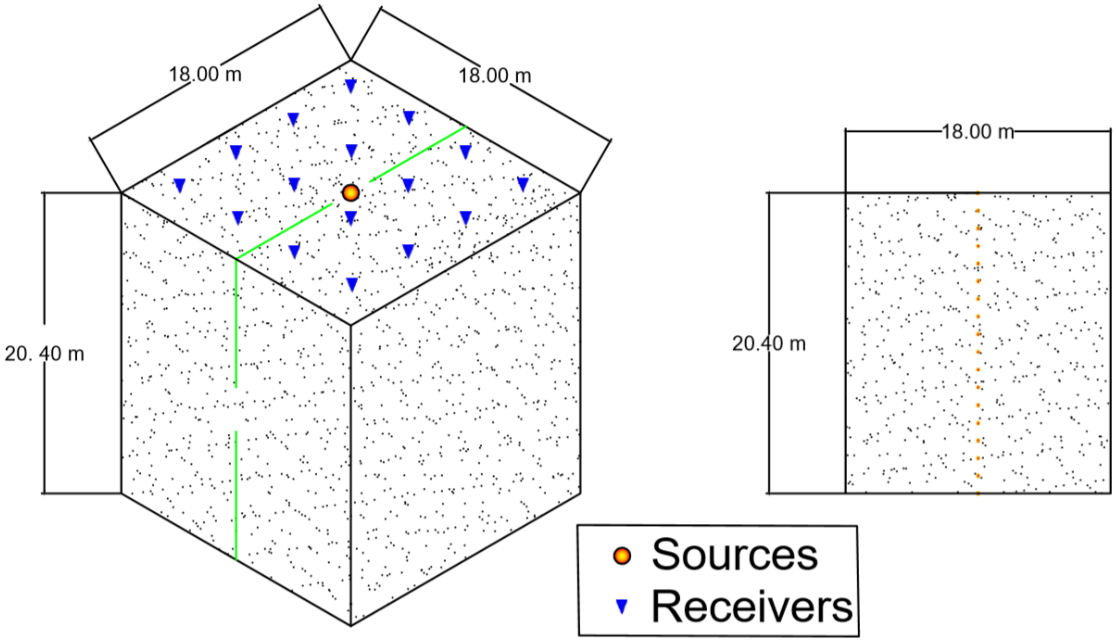

Figure 3.2. Test configuration 1: 16 receivers of 4.5-m spacing and 18 sources of 1.2-m interval

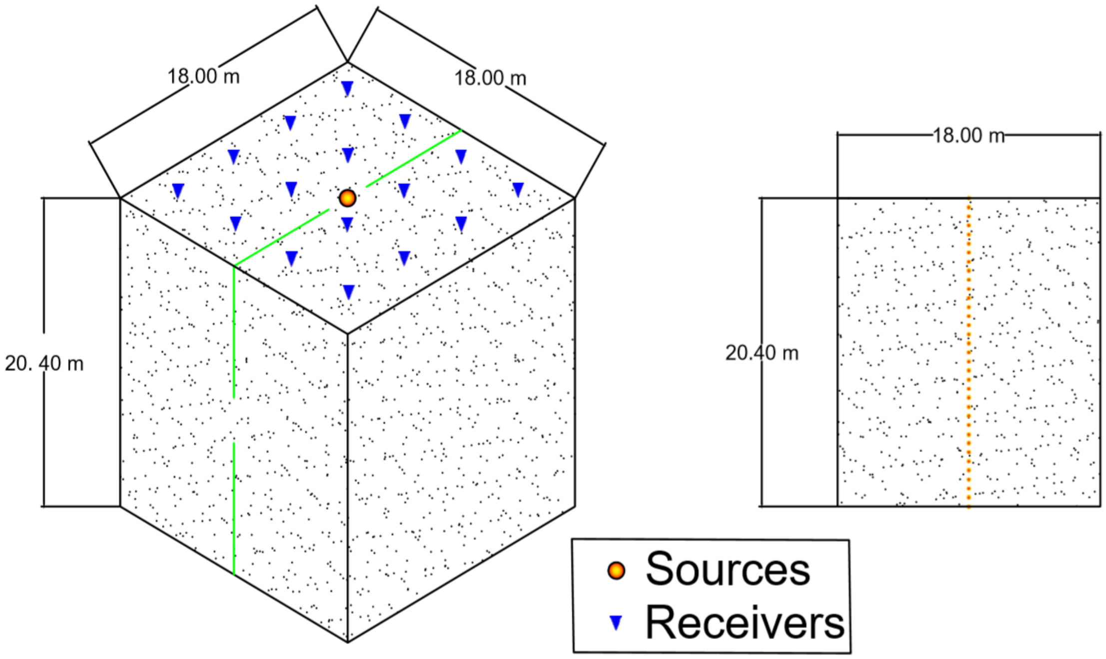

Figure 3.3. Test configuration 2: 16 receivers of 4.5-m spacing and 35 sources of 0.6-m interval

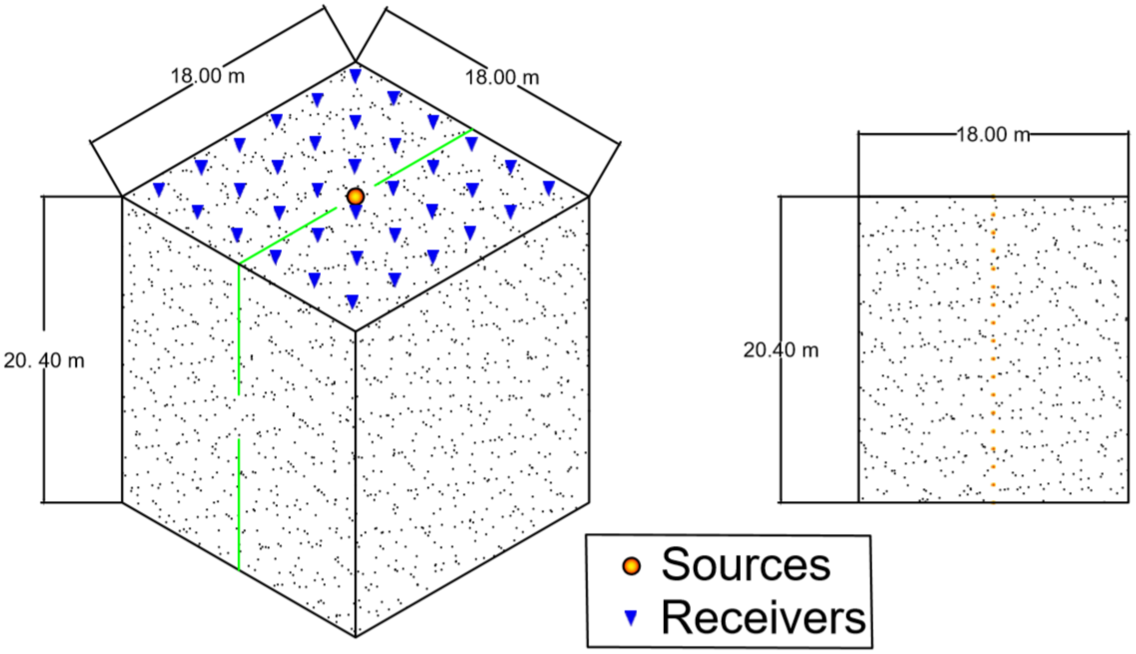

Figure 3.4. Test configuration 3: 36 receivers of 3.0-m spacing and 18 sources of 1.2-m interval

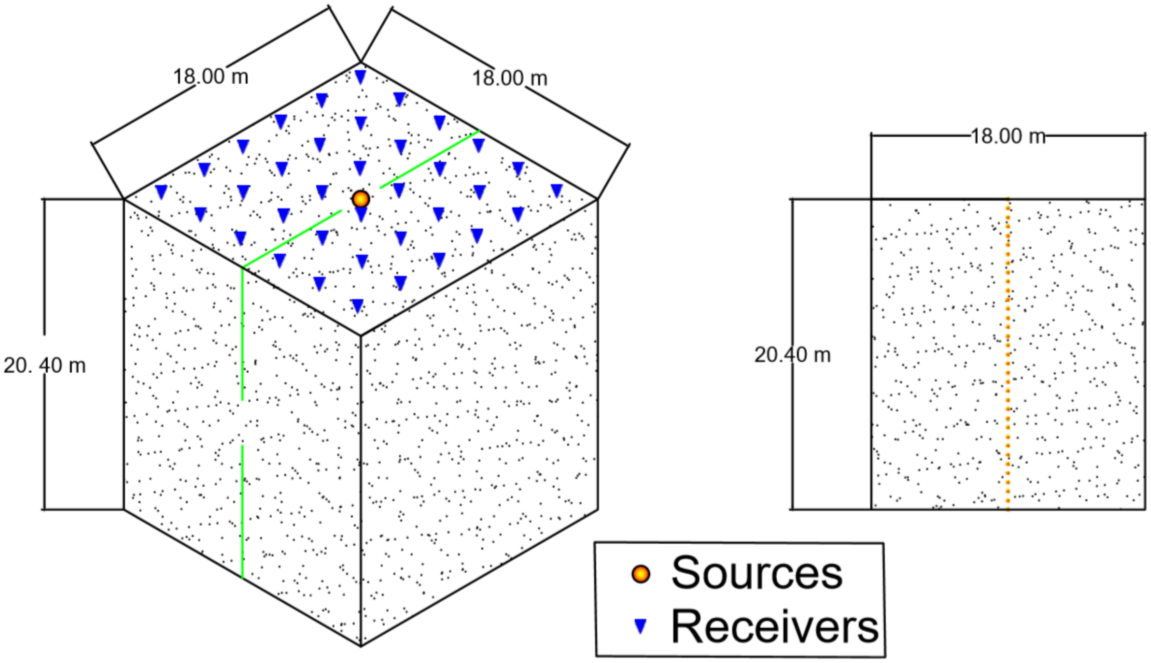

Figure 3.5. Test configuration 4: 36 receivers of 3.0-m spacing and 35 sources of 0.6-m interval

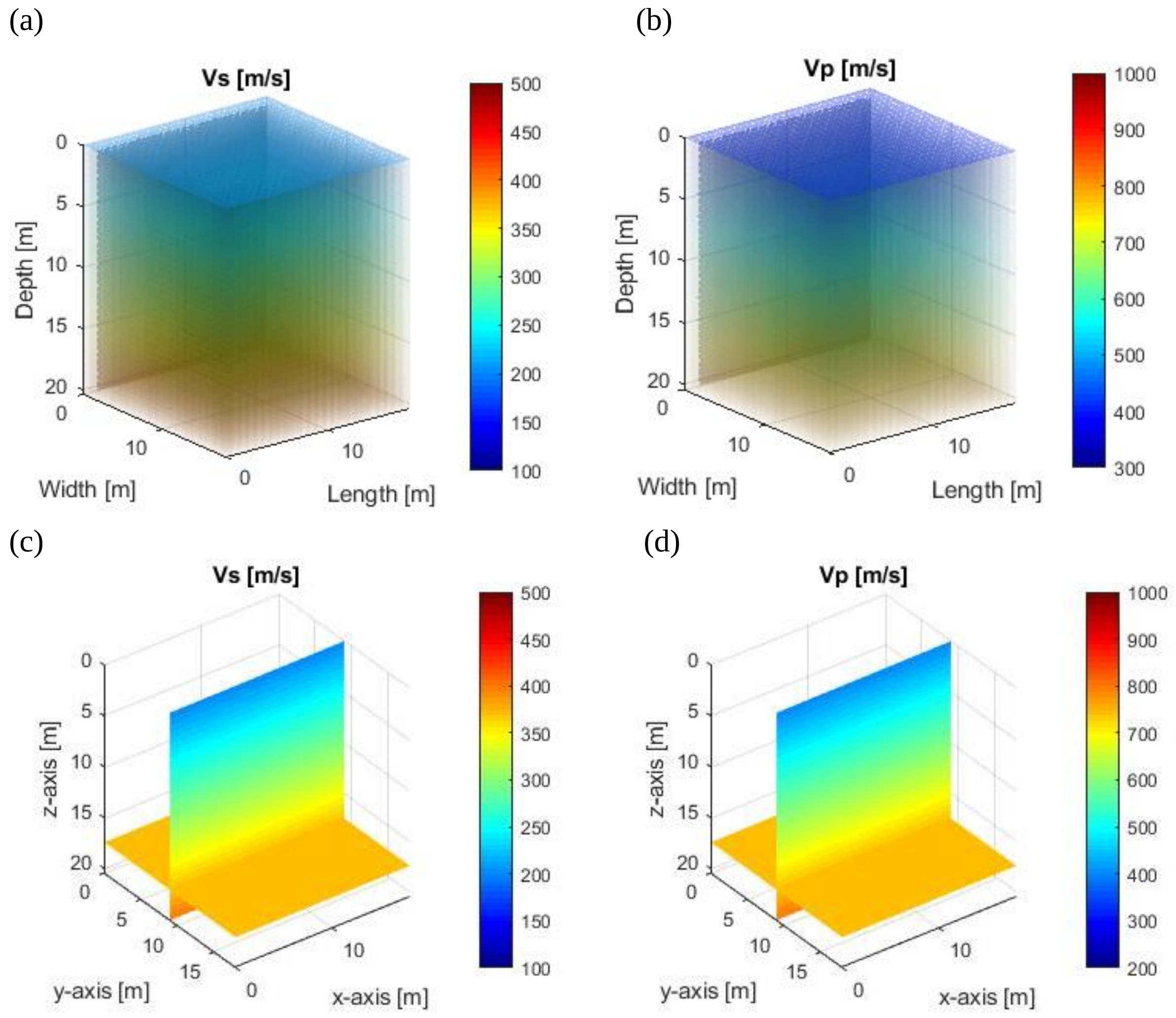

Figure 3.6. Initial model used for all four test configurations: (a) 3D rendering of V_s; (b) 3D rendering of V_p; (c) 2D cross-section view of V_s; (d) 2D cross-section view of V_p

3.2.2 Results for test configuration 1 (16 receivers at 15-ft spacing, 18 sources at 4-ft interval)

To evaluate the algorithm's performance, the misfit error and waveform comparisons are examined. The normalized least-squares error for all iterations of the two inversion runs are shown in Figure 3.7. The error decreased from 1.0 at the first iteration to about 0.01 at the final iteration of the first run, and to 0.06 in the second run. The large reduction of error (99% for the first run, and 94 % for the second run) is a good measurement for the improvement of waveform fitting. It is noted that the error jumped at the beginning of the second run at higher frequencies because the model is not yet appropriate to produce the recorded wave propagation of shorter wavelengths.

Shown in Figure 3.8 is a sample waveform comparison between the observed data from the true model and estimated data associated with the initial model and the final inverted model at iteration 200. At the beginning of analysis, the clear discrepancy between observed and estimated waveform data was observed (Figure 3.8a). This was due to the fact that estimated data are computed from the initial model (Figure 3.6) with no void, no layer interface, and different V_s and V_p values from the true model. No reflected signals from the void and the layer interface existed in the estimated data, while the observed data contained such reflected signals.

At the end of analysis, an excellent match between observed and estimated data was obtained (Figure 3.8b) because the model was updated toward the true model during inversion. The waveform match improved substantially during inversion. Phase and amplitudes were matched perfectly at the end. No cycle skipping or matching of wrong peaks was observed, indicating the success of the inversion algorithm that vectored toward the global minimum.

The excellent match of observed and estimated data shows that a few dominant frequency components could well represent waveforms for the entire filtered frequency bandwidth. Matching data at 6 frequencies (15, 20, 25, 30, 35, and 40 Hz) allows matching the waveforms in the time-domain for the entire filtered bandwidth from 10 to 50 Hz. In other words, there is a lot of redundant information in the time-domain waveforms, and only a few frequencies are needed for analysis.

The final inverted V_s and V_p profiles are displayed in Figure 3.9. Even with the sparse test configuration of only 16 receivers, V_s profile (Figure 3.9 a) was well characterized. The existence of two separate layers is clearly observed, and the variable layer interface is well imaged. More importantly, the location and overall shape of the deep void is successfully identified. However, the characterized V_p profile (Figure 3.9 b) is less accurate. While the void is imaged, several artifacts exist at shallow depths. This is due to the fact that there are not enough receivers to capture P-waves with longer wavelengths (twice S-wave wavelengths). The 2D cross-section views of results (Figure 3.9 c and d) confirm that the variable layers and void are characterized by the algorithm.

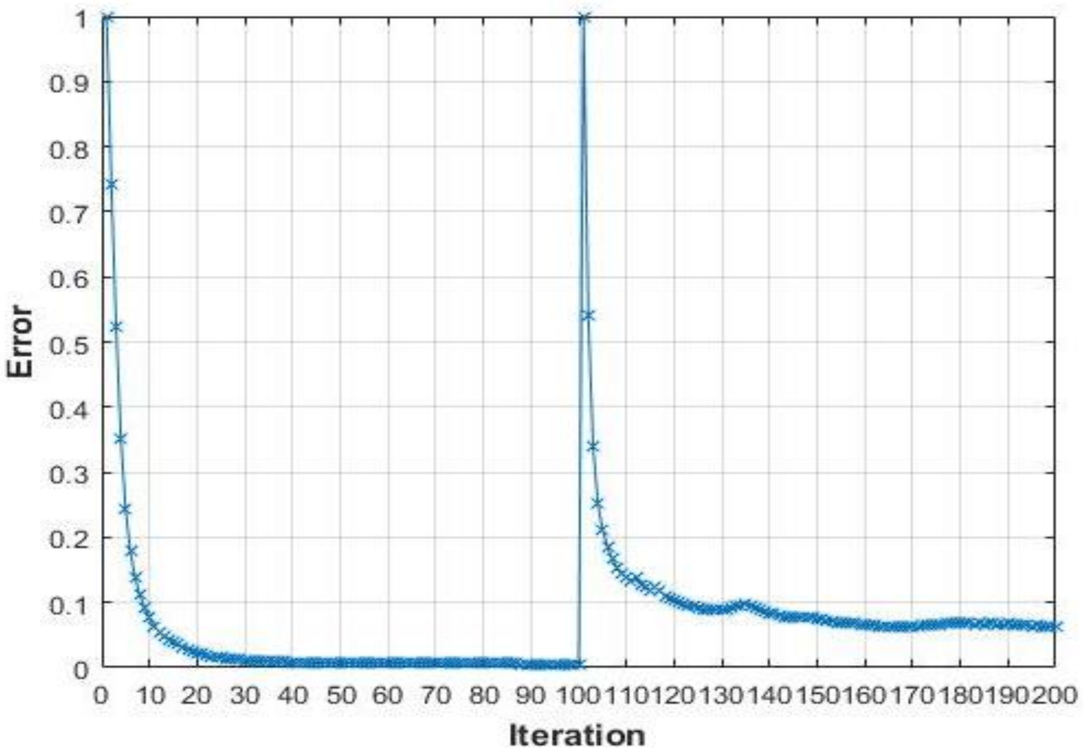

Figure 3.7. Test configuration 1: normalized least-squares error for both runs

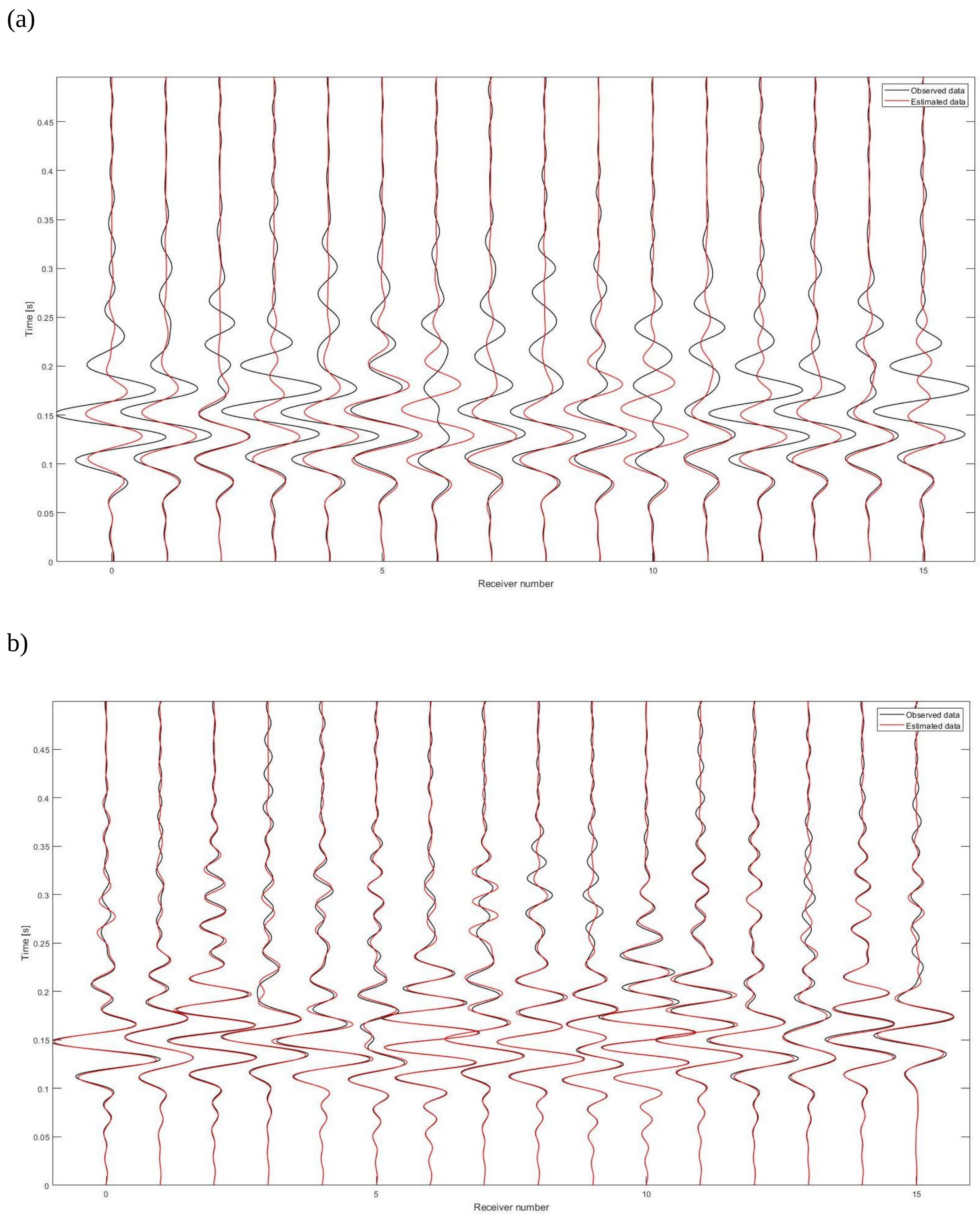

Figure 3.8. Test configuration 1: waveform comparison for a sample shot: (a) observed waveform and estimated waveform associated with the initial model; (b) observed waveform and estimated waveform associated with the final inverted model

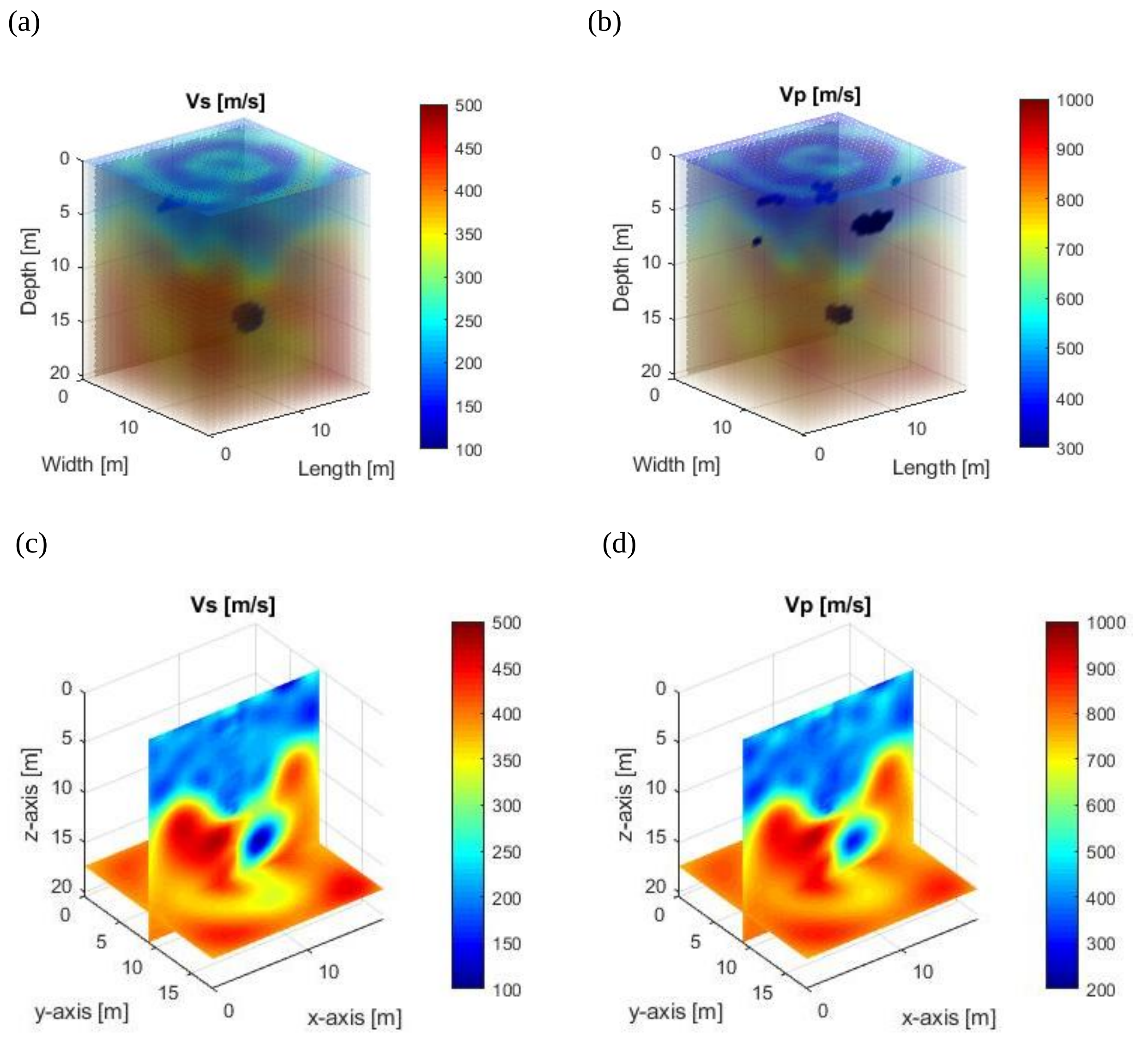

Figure 3.9. Results of test configurations 1 (16 receivers, 18 sources): (a) 3D inverted V_s; (b) 3D inverted V_p; (c) 2D cross-section view of inverted V_s; (d) 2D cross-section view of inverted V_p

3.2.3 Results for test configuration 2 (16 receivers at 15-ft spacing, 35 sources at 2-ft interval)

The inverted V_s and V_p profiles for test configuration 2 (16 receivers, 35 sources) are displayed in Figure 3.10. These results are very similar to those of test configuration 1 (Figure 3.9), including the void and layer interface. The artifacts still exist in the V_p image (Figure 3.10b), suggesting that increasing the number of sources does not improve the accuracy of inverted V_p. More receivers are needed to accurately capture P-wave propagation and inversion.

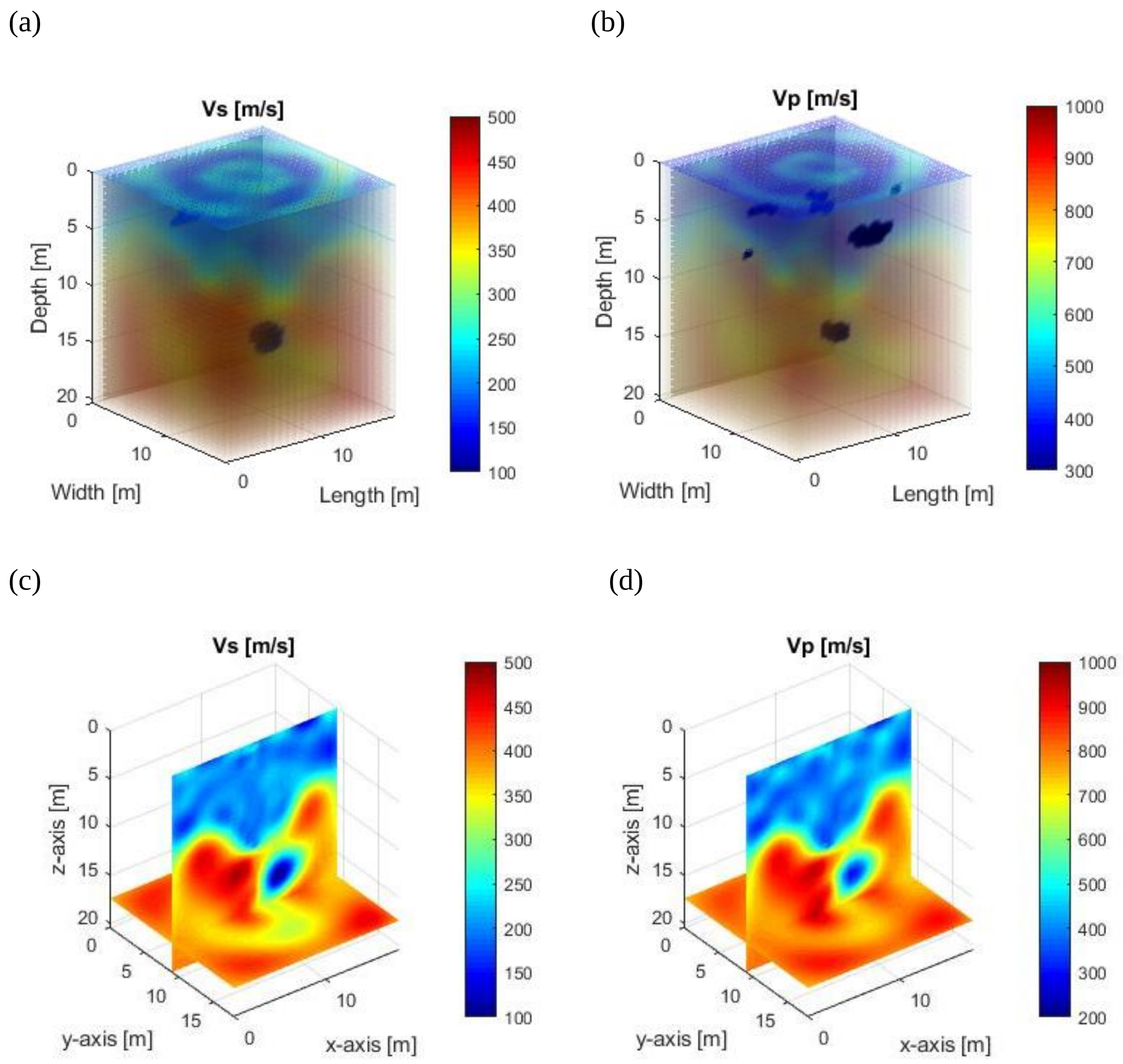

Figure 3.10. Results of test configurations 2 (16 receivers, 35 sources): (a) 3D inverted V_s; (b) 3D inverted V_p; (c) 2D cross-section view of inverted V_s; (d) 2D cross-section view of inverted V_p

3.2.4 Results for test configuration 3 (36 receivers at 10-ft spacing, 18 sources at 4-ft interval)

Next, the inversion analysis was performed for the dense test configuration of 36 receivers at 10 ft spacing, and 18 sources at 4 ft interval, as shown in Figure 3.4. Normalized least-squares error of the two inversion runs is shown in Figure 3.11, where the error reduced from 1.0 at the first iteration to about 0.02 at the end of the first run (iteration #100), and to 0.2 at the end of the second run (iteration #200). Waveform and residual comparisons are displayed in Figure 3.12. The inversion has drastically improved the waveform fitting from the initial stage (Figure 3.12a) to the final stage (Figure 3.12b).

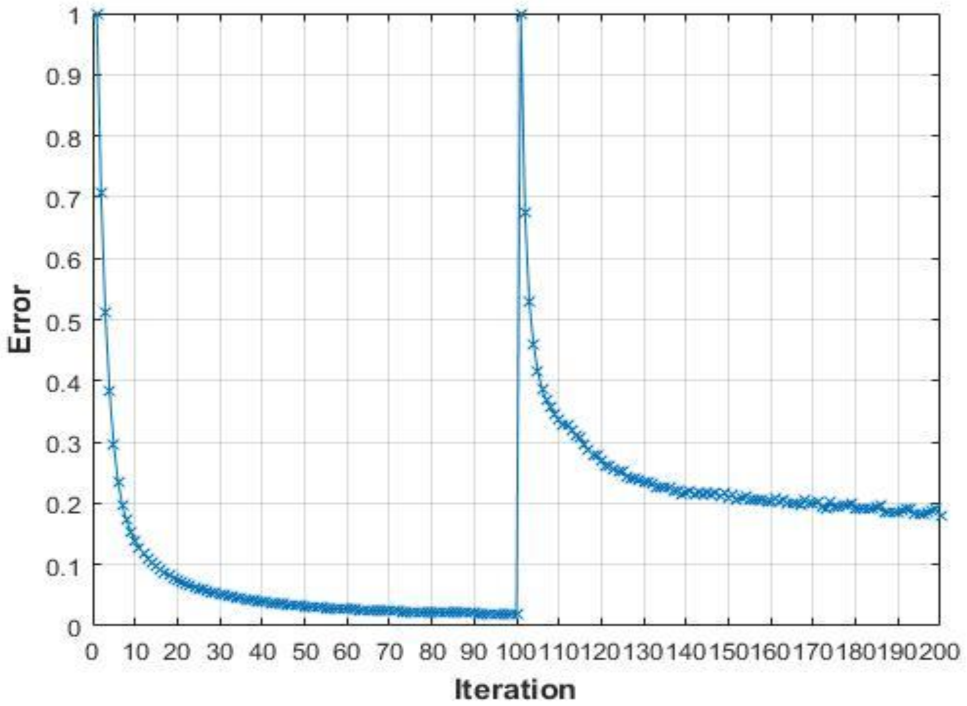

Figure 3.11. Test configuration 3: normalized least-squares error for two runs

The inverted V_s and V_p profiles are displayed in Figure 3.13. As expected, for inverted V_s (Figure 3.13a), the layers are characterized, and the location and size of the void are recovered. For inverted V_p (Figure 3.13b), the layers and void are also characterized. There are still two small artifacts at shallow depths, but they are negligible. The result has been improved considerably compared to those in Figure 3.12b. The 2D cross-section views of results (Figure 3.13 c and d) confirm the variable layers and void are well characterized. This test configuration produces satisfying results for both V_s and V_p.

(a)

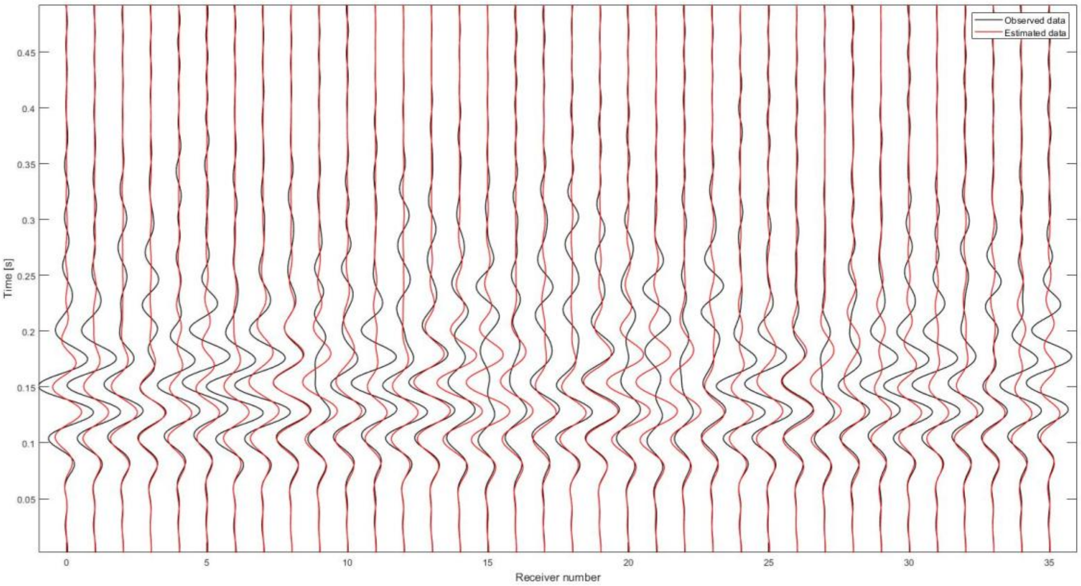

(b)

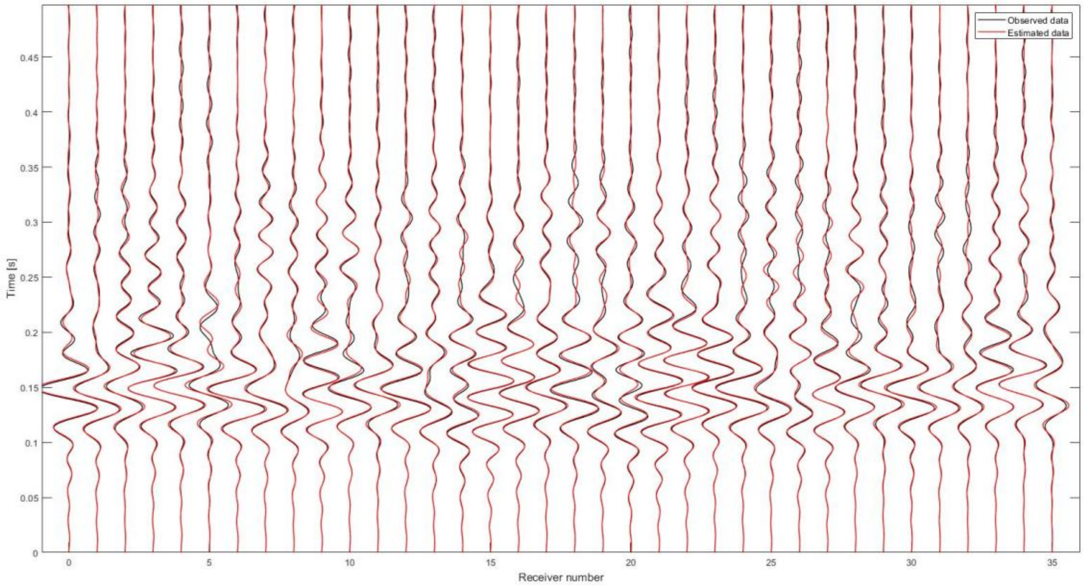

Figure 3.12. Test configuration 3: waveform comparison for the deepest source: (a) observed waveform and estimated waveform associated with the initial model; (b) observed waveform and estimated waveform associated with the final inverted model

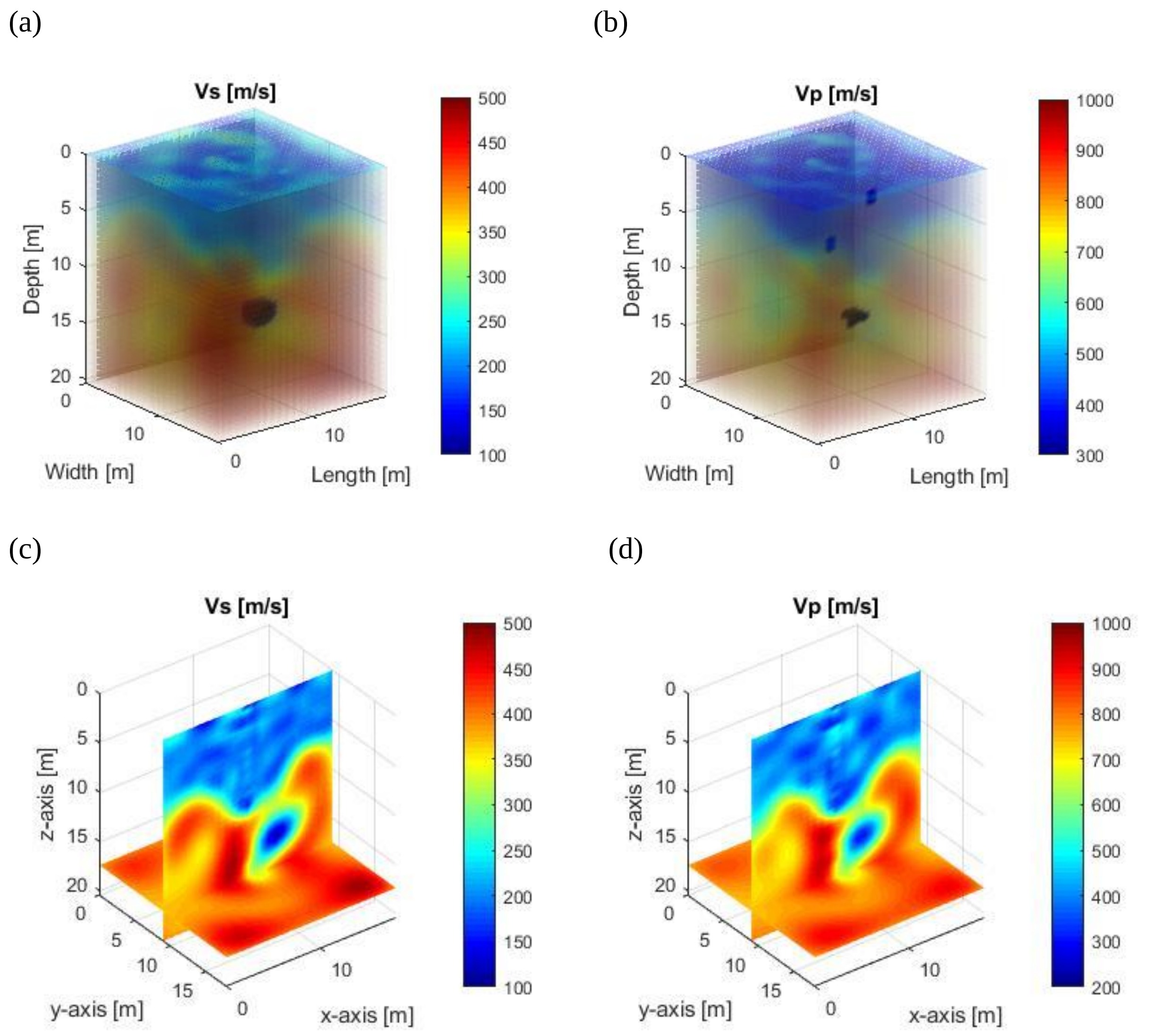

Figure 3.13. Results of test configurations 3 (36 receivers, 18 sources): (a) 3D inverted V_s; (b) 3D inverted V_p; (c) 2D cross-section view of inverted V_s; (d) 2D cross-section view of inverted V_p

3.2.5 Results for test configuration 4 (36 receivers at 10-ft spacing, 35 sources at 2-ft interval)

The inverted V_s and V_p profiles for test configuration 4 (36 receivers, 35 sources) are displayed in Figure 3.14. These results are similar to those of test configuration 3 (Figure 3.13), including the void, layer interface, and true velocity values. Again, increasing the number of sources does not improve inverted results due to data redundancy.

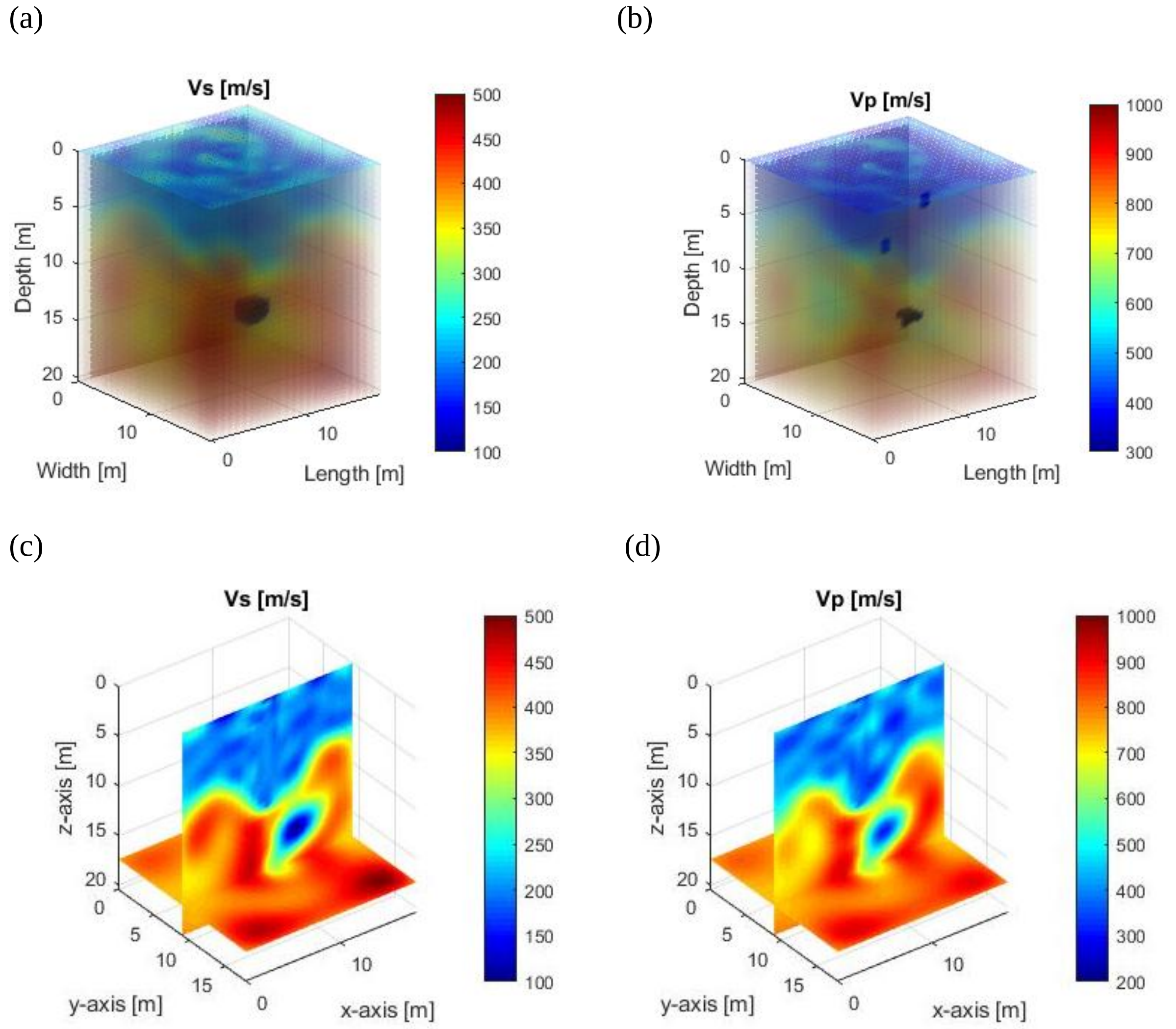

Figure 3.14. Results of test configurations 4 (36 receivers, 35 sources): (a) 3D inverted V_s; (b) 3D inverted V_p; (c) 2D cross-section view of inverted V_s; (d) 2D cross-section view of inverted V_p

3.3 Model of 80×80-ft surface area

3.3.1 Test configuration and analyses

The developed 3D SPT-Seismic FWI algorithm was then tested on a larger model of 30 × 24× 24 m (100 × 80 × 80 ft). The velocity model (Figure 3.15) represents a variable subsurface profile with V_s of 200 m/s for the top layer and 400 m/s for the lower half space, with V_p twice of V_s. An offline void of 3 m × 3.75 m × 3.75 m (depth × length × width) was placed at 19 m depth and 2 m away from the source line, thus it would not be found with an actual SPT. The void was assumed to be filled with air with V_s of 0 m/s and V_p of 300 m/s. A mass density of 1,800 kg/m3 is assumed to be for the whole medium, as a typical value for general soils.

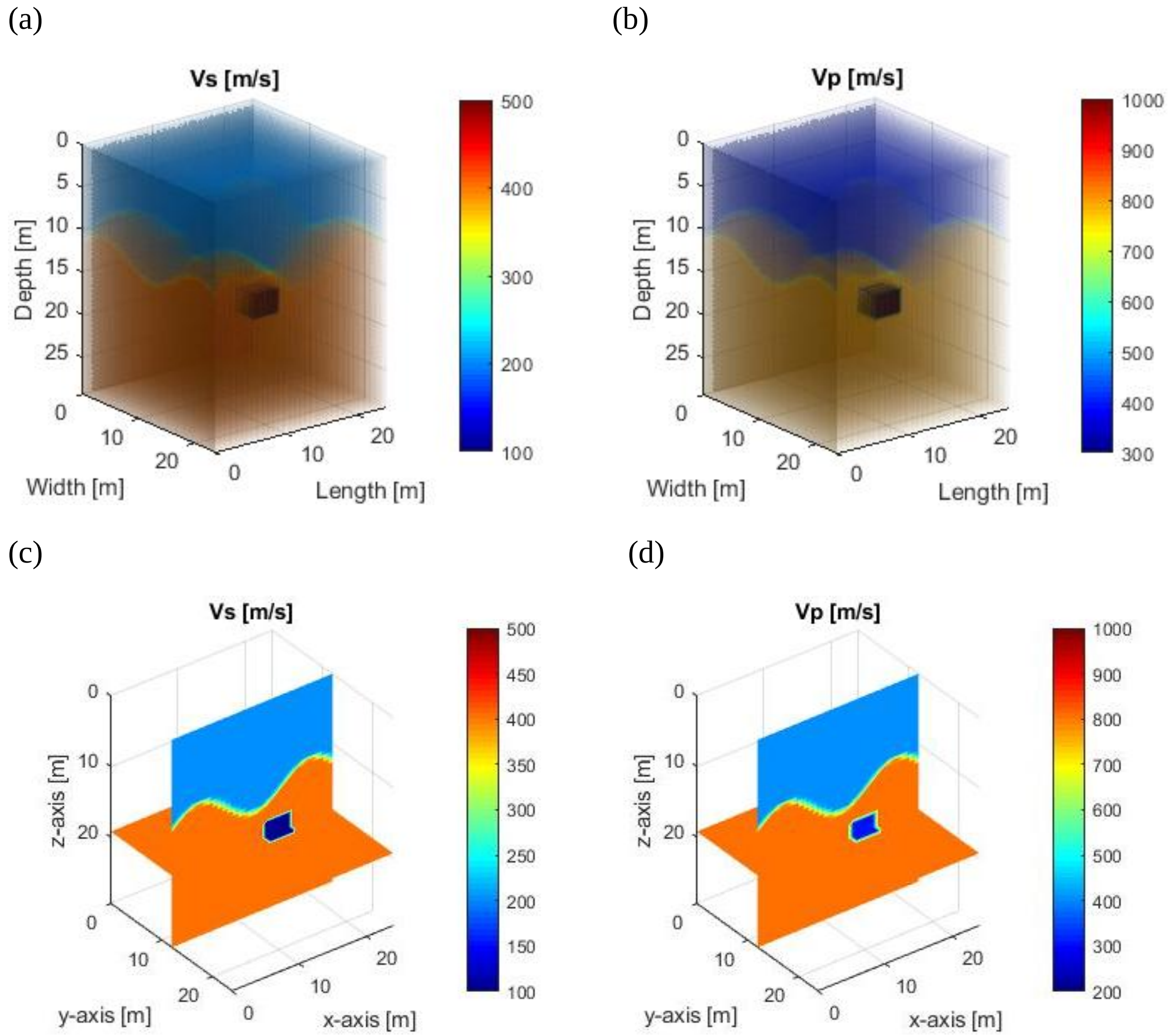

Figure 3.15. Larger synthetic model with a deep void: (a) 3D rendering of V_s; (b) 3D rendering of V_p model; (c) 2D cross-section view of V_s; (d) 2D cross-section view of V_p

Four test configurations were analyzed to investigate the optimal number and spacing interval of receivers for successful recovery of the subsurface features. The analyses were carried out with an increasing number of receivers. The four configurations are shown in Figures 3.16 to 3.19, with receiver grids of 4 × 4, 6 × 6, 8 × 8, and 10 ×10 and one SPT sampling interval of 4 ft.

As shown in the previous model, a smaller SPT sampling interval (2 ft) does not improve inversion results, thus only one SPT sampling interval of 4 ft was investigated for this larger model.

Like the previous model, analyses for all four test configurations were conducted in the same fashion. A velocity model with V_s increasing from 200 m/s at the free surface (0-m depth) to 400 m/s at the model bottom (30 m depth) was used as the initial model (Figure 3.20). For each test configuration, two inversions were conducted with increasing frequency data. The first run began with the initial model (Figure 3.20), using data at three frequencies of 15, 20 and 25 Hz. The second run continued on data at three frequencies of 30, 35 and 40 Hz, using the result of the first run as the input velocity model. Both runs stopped after 100 iterations.

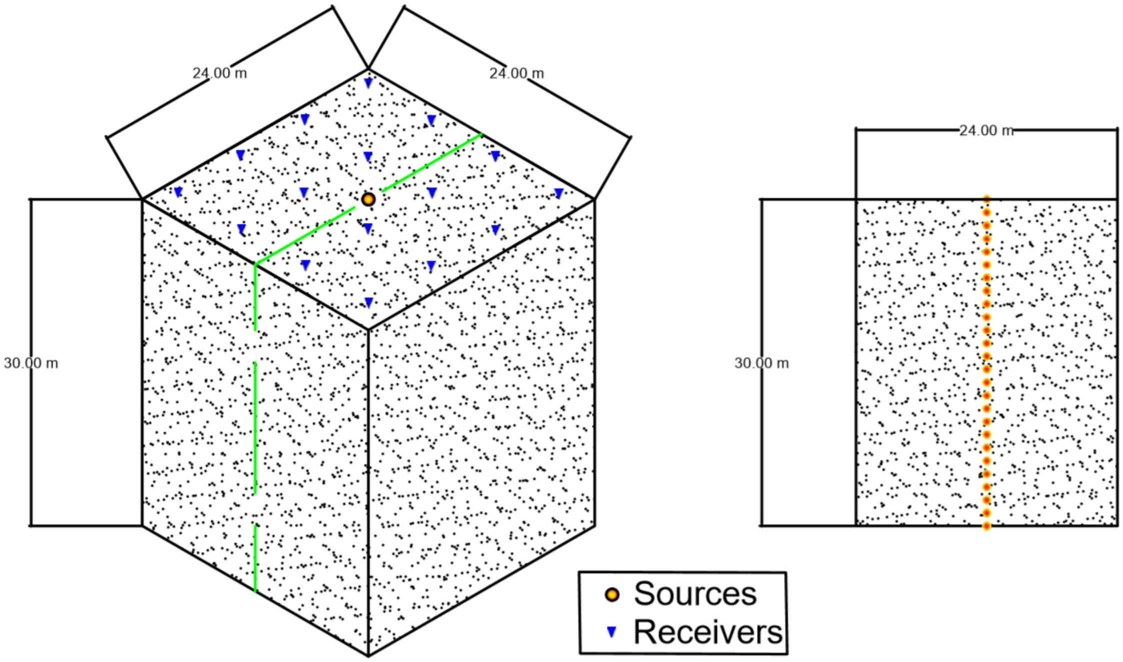

Figure 3.16. Test configuration 5: 16 receivers at 6.75-m spacing and 25 sources at 1.2-m interval

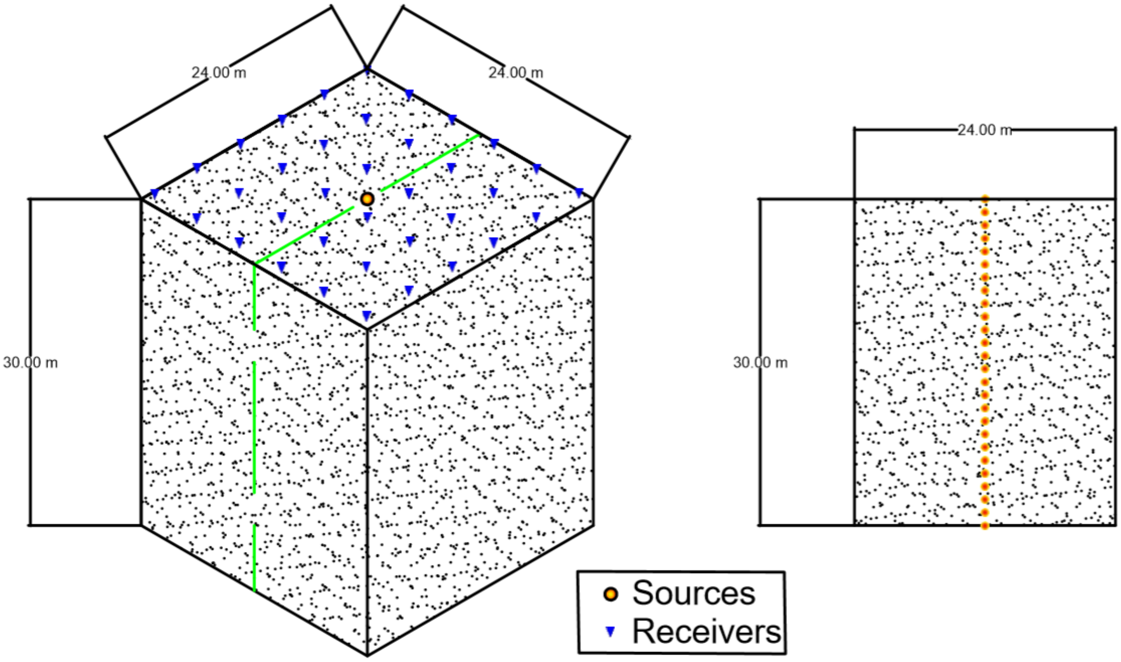

Figure 3.17. Test configuration 6: 36 receivers at 4.5-m spacing and 25 sources at 1.2-m interval

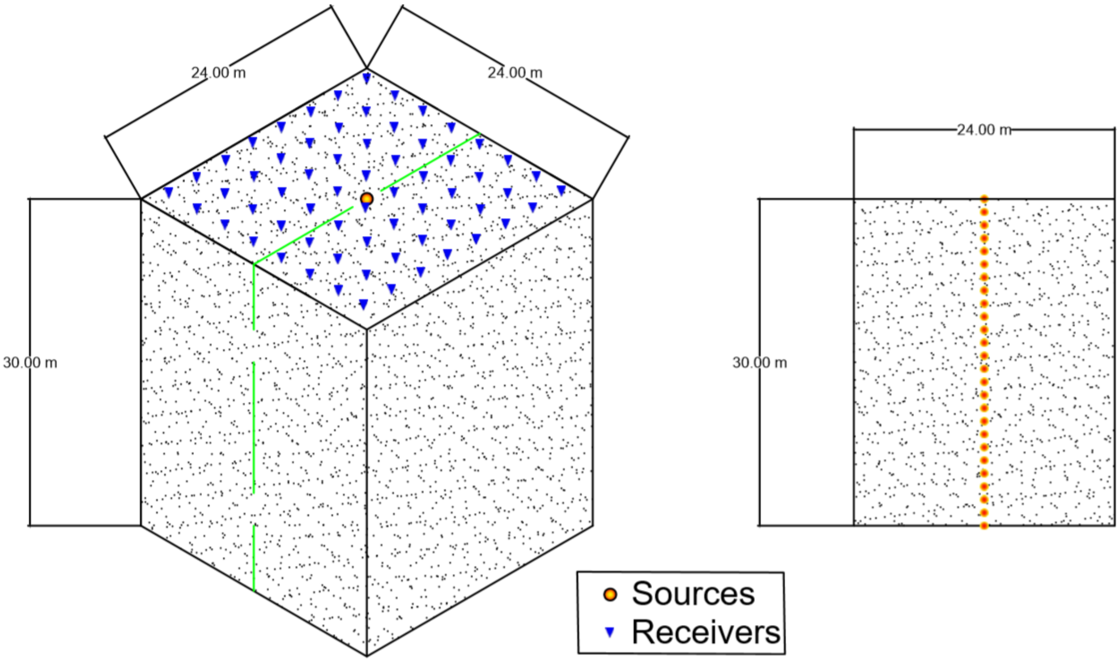

Figure 3.18. Test configuration 7: 64 receivers at 3.0-m spacing and 25 sources at 1.2-m interval

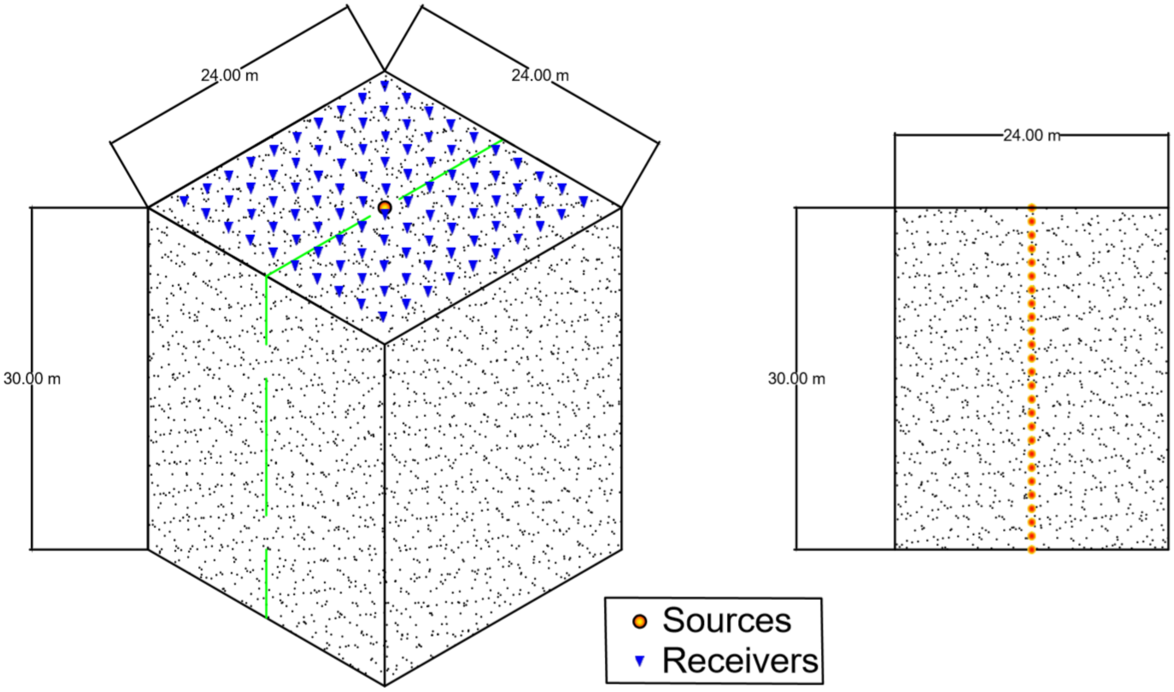

Figure 3.19. Test configuration 8: 100 receivers at 2.25-m spacing and 25 sources at 1.2-m interval

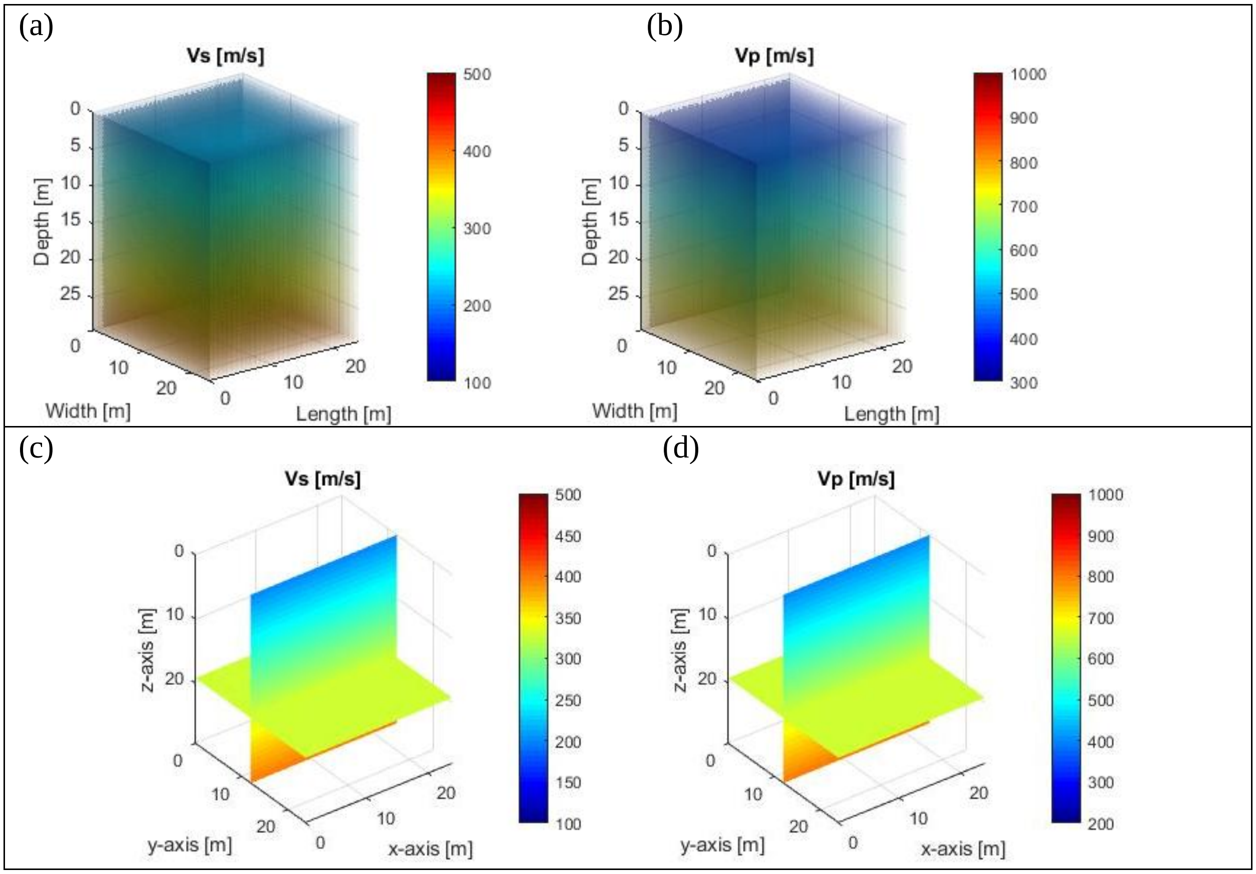

Figure 3.20. Initial model used for all test configurations: (a) 3D rendering of V_s; (b) 3D rendering of V_p; (c) 2D cross-section view of V_s; d) 3D cross-section view of V_p

3.3.2 Results for test configuration 5 (16 receivers at 22.5-ft spacing, 25 sources at 4-ft interval)

To assess the algorithm's performance on this larger model, the misfit error and waveform comparison are examined. The normalized least-squares error of all iterations for test configuration 5 are shown in Figure 3.21. The error reduced from 1.0 at the beginning to about 0.01 at the end of the first run, and to 0.07 in the second run. Shown in Figure 3.22 is the waveform comparison between the observed data from the true model and estimated data associated with the initial model and the final inverted model at iteration 200. The waveform match improved significantly during inversion from Figure 3.22a at the beginning to Figure 3.22b at the end of analyses. Both phase and amplitude match well at the end, indicating the inversion converges towards the global minimum.

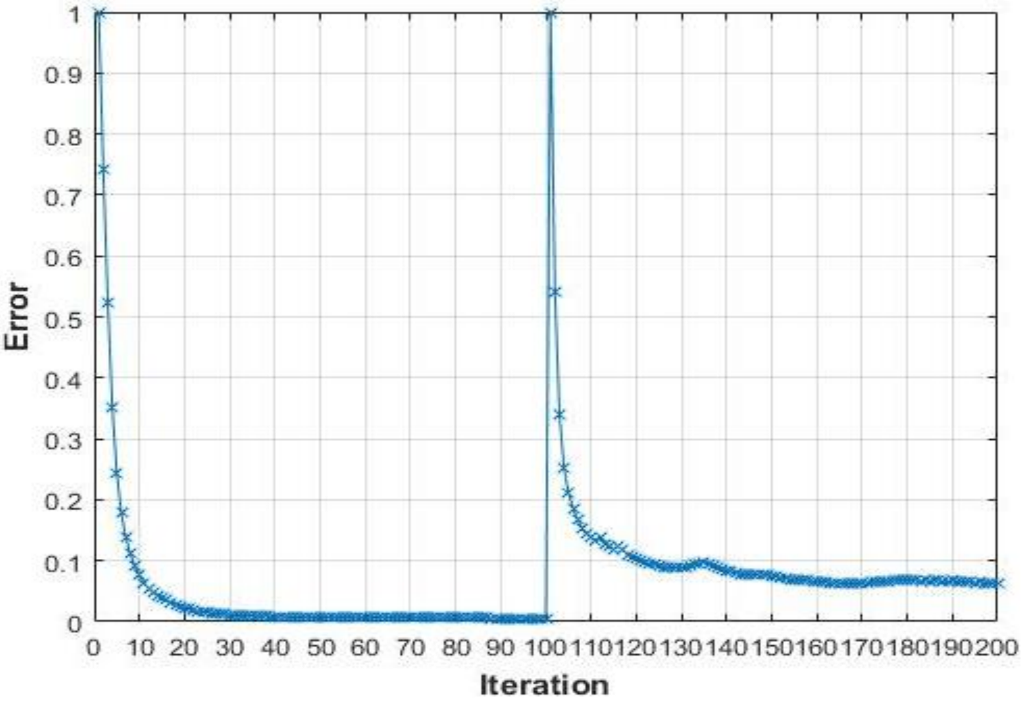

Figure 3.21. Test configuration 5: normalized least-squares error for both inversion runs

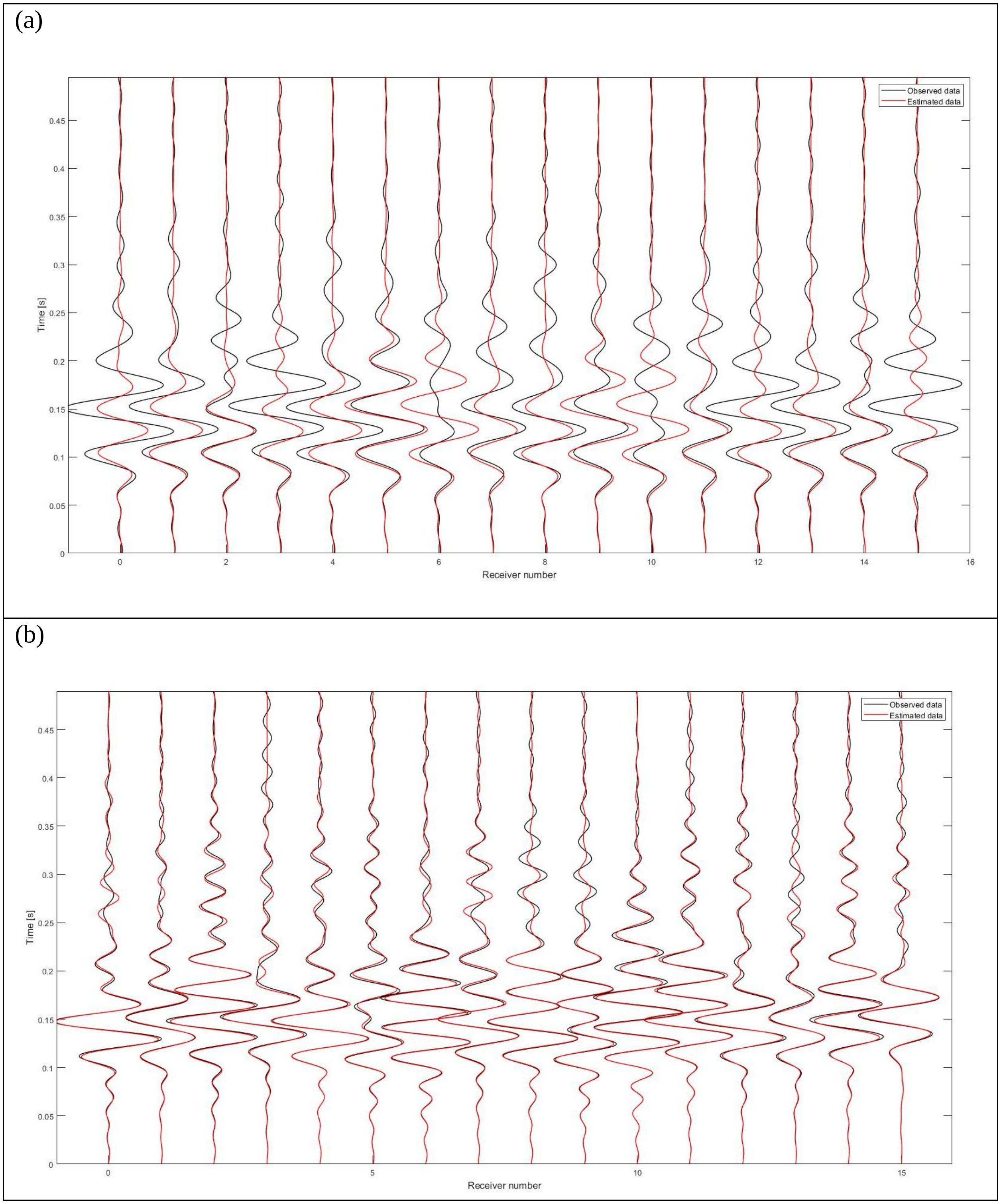

Figure 3.22. Test configuration 5: waveform comparison for the deepest source: (a) observed waveform and estimated waveform associated with the initial model; (b) observed waveform and estimated waveform associated with the final inverted model

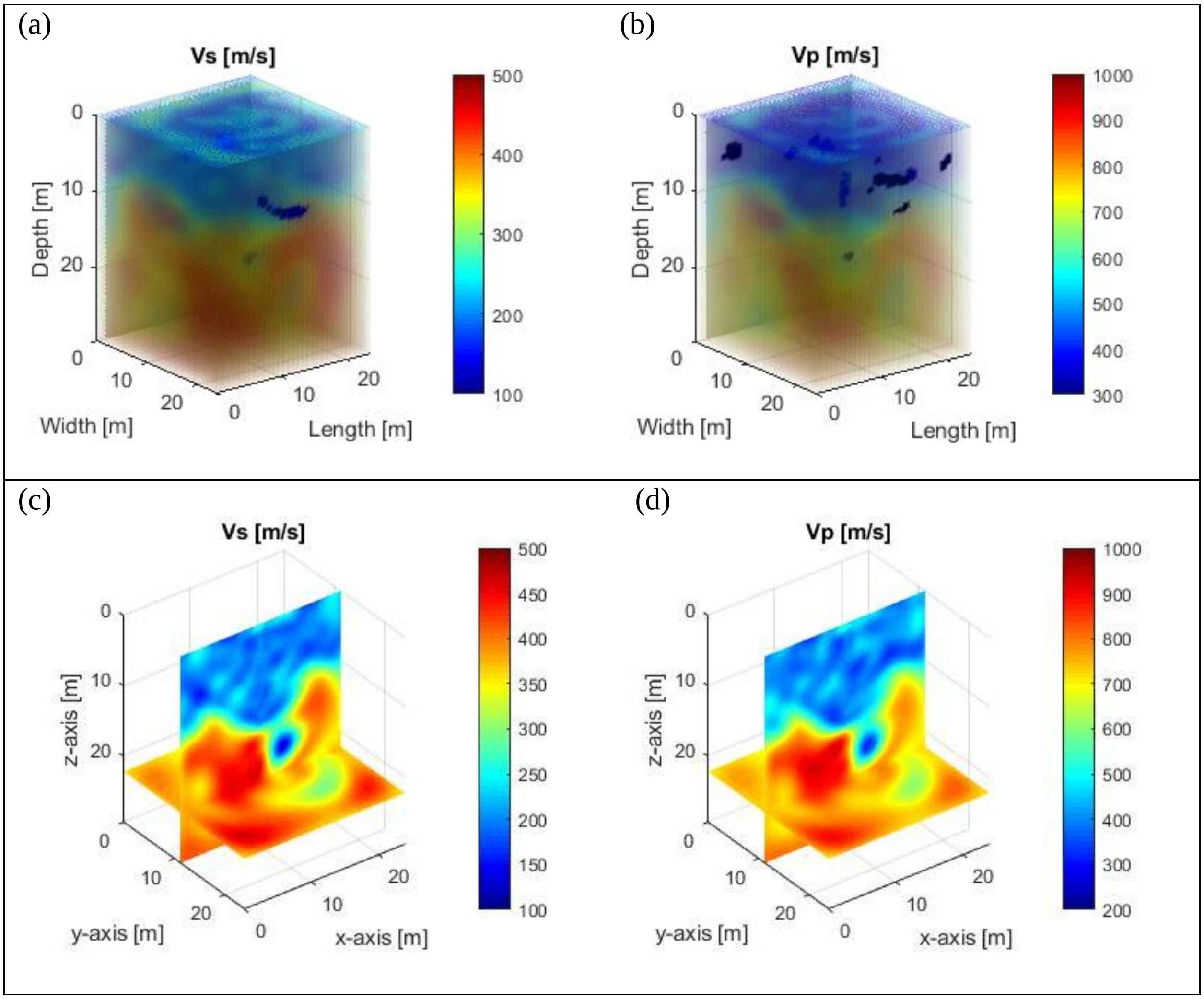

Figure 3.23. Results of test configurations 5 (16 receivers, 25 sources): (a) 3D inverted V_s; (b) 3D inverted V_p; (c) 2D cross-section view of inverted V_s; (d) 2D cross-section view of inverted V_p

The final inverted V_s and V_p profiles are shown in Figure 3.23. Even with the sparse test configuration of 16 receivers at a large spacing (22.5 ft), the algorithm can still characterize the two layers; the variable layer interface is imaged. However, the void is not characterized with the correct size. Inversion artifacts are shown at shallow depths in both V_s and V_p images (Figure 3.23 a and b). The 2D cross-section views of results (Figure 3.23 c and d) show the variable layer interface and an anomaly at the void location. However, the inverted V_s of the void is only about 200 m/s, which is much higher than its true velocity of zero. More receivers are needed to capture both S-wave and P-wave components for accurate inversion results.

3.3.3 Results for test configuration 6 (36 receivers at 15-ft spacing, 25 sources at 4-ft interval)

The inverted V_s and V_p profiles for test configuration 6 are shown in Figure 3.24. Compared to the results (Figure 3.23a) of test configuration 5, V_s profile (Figure 3.24a) is characterized much better without inversion artifacts. The void is characterized with good accuracy of its location and size. However, significant artifacts still exist in the V_p image, because the receiver grid is too sparse to capture P-waves with longer wavelengths. The 2D cross-section views of results (Figure 3.24 c and d) confirm that the variable layers and void are characterized. This test configuration only produces good results for V_s profile, but not V_p profile.

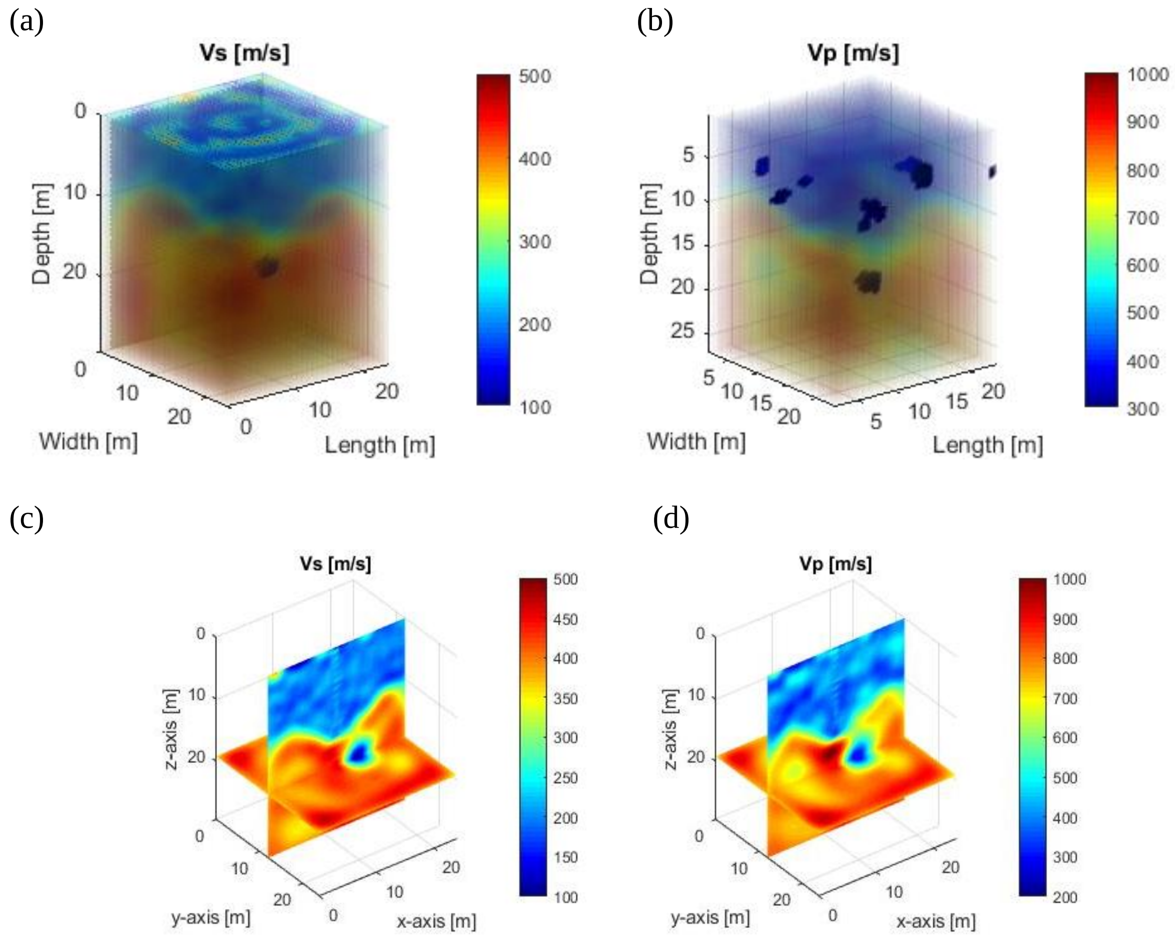

Figure 3.24. Results of test configurations 6 (36 receivers, 25 sources): (a) Inverted 3D V_s model; (b) Inverted 3D V_p model; (c) 2D cross-section view of inverted V_s model; (d) inverted 2D cross-section view of inverted V_p model

3.3.4 Results for test configuration 7 (64 receivers at 10-ft spacing, 25 sources at 4-ft interval)

The inverted V_s and V_p profiles for test configuration 7 are shown in Figure 3.25. As expected, V_s profile (Figure 3.25a) is well characterized. The layer interface and the void are characterized with good accuracy. Regarding V_p file (Figure 3.25b), there is a considerable improvement compared to the V_p result (Figure 3.24b) of test configuration 6. Most of artifacts were eliminated with this denser test configuration. The 2D cross-section views of results (Figure 3.24 c and d) confirm the variable layers and void are characterized. Test configuration 7 produces satisfying results for both V_s and V_p profiles.

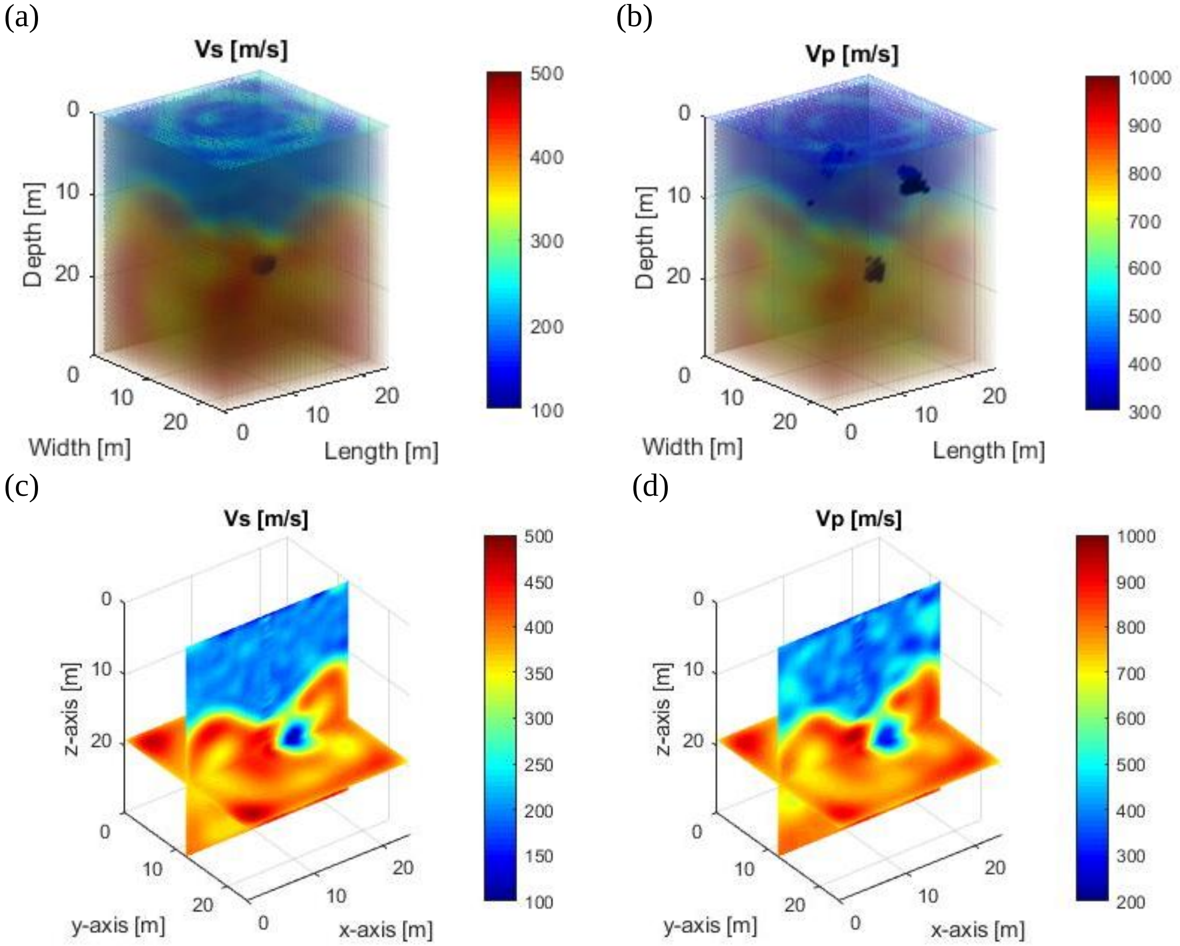

Figure 3.25. Results of test configurations 7 (64 receivers, 25 sources): (a) Inverted 3D V_s model; (b) Inverted 3D V_p model; (c) 2D cross-section view of inverted V_s model; (d) inverted 2D cross-section view of inverted V_p model

3.3.5 Results for test configuration 8 (100 receivers at 7.5-ft spacing, 25 sources at 4-ft interval)

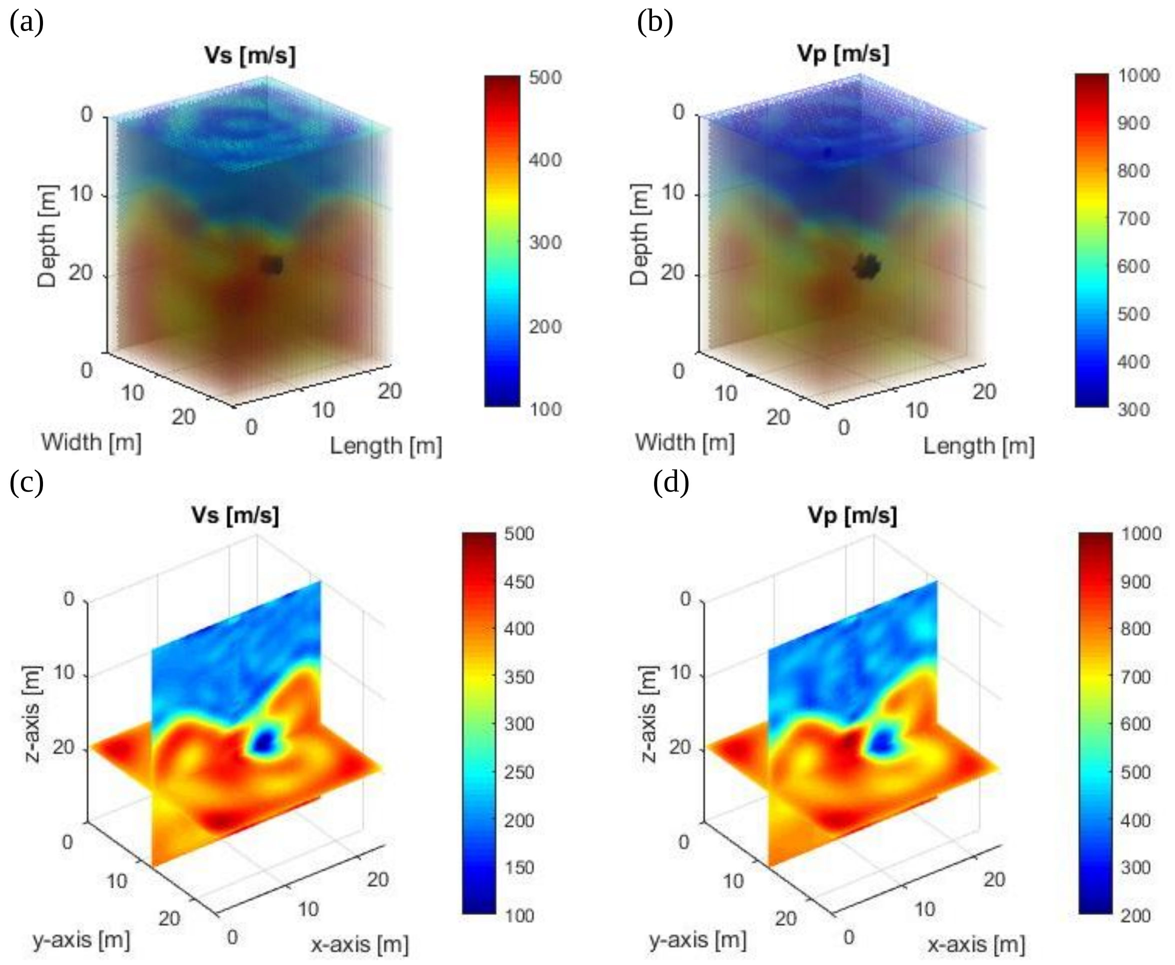

Figure 3.26. Results of test configurations 8 (100 receivers, 25 sources): (a) Inverted 3D V_s model; (b) Inverted 3D V_p model; (c) 2D cross-section view of inverted V_s model; (d) inverted 2D cross-section view of inverted V_p model

Finally, the inverted results for the densest configuration of 100 receivers are shown in Figure 3.26. Both V_s and V_p profiles are well characterized in terms of the layer interface, void location and size, as well as the true velocity values. Compared with the previous cases with fewer receivers, this densest test configuration provides the best results, without any inversion artifacts in both V_s and V_p profiles. The 2D cross-section views of results (Figure 3.24 c and d) clearly show the two variable layers and the void. While excellent results are obtained with this dense test configuration, significant computing time (2 days) is required. As the computer time is proportional to the sum of numbers of sources and receivers, using 100 receivers increases the computer time by 30 % compared to that of 64 receivers, and by 100% compared to that of 36 receivers.

3.3.6 Summary

The 3D SPT-Seismic FWI algorithm was tested on a large model (100 x 80 x 80 ft), using four test configurations with 16 receivers (22.5 ft spacing), 36 receivers (15 ft spacing), 64 receivers (10 ft spacing), and 100 receivers (7.5 ft spacing), and a SPT source interval of 4 ft. By examining inverted results, the algorithm requires the receiver spacing of 15 ft or less for recovering V_s profile, and the receiver spacing of 10 ft or less for recovering V_p profile. Based on accuracy of results and computing demand, the receiver spacing of 10 ft and source interval of 4 ft is also recommended for this large model. The receiver spacing of 15 ft can also be used if only V_s profile is needed.

3.4 Conclusion

This task was to find the minimum number of receivers (max spacing) and sources (max sampling interval) that enabled a successful characterization of variable layers and embedded voids by the 3D SPT-seismic algorithm developed in Task 1. Several test configurations of various spacing intervals of receivers and sources were analyzed. The configurations were tested on two synthetic models with variable soil/rock layers and embedded voids. Accuracy and resolution of inverted V_s and V_p profiles were compared between simulations to identify the optimal test configuration.

The analyses were first performed on a smaller model of 68 × 60 × 60 ft (depth × length × width) with variable layers and an offline void. Four test configurations with 16 receivers (15-ft spacing) and 36 receivers (10-ft spacing), and each with two SPT source intervals of 4 ft and 2 ft were investigated. In all 4 cases, the V_s profile was well characterized by the algorithm, including variable layers as well as location and size of the void. However, the receiver spacing of 15 ft produced inversion artifacts in V_p image. Interestingly, due to data redundancy, the source interval of 2 ft did not improve inverted results, compared to those with the source interval of 4 ft. Thus, analyzing SPT sampling intervals smaller than 4 ft was not necessary.

The inversion analyses were then performed on a larger model of 100 × 80 × 80 ft (depth × length × width), also with variable layers and an offline void. Four test configurations with 16 receivers (22.5-ft spacing), 36 receivers (15-ft spacing), 64 receivers (10-ft spacing), and 100 receivers (7.5-ft spacing), and SPT source interval of 4 ft were tested. By examining inverted results, the SPT-seismic algorithm requires the receiver spacing of 15 ft or less for recovering V_s profile, and the receiver spacing of 10 ft or less for recovering V_p profile.

Based on accuracy of results and computing demand for all eight test configurations, the receiver spacing of 10 ft and SPT source interval of 4 ft is recommended. The receiver spacing of up to 15 ft can be used if only V_s profile is needed (V_p is less accurate). For field experiments, SPT sampling at 2- to 4-ft intervals should be used, in cases where averaging data to enhance signal-to-noise ratio or removing blows with poor data is required. These optimal test configurations will be applied to field experiments in Task 3.

Chapter 4 – VERIFICATION OF 3D SPT-SEISMIC FWI ALGORITHM AT FIELD TEST SITES (TASK 3)

4.1 Introduction

This task is to validate the 3D SPT-seismic Full Waveform Inversion (3D SPT-seismic FWI) algorithm, developed in Task 1, to assess its efficacy in identifying voids away from SPT locations and characterizing variable soil/rock layers. Field experiments were conducted at 3 test sites (Newberry, Bell, and Kanapaha) for the validation. For each test site, a 2D grid of geophones were deployed on the ground surface to record seismic waves generated by a SPT hammer at depths. The optimal test configurations (geophone spacing and SPT sampling intervals) identified in Task 2 were used for field experiments in this task. Recorded SPT-seismic data were analyzed by the 3D SPT-seismic FWI algorithm, and results were compared to SPT-N values for assessment of the method's capability. Key outcomes of this task included the 3D visualization of seismic results, illustrating soil/rock layering, pinnacles, and void identification. Details on data acquisition, analysis, visualization, and validation are provided in subsequent sections.

4.2 Newberry site

The field experiments were first conducted at Newberry site (Fig. 4.1a). It is a dry retention pond, consisting of fine sand and silt layers underlain by weathered and karst limestone. The top of limestone is typically from 2 to 10-m depth over the site, with exception of a few locations where limestone is seen on the ground surface. The site is prone to sinkhole activity, and a number of voids have been found at shallow depths of a few meters (Mirzanejad et al., 2020a).

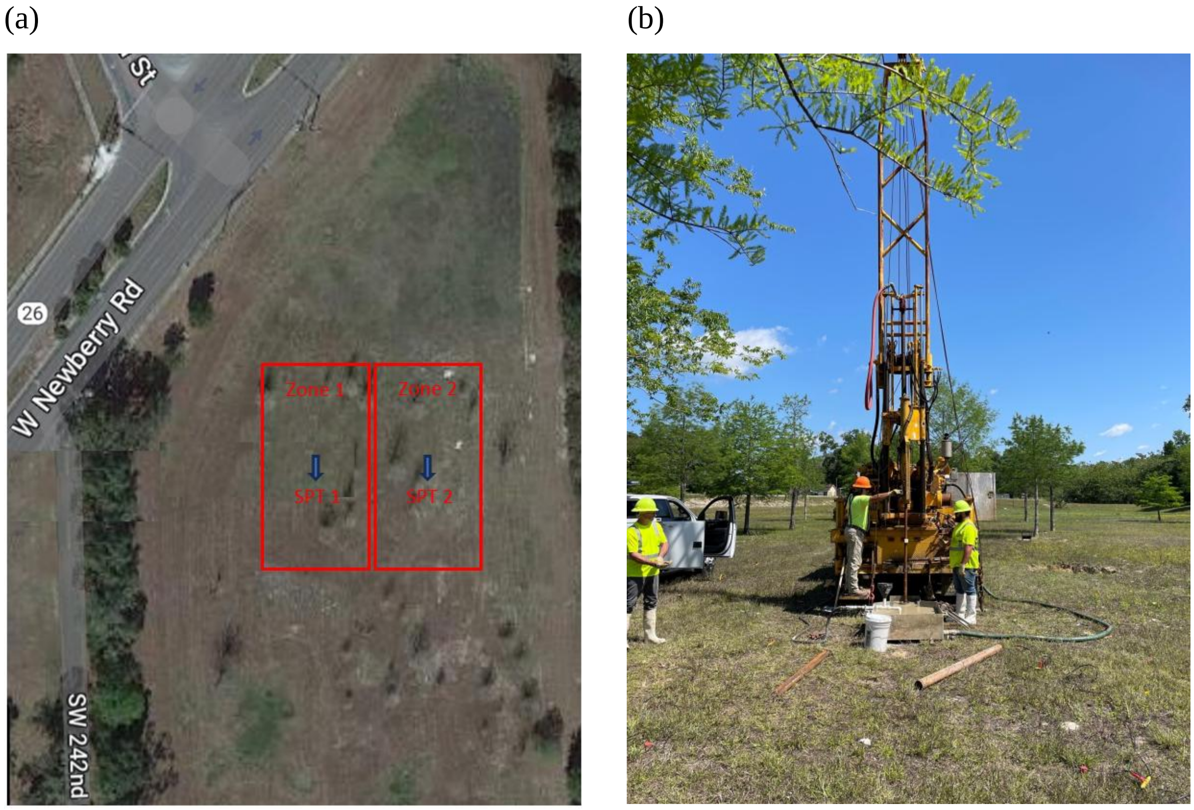

Figure 4.1. Field experiment at Newberry site: (a) two test zones with an SPT at the center of each zone; (b) site photo with the SPT rig

4.2.1 Data acquisition

Data acquisition was performed for two test zones of 36 × 18 m (120 × 60 ft), each with an SPT at the center as shown in Fig. 4.1a. For each zone, 72 vertical geophones of 4.5-Hz resonance frequency were used on the ground surface, covering a 6 × 12 grid of 3 m spacing as shown in Fig. 4.2. This test configuration was selected based on our parametric studies (Task 2). A 2D grid of geophones at 3 m (10 ft) spacing (or less) is required to achieve acceptable accuracy and desired resolutions at submeter pixels.

The SPT rig was used as the seismic source. For each source location at depth, the 140-lb SPT hammer was dropped 30 inch, striking the top of SPT rod (above the ground surface), and imparting energy that propagated to the SPT spoon (attached at the end of SPT rod), which acted as the in-depth seismic source and induced seismic wavefields at depths. At each hammer strike (blow), the seismic trigger, mounted on the SPT rod, activated the seismograph for data recording.

SPT#1 was conducted to 18.9-m depth (63 ft), with intervals of 0.45 m (1.5 ft) above 6-m depth (20 ft) and 1.5 m (5 ft) below 6-m depth (20 ft). SPT-seismic data were recorded for 5 to 10 blows at each interval, for a total of 146 blows from the ground surface to the bottom of boring. From about 13 to 17 m depth (43-56 ft), the weight of hammer was recorded for the SPT blow counts (N = 0), suggesting a void that could be partially filled with raveled soils. It is noted that no seismic data were recorded at the void depth.

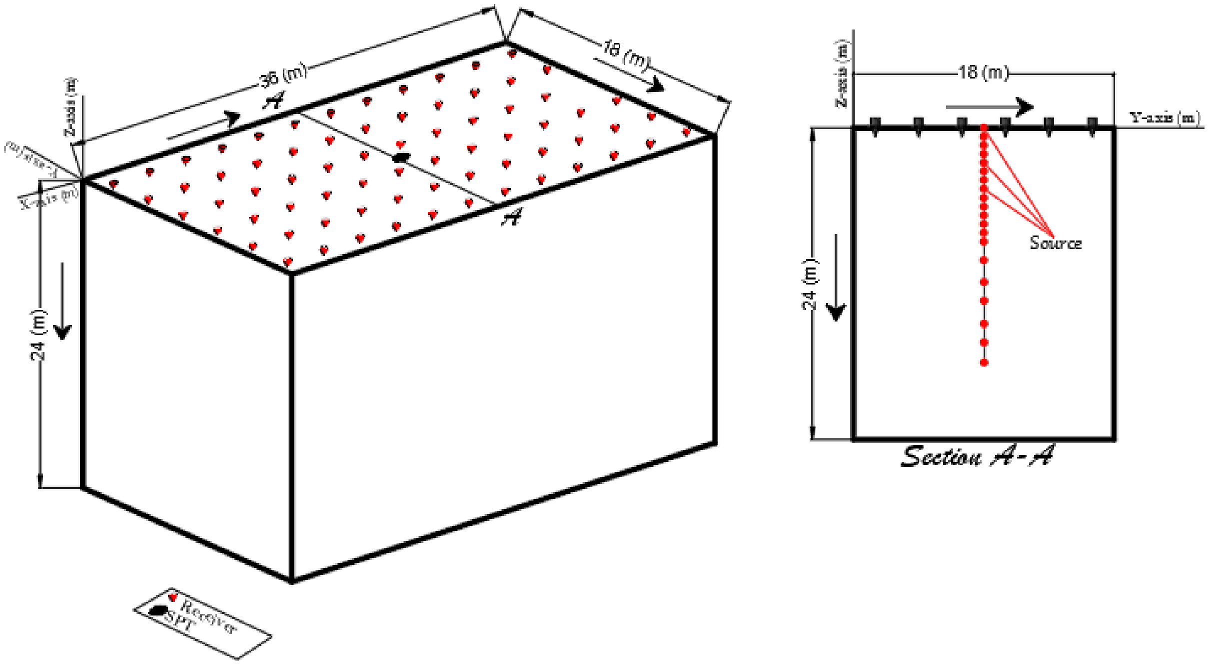

Figure 4.2. Test configuration used for each test zone, with 72 geophones placed on the ground surface in a 6 × 12 grid of 3-m spacing and SPT at the center of the geophone array

Similar to zone 1, SPT#2 was conducted to a depth of 18.10 m (60 ft) at intervals of 0.45 m (1.5 ft) above 6-m depth (20 ft) and 1.5 m (5 ft) below 6-m depth (20 ft). Seismic data were recorded for 102 blows from the ground surface to the maximum SPT depth, with 5 to 10 blows at each SPT interval. From about 5 to 9 m depth, the weight of rod or weight of hammer were recorded (SPT-N values = 0), suggesting that a void filled with air and some raveled soils. In addition, a complete loss of drilling fluid circulation happened at 17.1-m depth (57 ft), suggesting another void.

Shown in Figure 4.3 is the measured field data for the deepest source at 18.9-m depth (63 ft). The data were filtered through 10-40 Hz bandwidth (Figure 4.3a) with the corresponding frequency spectra (Figure 4.3b). The wavefield emitted from this deep source location arrived at all receivers with a consistent propagation pattern in both magnitude and phase. It suggests that the SPT hammer provided sufficient wave energy at the depth required for propagating over large distances (26 m to the farthest geophone) to the ground surface. A similar quality of measured data was obtained for most blows.

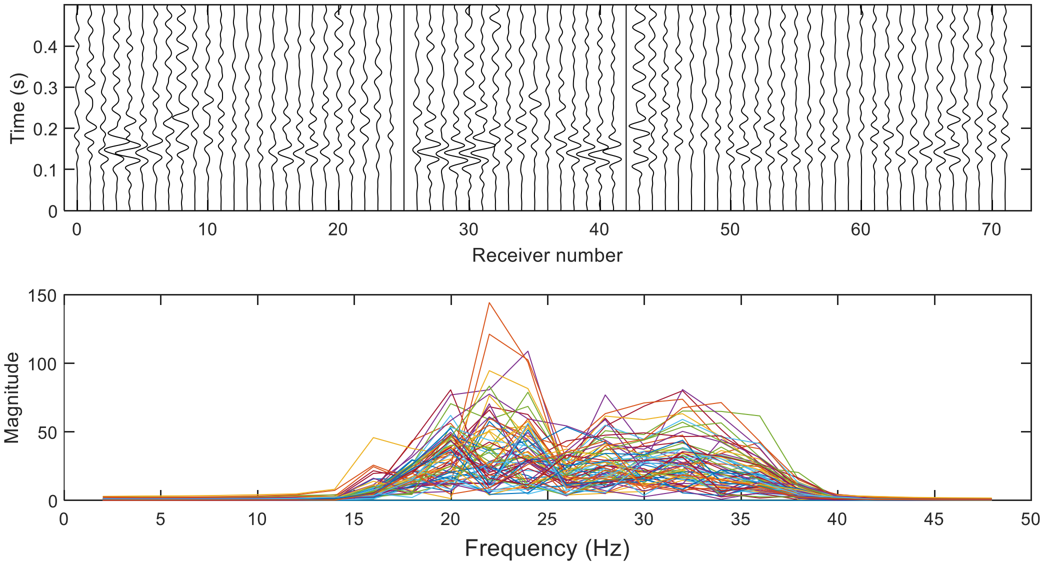

Figure 4.3. Field experimental data for the deepest source at 63-ft depth

4.2.2 Data analysis

Test zone 1

For inversion, the analyzed medium of 24 × 36 × 18 m (80 × 120 × 60 ft, depth × length × width) was discretized into cells of 0.60 × 0.75 × 0.75 m (2 × 2.5× 2.5 ft, depth × length × width). The source locations (actual depths of SPT spoon) were assigned to nearest numerical nodes (0.6-m vertical spacing) for wave simulation. One hundred forty-six blows were assigned to 20 depths, and data from blows at the same depth were averaged to enhance signal quality.

Based on the spectral analysis of surface data at the site, a 1D initial velocity model (Fig. 4.4) was taken with V_s linearly increasing from 200 m/s for soil on the surface and to 500 m/s for limestone at the model bottom (24-m depth). The initial V_p was assumed to be twice the initial V_s. The inversion started on the initial model (Fig. 4.4) using waveform data filtered through 10-40 Hz bandwidth. The inversion stopped at a preset maximum number of iterations (100 iterations) and took about 26 hours on a desktop computer (32 cores of 3.4 GHz, and 512 GB of RAM).

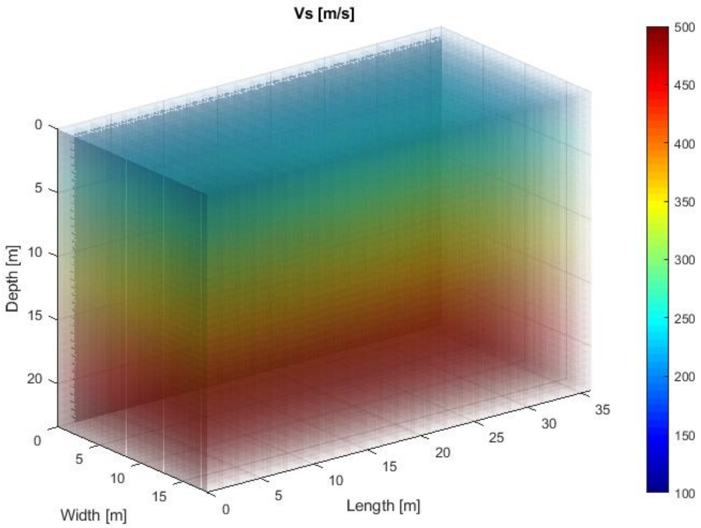

Figure 4.4. Initial V_s used for inversion of data from both test zones, and initial Vp as 2 × V_s (not shown)

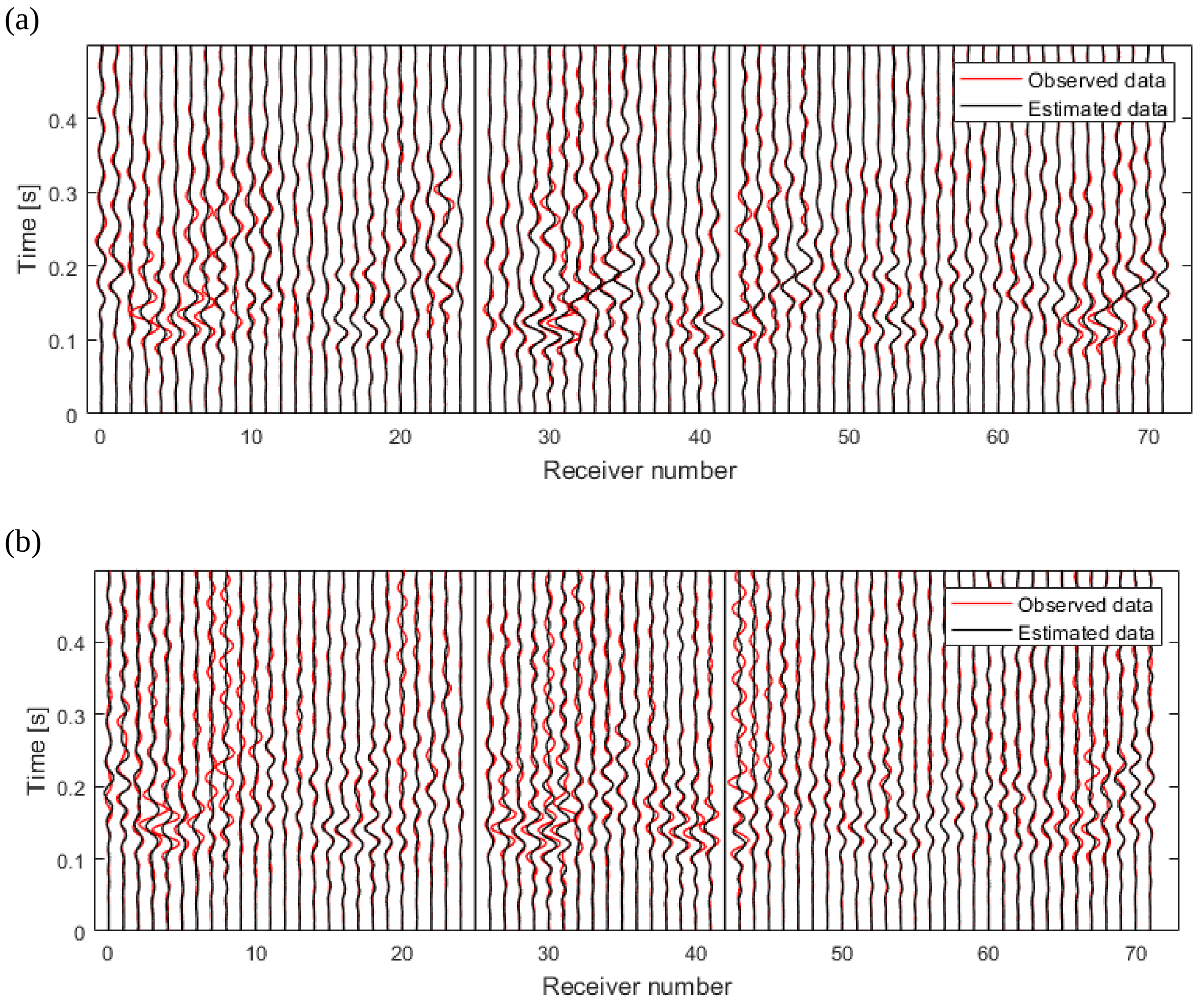

Figure 4.5. Test Zone #1 — Waveform comparison between observed and estimated data for two sources: (a) 11.0 m depth (just above the void) and (b) 18.9 m depth (deepest source). Data from two poor channels were excluded from the analysis.

Figure 4.5 is the comparison of waveform data for two source locations at 11-m (36 ft) depth (above the void) and 18.9-m (63 ft) depth (deepest source). The estimated and observed (measured) data matched well at the end of analysis. No cycle skipping (matching of wrong peak) is observed, confirming that inversion converged to the global minimum. Figure 4.6 shows the normalized error for all 100 iterations. The error reduced continuously from 1.0 at the beginning to 0.67 at the end of analysis. The remaining error (waveform misfit) is due to the fact that the field conditions (noise, damping, soil/rock properties) were not fully captured by the forward simulation and model update. Nevertheless, the final estimated data mimics the field data (Fig. 4.5).

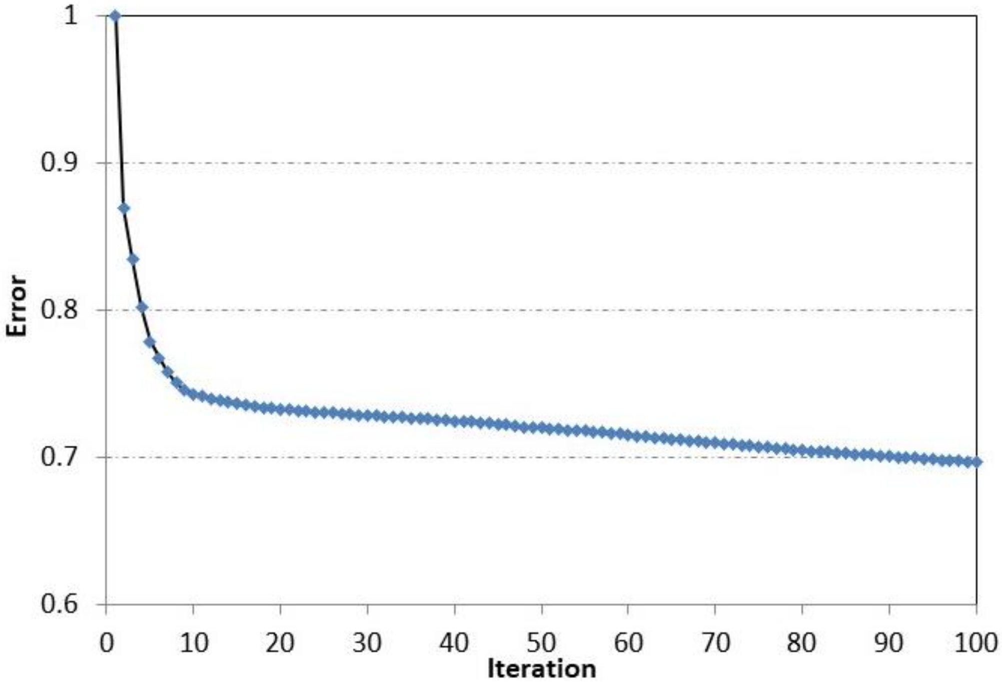

Figure 4.6. Test zone #1: normalized least-squares errors of all 100 iterations

Shown in Fig. 4.7 are the final inverted results. V_s profile (Fig. 4.7, left) contains two distinct layers: 1) a soft layer with V_s ~ 200 m/s from 0 to about 7-m depth (0 to 23 ft) and 2) a stiff layer with V_s ~ 500 m/s from 7 to 24-m depth (23 to 80 ft). They agree with the material samples from SPT with soil underlain by limestone. Importantly, a large low-velocity zone (V_s ~100 m/s) is found at the middle of medium from about 13 to 17 m depth (43 to 56 ft). The V_p profile (Fig. 4.7, right) is similar to the V_s profile, including the existence of the low-velocity zone and soil/limestone layers.

The 3D rendering of inverted V_s and V_p are shown in Figure 4.8. Both profiles exhibit the shallow soil layer underlain by the limestone layer. The top of limestone varies from 6 to 8 m depth (20-27 ft) below the test area of 36 × 18 m (120 × 60 ft). In Fig. 4.8 a, two separate voids are imaged in the middle of medium near 15-m depth (50 ft). One void intersects with the SPT borehole; the other void is off-line and was not identified by the SPT. V_p image (Fig. 4.8 b) is consistent with V_s image. Compared to the 1D SPT, the seismic results provide much more information on the subsurface profile such as locations and 3D dimensions of voids and 3D soil or rock variation.

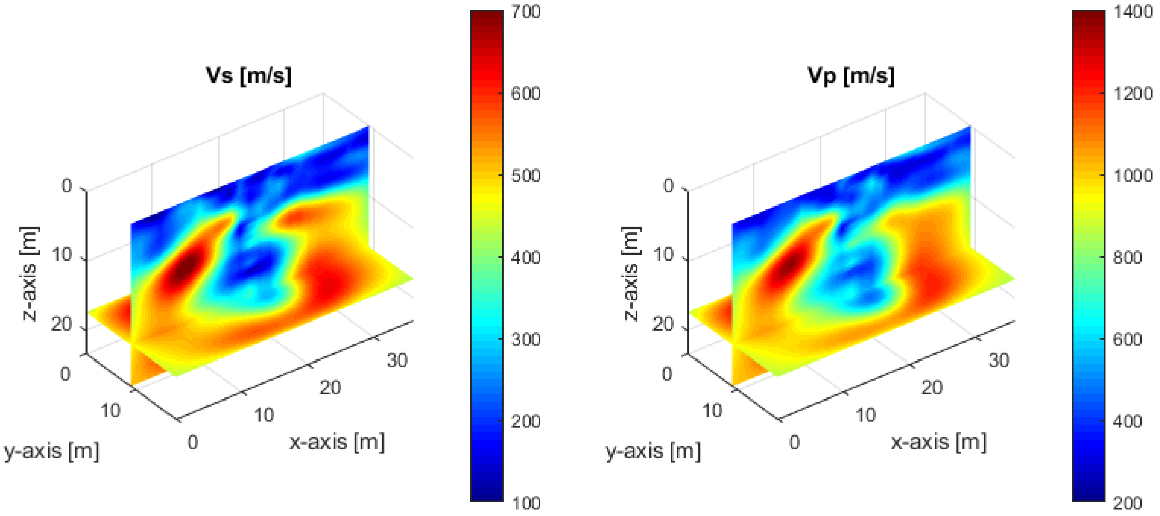

Figure 4.7. Newberry test zone #1: 2D cross-section view of inverted V_s and V_p

(a)

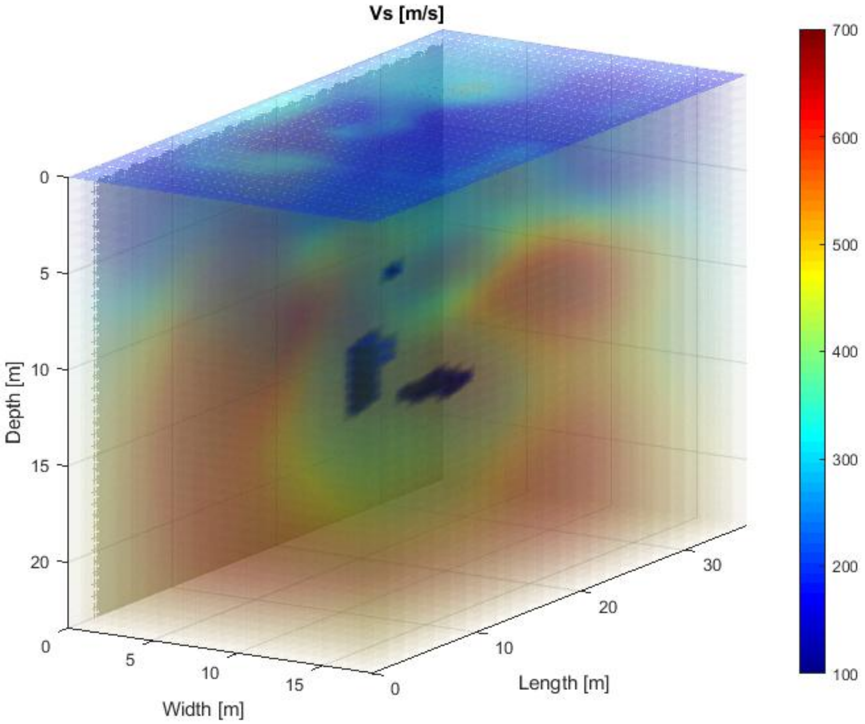

(b)

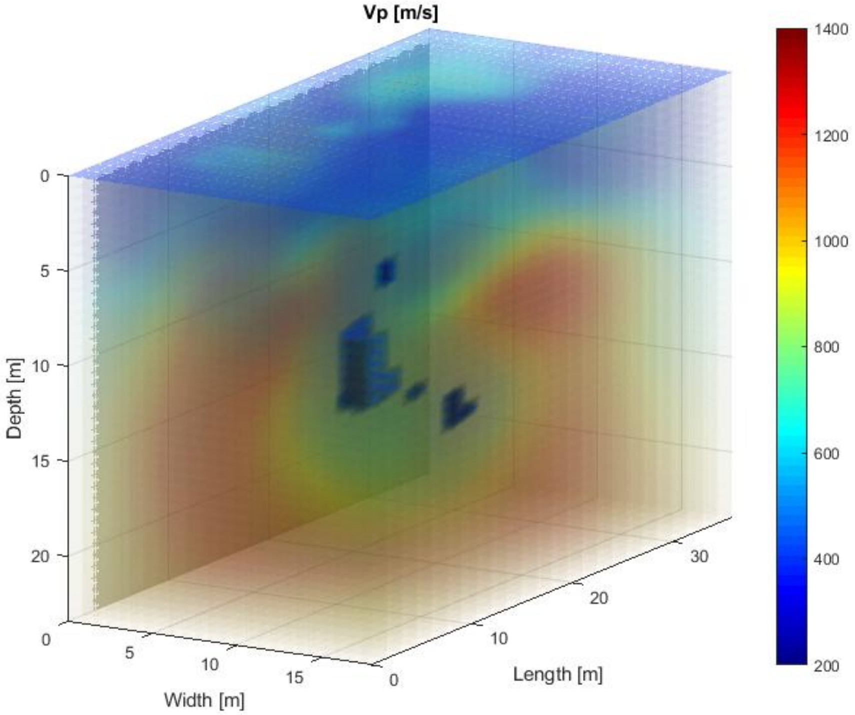

Figure 4.8. Newberry test zone #1: 3D rendering of inverted V_s (a) and V_p (b)

Test zone 2

Data analysis was performed in the same manner as that of zone 1. The analyzed medium of 24 × 36 × 18 m (80 × 120 × 60 ft in depth × length × width) with cells of 0.60 × 0.75 × 0.75 m (2 × 2.5× 2.5 ft in depth × length × width) were used. The 102 blows were assigned to 19 depths, and data from blows at the same depth were averaged to reduce noise and improve signal quality. The inversion started on the same initial model (Fig. 4.4) using 10-40 Hz data and stopped after 100 iterations.

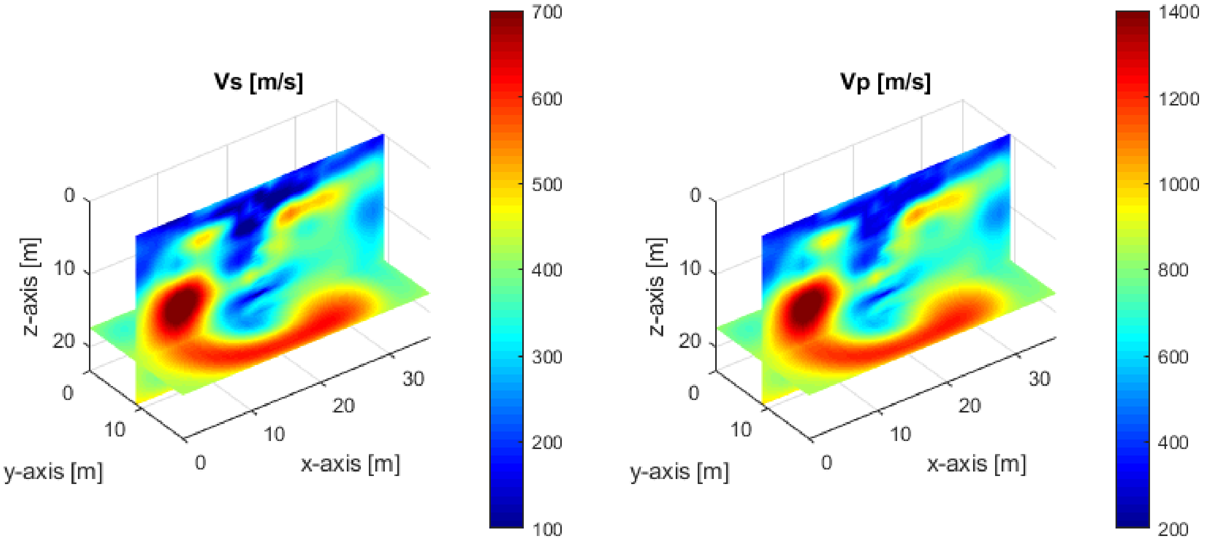

Figure 4.9. Newberry test zone #2: 2D cross-section view of inverted V_s and V_p

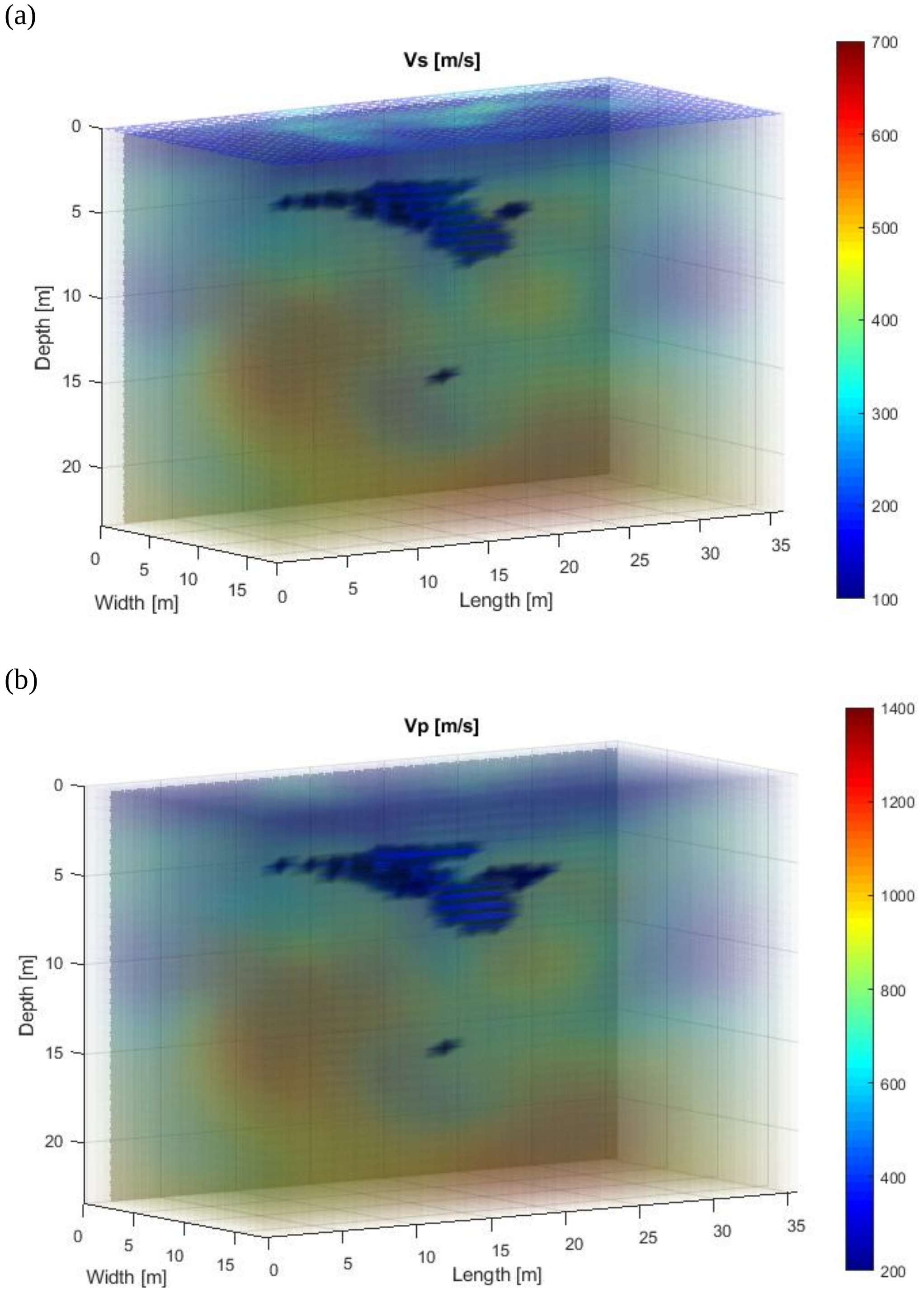

Figure 4.10. Newberry test zone #2: 3D rendering of inverted V_s (a) and V_p (b)

The final inverted results are shown in Fig. 4.9. V_s profile (Fig. 4.9, left) consists of a soft layer with $V_s \sim 200$ m/s from 0 to about 5-m depth (0 to 17 ft), and limestone layer below 5-m depth (17 ft). It contains a large low-velocity anomaly (V_s <100 m/s) at shallow depths (5-10 m) and a deeper low-velocity anomaly (V_s <150 m/s) at below 15-m depth (50 ft). V_p profile (Fig. 4.9, right) is similar to V_s profile, regarding the soil/rock layers and low-velocity anomalies. For better visualization, Figure 4.10 shows 3D rendering of inverted V_s and V_p. Both profiles exhibit the shallow soil layer underlain by the limestone layer. The large low-velocity anomaly is clearly imaged at between 5 to 10 m depth (17 to 33 ft), and the deep anomaly is also shown at about 17 m depth (56 ft).

4.2.3 Verification

The comparison of inverted V_s to SPT-N values at the two SPT locations is shown in Fig. 4.11. For test zone 1, Figure 4.11a shows the initial and inverted V_s profiles at the SPT location, together with SPT-N (blow counts) values of SPT 1. Apparently, V_s values changed significantly during the inversion. At the void location from 13-17 m depth (43 to 56 ft), the cell V_s changed from the initial values of about 400 m/s to the final values of about 120 m/s. The final V_s profiles generally agree with SPT-N values, including a high-velocity zone about the void at 10-12 m depth (33-40 ft), and the low-velocity zone at the void location of 13-17 m depth (43 to 56 ft).

For test zone 2, the initial and inverted V_s profiles at the SPT location are shown in Fig. 4.11b, together with SPT-N values of SPT 2. The good agreement between inverted V_s and SPT-N values is observed from the ground surface to 13-m depth (43 ft). Both profiles show low values from 5 to 10 m depth (17-30 ft) at the void location, and high values at about 3-m (10-ft) and 13-m (43-ft) depths. While there exist discrepancies between V_s and SPT-N values below 13-m depth

(43 ft), the complete loss of drilling fluid circulation at 17.1-m depth (57 ft) suggests that the SPT is next to the offline void in rock (shown as the deep anomaly in Fig. 4.10).

However, the SPT-N values are more erratic than the V_s for both SPTs. This is due to the SPT-N values representing the local soil properties at the device's tip, while V_s values represent average material properties of a 0.60 × 0.75 × 0.75 m (2 × 2.5× 2.5 ft) cell. In addition, the regularization used in Eq. 5 tends to tie a cell to its 6 adjacent cells (top, bottom, left, right, front and back), leading to smooth inverted models. Nevertheless, the SPT-seismic FWI was able to detect buried voids and characterize the subsurface soil/rock properties over large 3D volumes.

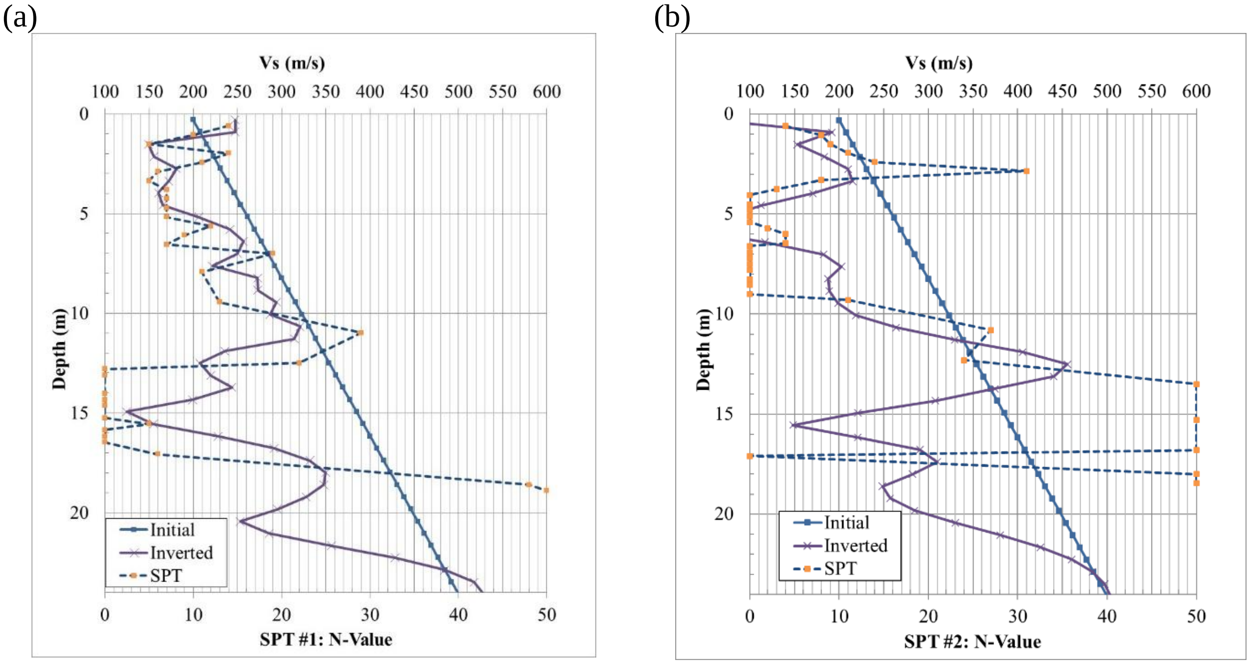

Figure 4.11. Newbery site: comparison of V_s with SPT N-values: (a) SPT 1 and (b) SPT 2

4.3 Bell site

4.3.1 Data acquisition

Figure 4.12. Field experiment at Bell site: test site photo with the SPT. The 72 geophones (6 × 12 grid) were placed over a test area of 60 x 120 ft. The SPT location is at the center of the test area

The SPT-seismic FWI method was subsequently tested at the Bell site (Fig. 4.12). The data acquisition involved deploying 72 vertical geophones with a resonance frequency of 4.5 Hz across a 6 × 12 grid with 3 m (10 ft) spacing, as depicted in Fig. 4.2. Using the SPT rig as a seismic source, the 140-lb SPT hammer was dropped from a height of 30 inches, impacting the top of the SPT rod above the ground surface. This impact transferred energy, propagating to the SPT spoon attached at the end of the rod, functioning as the in-depth seismic source. The SPT spoon induced seismic wavefields at various depths. With each hammer strike, the seismic trigger mounted on the SPT rod activated the seismograph for data recording. The recording process encompassed 116 blows, ranging in depth from 0 to 15.24 m (0-51 ft), providing a comprehensive dataset for subsequent analysis.

4.3.2 Data analysis

Data from all 116 blows from the ground surface to 15.24-m depth (51 ft) were used for analysis. Figure 4.13 shows the measured data for the deepest source. The data were filtered through a 5-40 Hz bandwidth. The wavefield displays a consistent propagation pattern in both magnitude and phase across most receivers. A similar quality of measured data was observed for all other shallower source locations, ensuring reliability and coherence throughout the dataset.

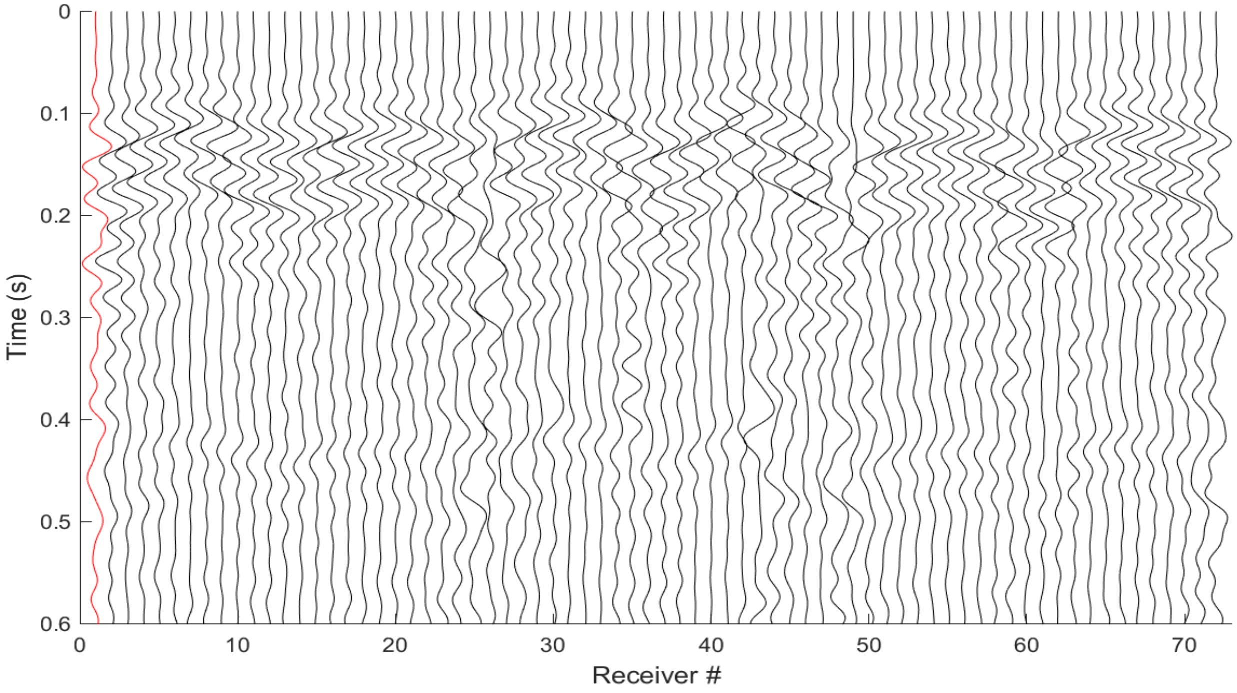

Figure 4.13. Bell site: experimental data for the deepest source at 51-ft depth

For the inversion process, the analyzed medium is 24 × 36 × 18 m (depth × length × width). Source locations, corresponding to the actual depths of the SPT spoon, were assigned to the nearest numerical nodes with vertical spacing of 0.61 m or 2 ft for wave simulation. The 116 blows were distributed across 15 depths from 0 to 15.24 m (0-51 ft) at intervals of 0.45 m (1.5 ft) or 1.5 m (5 ft), as illustrated in Fig. 4.14. To enhance signal quality, data from blows at the same depth were averaged.

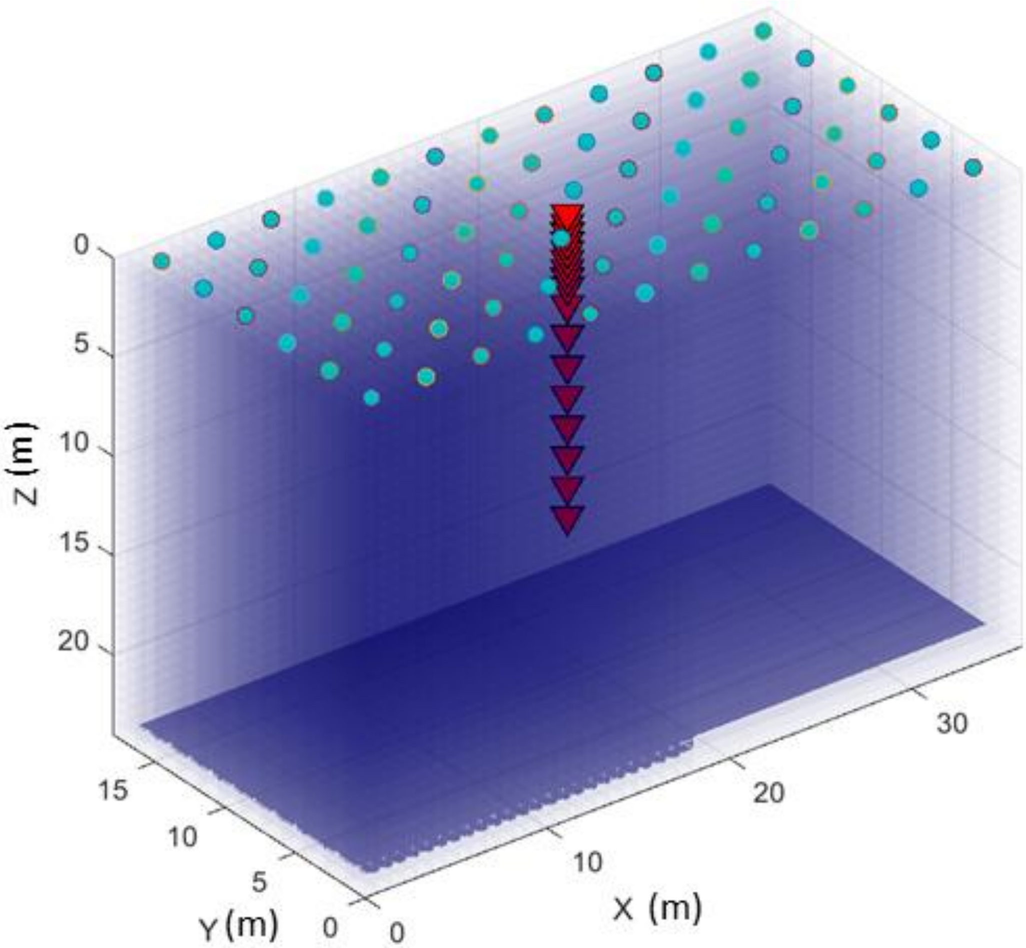

Figure 4.14. Field experiment test configuration with sources (red triangle) and receivers (cyan circle)

Following spectral analysis of the data, a 1D initial velocity model (Fig. 4.15) was established, with V_s linearly increasing from 200 m/s for surface soil to 400 m/s for limestone at the model bottom. The initial V_p was assumed to be twice that of the initial V_s. The inversion commenced with the initial model (Fig. 4.15), using waveform data filtered through a 10-35 Hz bandwidth. The stopping criteria were set as that the inversion stopped at the maximum number of iterations (100 iterations), or when the error changed by less than 0.1% from the previous iteration for three consecutive iterations.

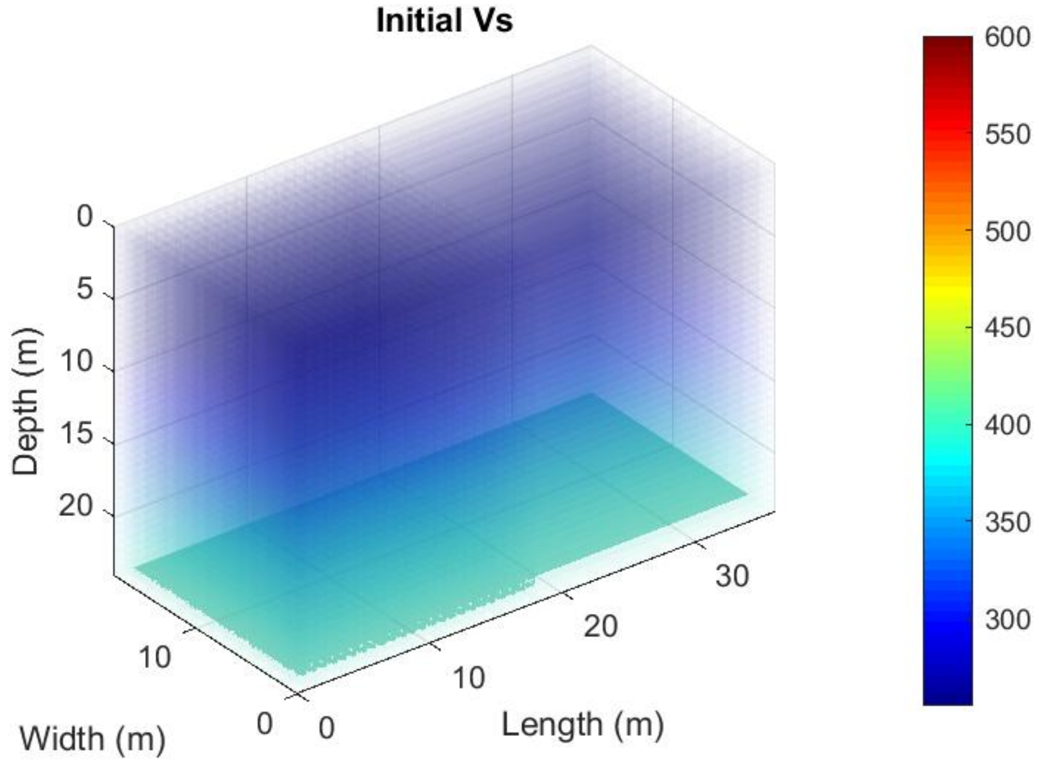

Figure 4.15. Initial V_s used for inversion, and initial V_p as 2 × V_s (not shown)

A detailed comparison between the estimated and observed (field) data is shown in Fig. 4.16 for the deepest source at 51 ft depth. The strong agreement between the estimated and field data confirms the accuracy of the analysis. Importantly, no cycle skipping affirms that the analysis converged to the global solution.

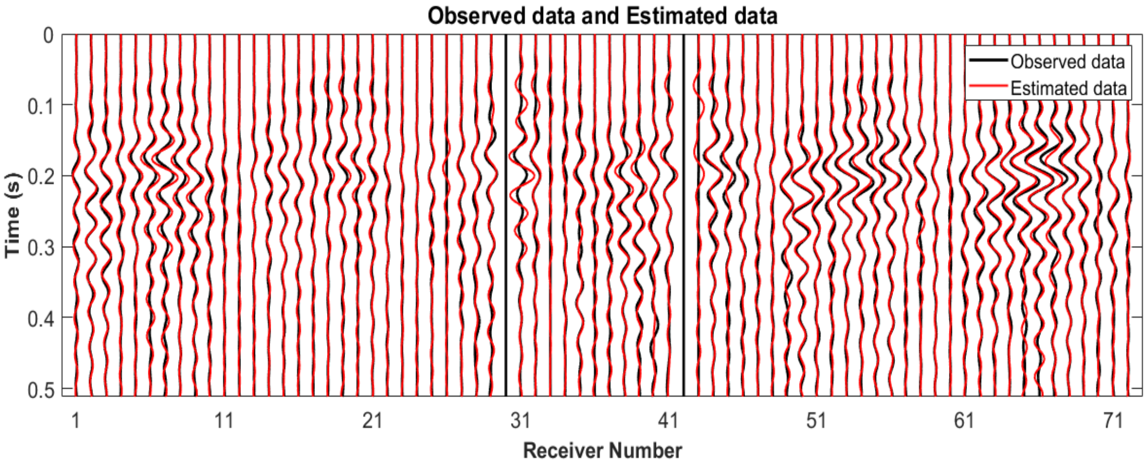

Figure 4.16. Field experiment: waveform comparison between observed data and estimated data) for the deepest source at 51-ft depth. Poor channels are removed from analysis

In Fig. 4.17, the normalized error for all iterations is depicted, revealing a consistent reduction from 1.0 at the start to 0.74 at the conclusion of the analysis. The remaining error is attributed to the fact that the field conditions including noise, damping, and soil/rock properties, were not entirely captured by the forward wave simulation. Despite these challenges, the final estimated data closely mimics the field data, as illustrated in Fig. 4.16.

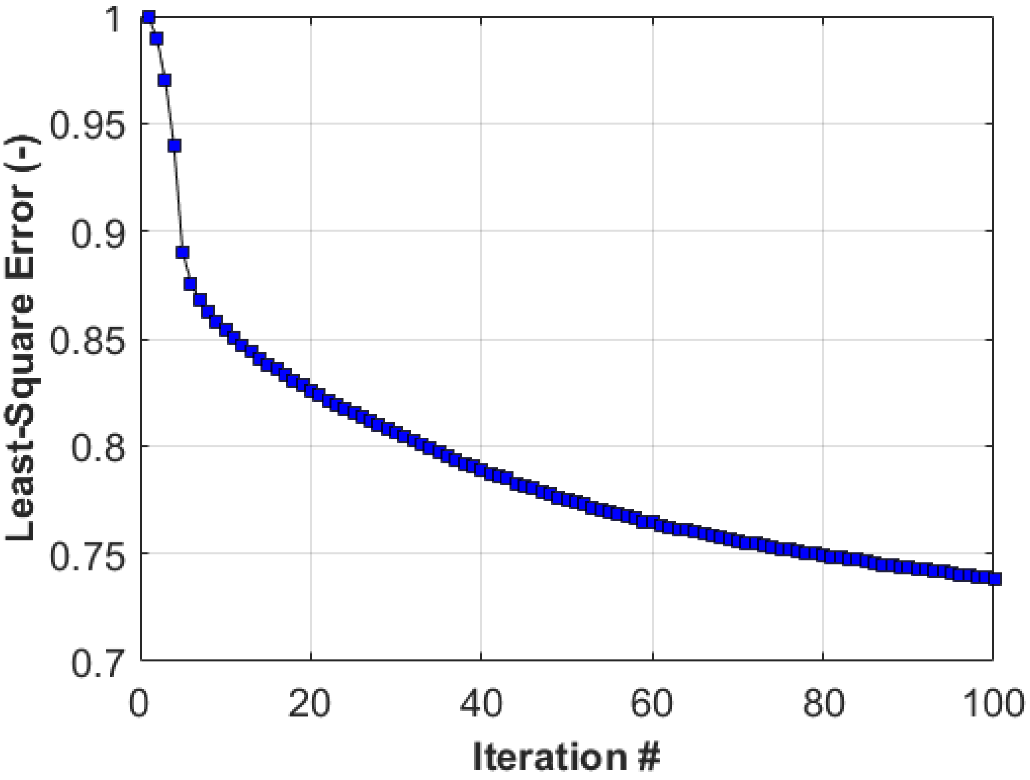

Figure 4.17. Bell site: normalized least-squares errors of all 100 iterations

The final inverted results are shown in Fig. 4.18. The V_s profile (Fig. 4.18, left) delineates five distinct layers: 1) a stiff layer (V_s ~250 m/s) near the ground surface, 2) two soft layers (V_s ~150 m/s) at about 3 to 5 m depth (10-17 ft) and 12 to 17 m depth (40-57 ft), and 3) two stiff layers (V_s ~550 m/s) at 6 to 12 m depth (20-40 ft) and at the bottom. The V_p profile (Fig. 4.18, right) mirrors the V_s profile.

As shown in Fig. 4.19, the 3D rendering of the inverted V_s and V_p profiles illustrates a soft soil layer overlaying the limestone layer. The limestone layer varies from 6 to 15 m below the surface in the test area of 36 × 18 m. The soft layers are distinctly visualized as the blue zone in the figure.

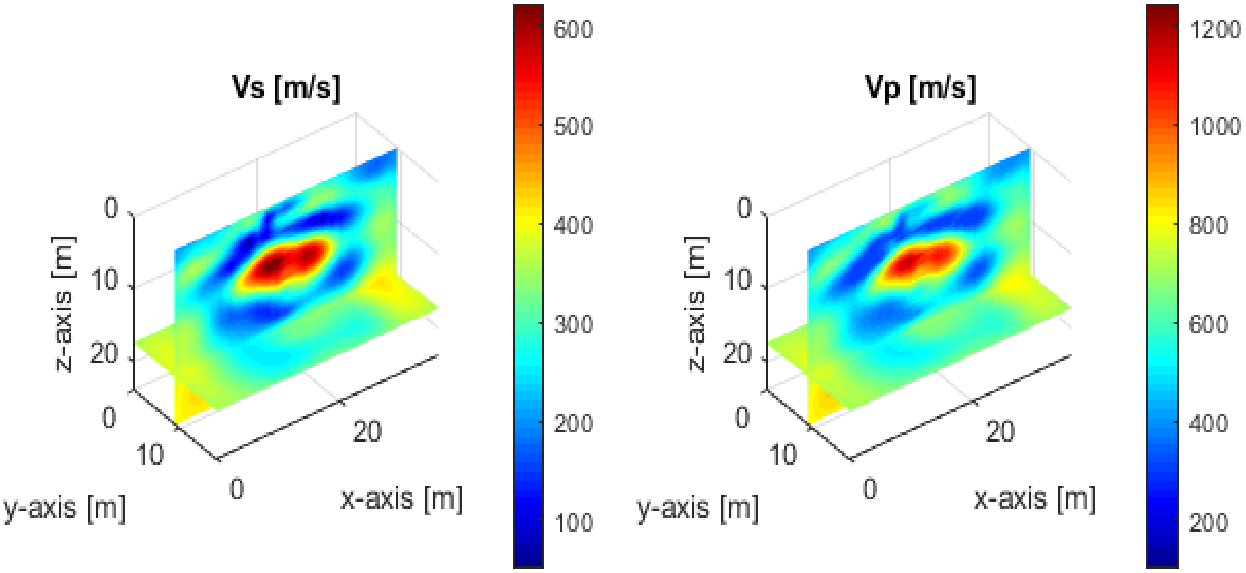

Figure 4.18. Bell site: 2D cross-section view of inverted V_s and V_p

(a)

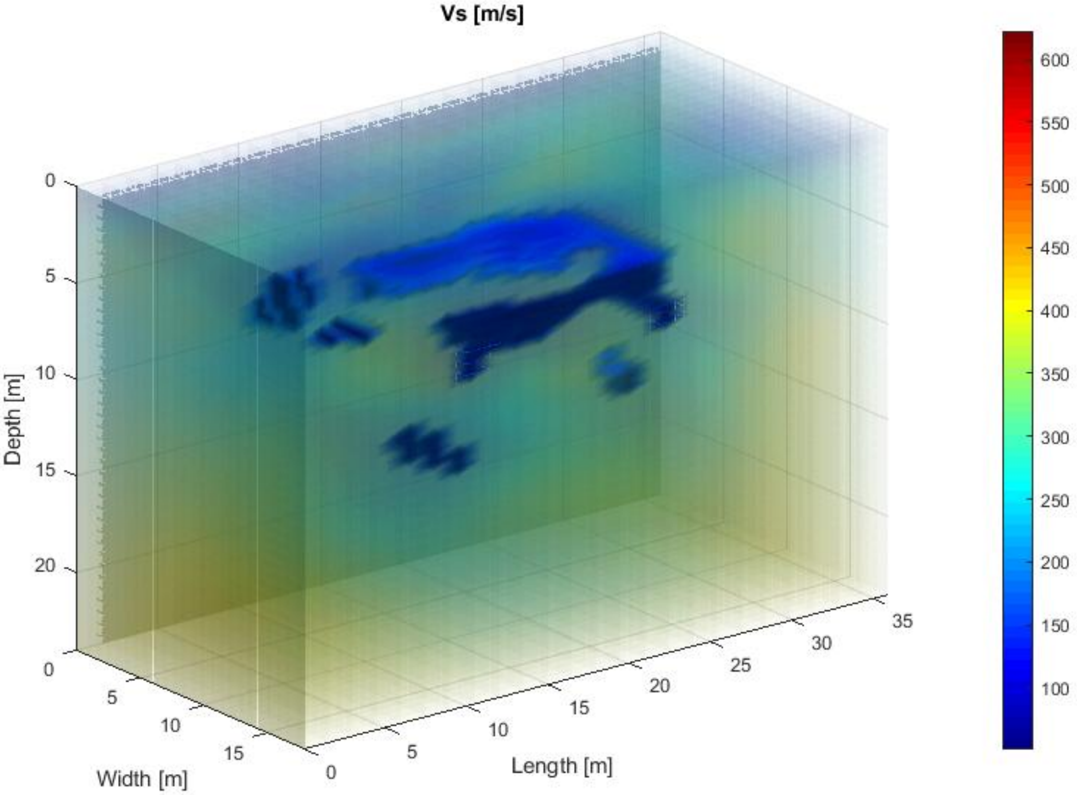

(b)

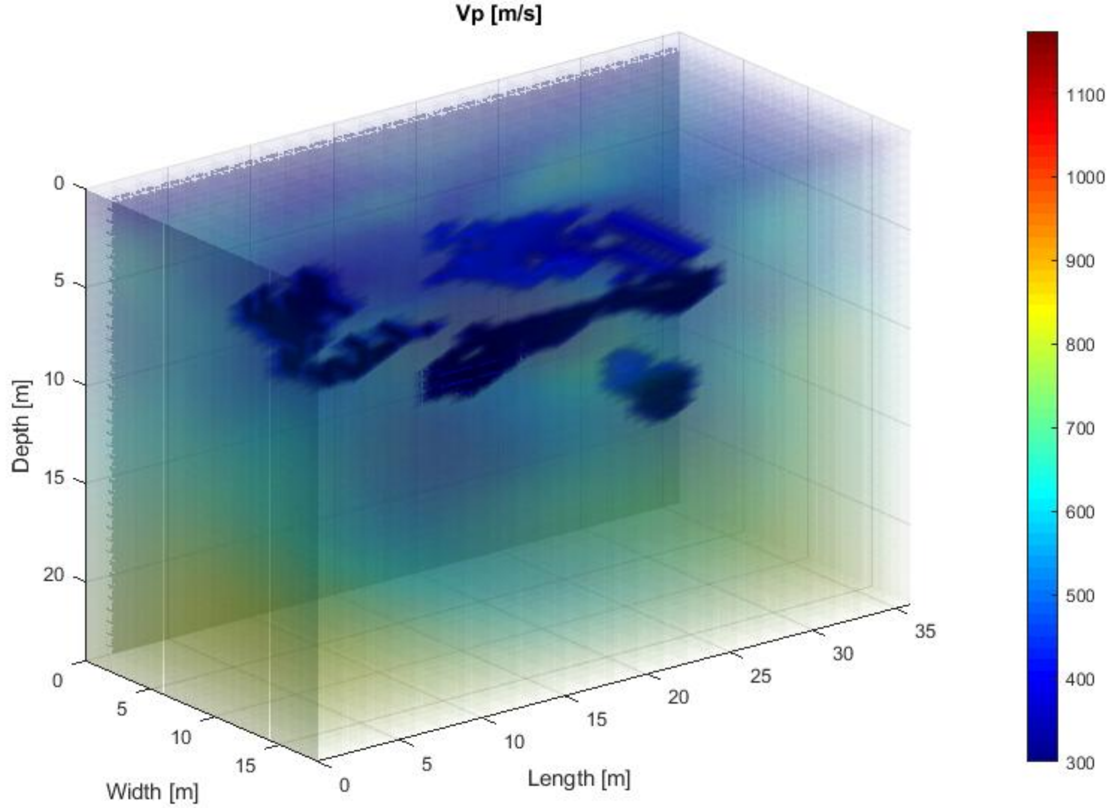

Figure 4.19. Bell site: 3D rendering of inverted V_s (a) and V_p (b)

4.3.3 Verification

Figure 4.20 depicts the initial and final inverted V_s profiles at the SPT location, accompanied by SPT-N (blow counts) values. V_s values changed significantly during inversion from the initial values to the final values, suggesting the algorithm is robust. The final inverted V_s profiles well correlate with SPT-N values, revealing a high-velocity zone at 6-15m depth and a low-velocity zone between 15-17 m depth. The SPT-seismic FWI effectively characterizes subsurface soil/rock stratigraphy and properties, providing valuable insights into the presence of a soft material zone beyond the boring depth.

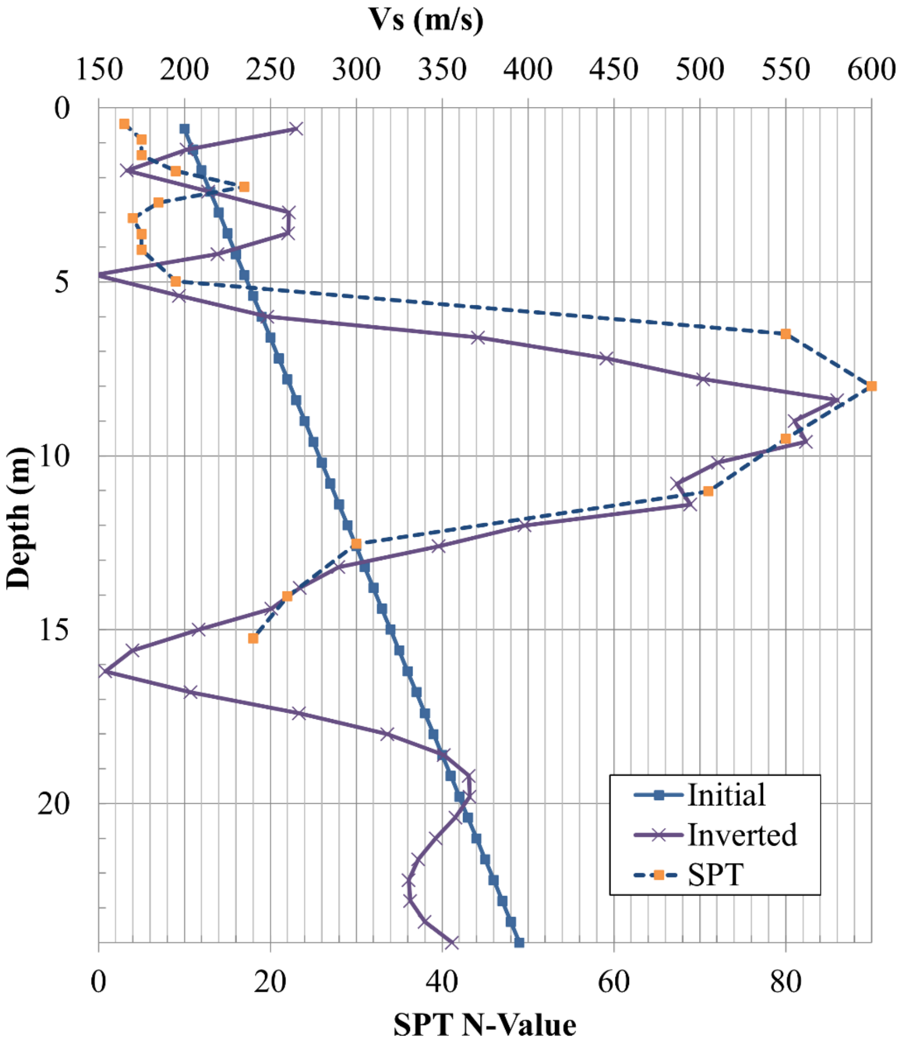

Figure 4.20. Comparison of inverted V_s with SPT N-values

4.4 Kanapaha site

4.4.1 Data acquisition

The SPT-seismic FWI method was then tested at Kanapaha site, Florida (Fig. 4.21). The same test equipment and configuration as those of the previous sites were used for this site. Data acquisition involved the deployment of 72 vertical geophones, arranged in a 6 × 12 grid at 3-meter spacing (10 ft), as illustrated in Fig. 4.2. One SPT was conducted at the center of the test area down to 17.4 m (58 ft). SPT-seismic data were recorded for 100 blows from 0 to 17.4 m depth (0-58 ft), providing a complete dataset for analysis. Weight of hammer was recorded at about 11 m (34 ft depth), suggesting a small void or very soft material exists.

Figure 4.21. Field experiment at Kanapaha site: photo with the SPT rig. The 72 geophones (6 × 12 grid) were placed over a test area of 60 x 120 ft. The SPT location is at the center of the test area

4.4.2 Data analysis

All data from 100 blows were used for analysis. Figure 4.22 depicts the collected data from the first source on the ground surface. The wavefield exhibited a consistent propagation pattern in both magnitude and phase across the geophone array. The analyzed medium is 24 × 36 × 18 m (80 × 120 × 60 ft in depth × length × width). Source locations, aligned with the actual depths of the

SPT spoon, were assigned to the nearest numerical nodes with a vertical spacing of 0.60 m (2 ft) for wave simulation. The 100 blows were distributed at 15 depths ranging from 0 to 17.4 m (0-58 ft). Data from blows at the same depth were averaged to enhance the quality.

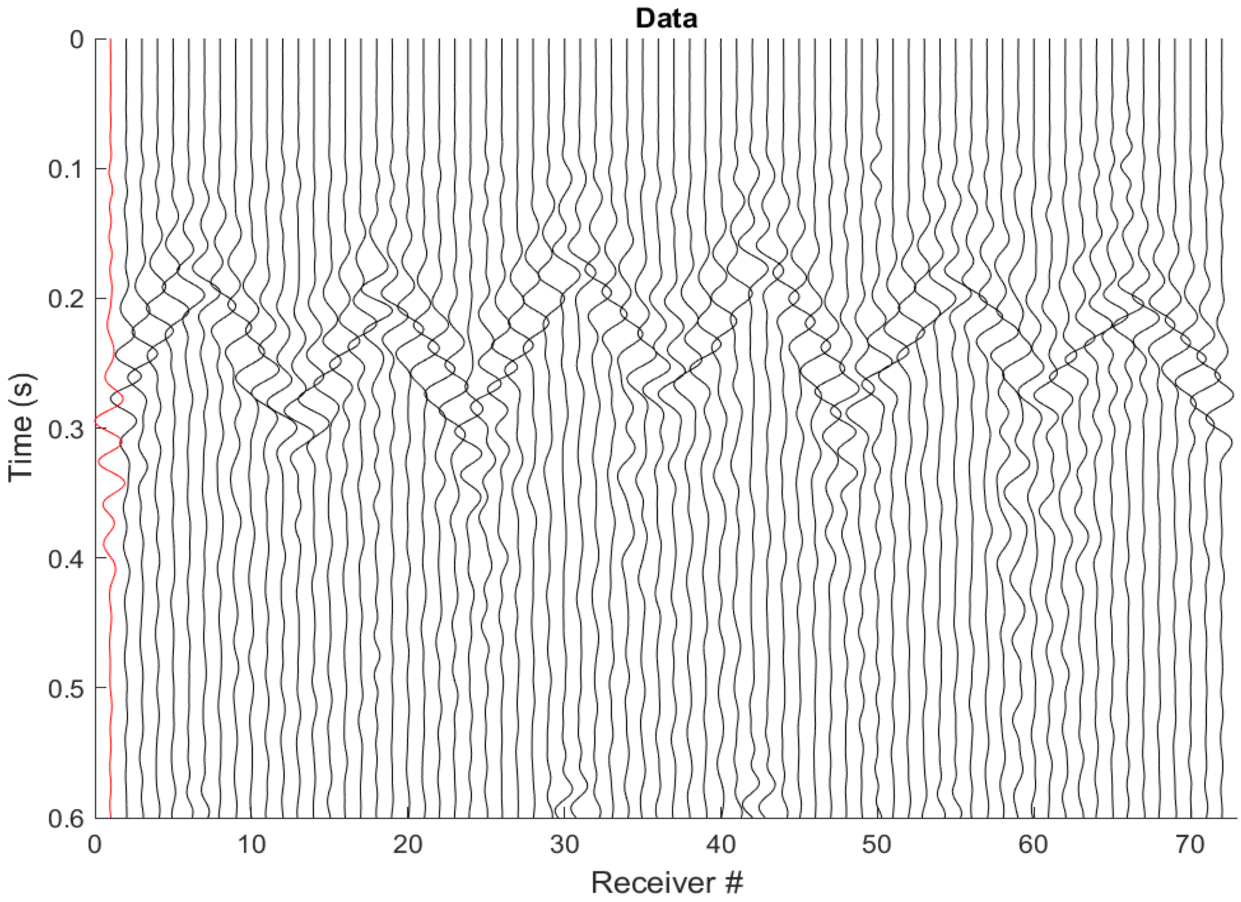

Figure 4.22. Field experimental data for a sample source on the surface

Based on spectral analysis of measured data, a 1D initial velocity model was estimated as shown in Fig. 4.23. In this model, the S-wave velocity (V_s) linearly increases from 200 m/s for surface soil to 400 m/s for limestone at the model bottom. The initial P-wave velocity (V_p) was assumed to be twice the initial V_s. The inversion began with the initial model shown in Fig. 4.23, utilizing waveform data filtered within a 10-40 Hz bandwidth. The inversion process concluded after 100 iterations.

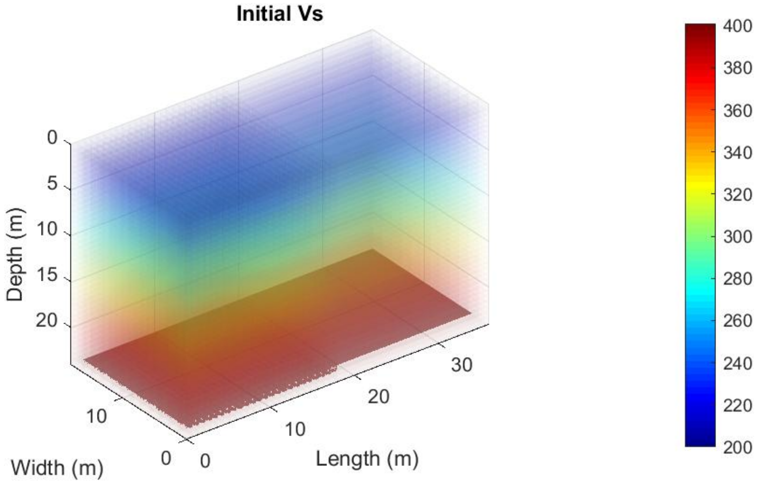

Figure 4.23. Initial V_s used for inversion, and initial V_p as $2 \times V_s$ (not shown)

Figure 4.24 shows the normalized errors, which decreased from 1.0 at the beginning to 0.75 at the end of analysis. Figure 4.25 shows a comparison between the observed and estimated data for two source locations. A good agreement between the final estimated and field data was obtained. No cycle skipping (matching of wrong peak) is seen, suggesting the analysis converges to the global solution.

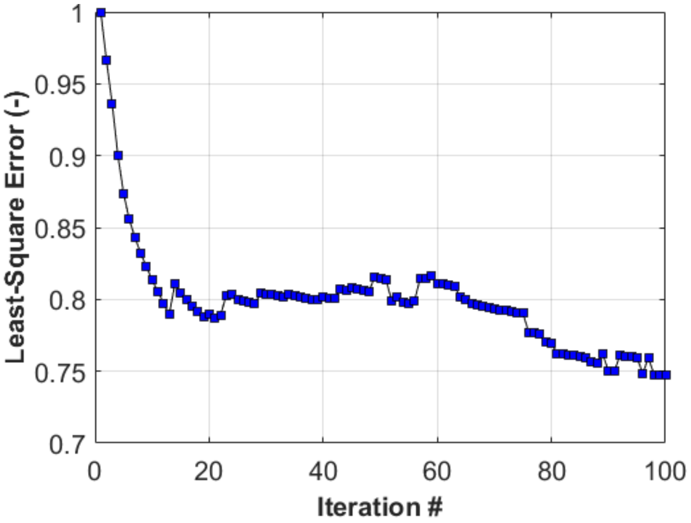

Figure 4.24 Kanapaha site: normalized least-squares errors of all 100 iterations

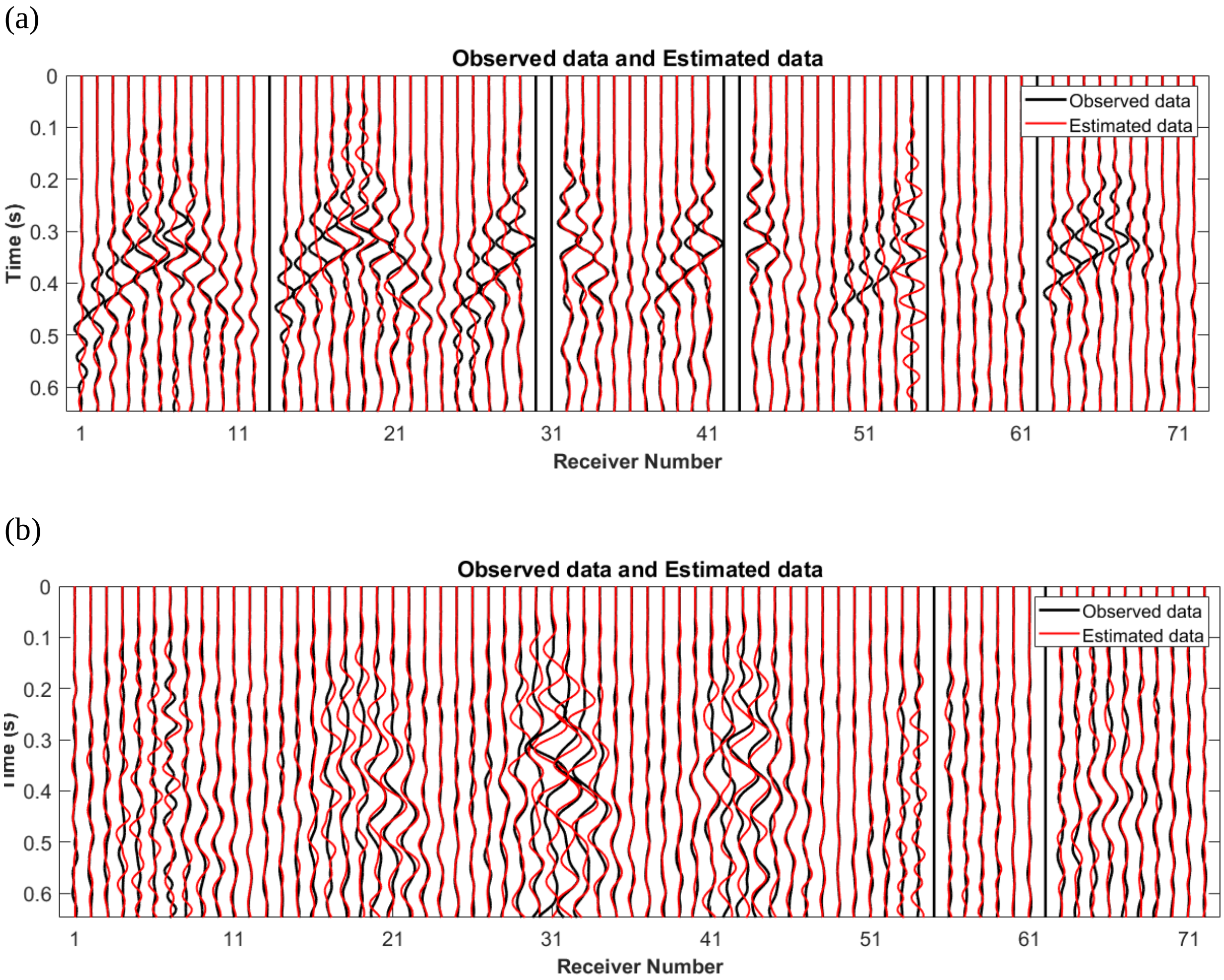

Figure 4.25. Field Experiment — Waveform comparison between observed and estimated data: (a) first source (surface source); (b) deepest source at 17.4 m (58 ft). Poor channels were excluded from the analysis

Figure 4.26 presents the final inverted results. The V_s profile delineates a soil layer (V_s ~200 m/s from surface to about 10-m depth (30 ft), underlain by variable limestone layers with V_s > 500 m/s. Notably, a small void is effectively characterized with low V_s values (~ 100 m/s) at 10-12 m depth, which was confirmed by SPT data (around 11 m depth). The V_p profile mirrors the V_s profile, delineating the void and the soil/limestone layers.

The 3D rendering of the inverted V_s and V_p profiles portrays a shallow soil layer over the limestone layer. The top of the limestone layer exhibits variation, ranging from 10 to 13 m (33-43 ft) below the surface within the test area of 36 × 18 m (120 × 60 ft). The soft layer is clearly visualized as the blue zone in the figure.

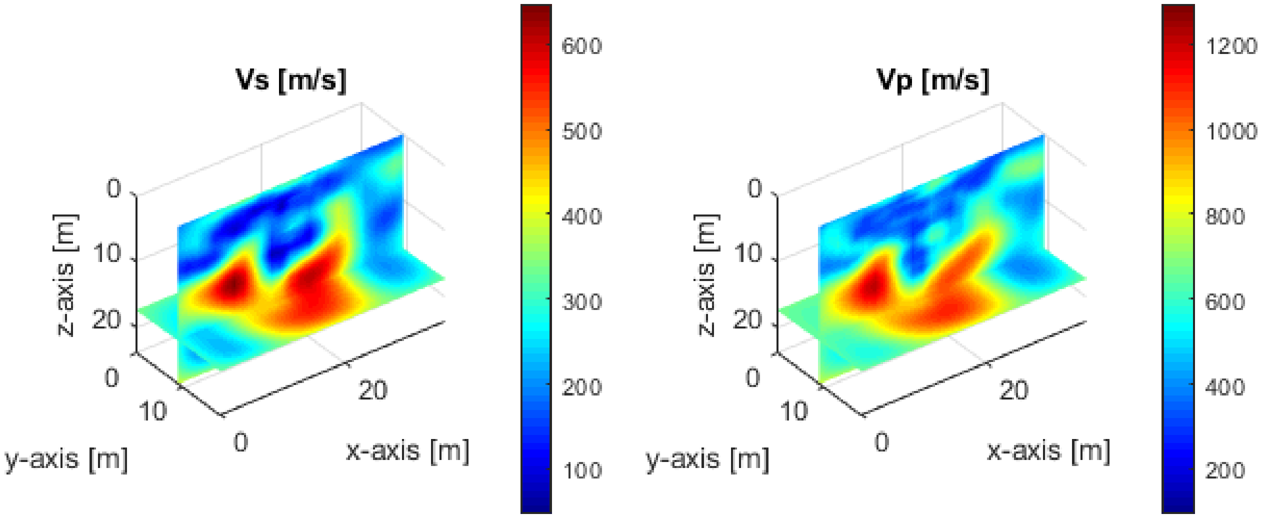

Figure 4.26. Kanapaha site: 2D cross-section view of inverted V_s and V_p

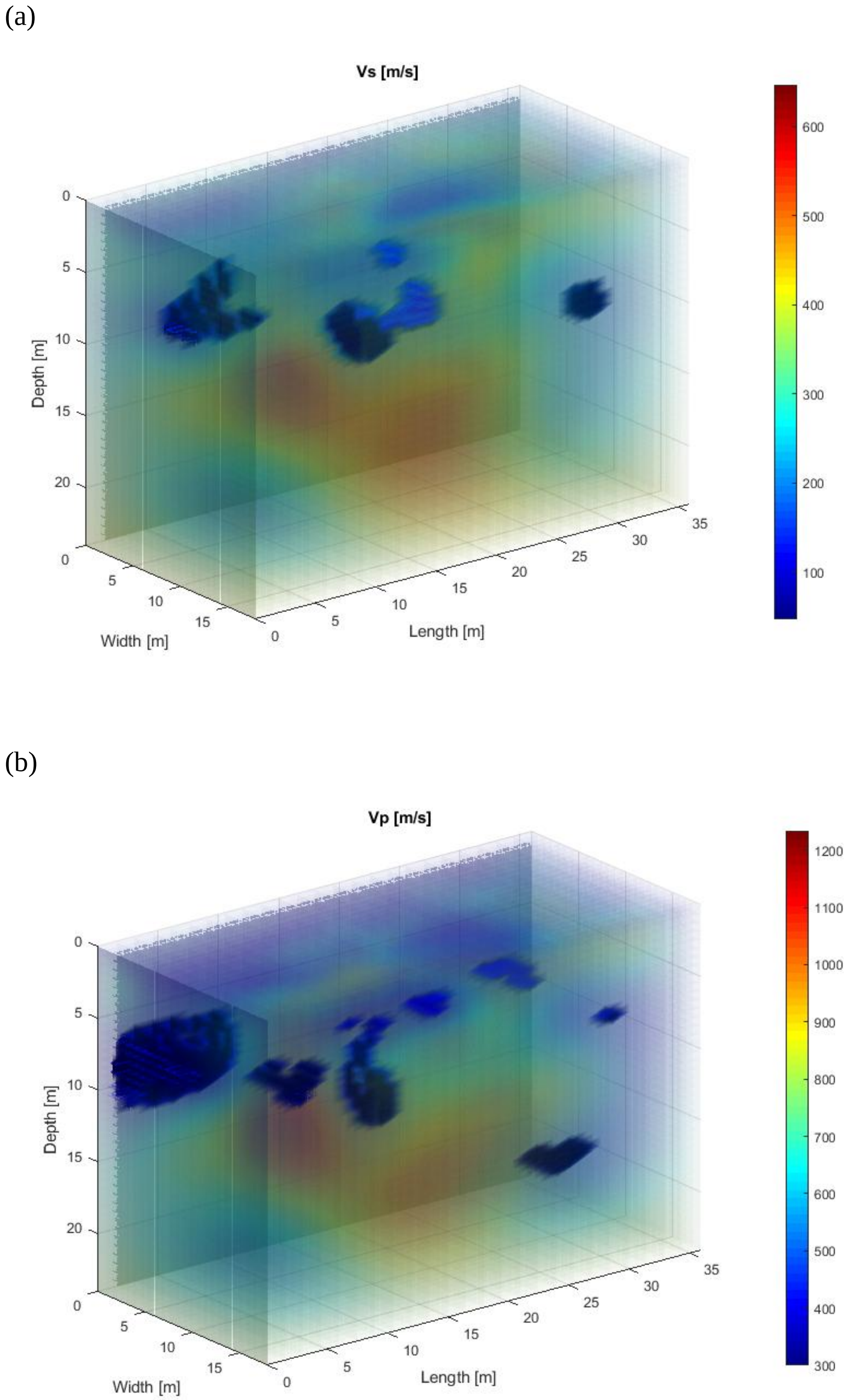

Figure 4.27 Kanapaha site: 3D rendering of inverted V_s (a) and V_p (b). The anomaly is clearly shown as the blue zone near the middle in V_s profile

4.4.3 Verification

Figure 4.28 shows both the initial and final inverted V_s profiles at the SPT location, accompanied by SPT-N (blow counts) values. The final V_s profile well agrees with SPT-N values, including low-velocity zones between 1.5-4 m depth (5-13 ft) and 10-12 m depth (33-40 ft), a medium-velocity zone near the ground surface and 4-10 m depth (13-33 ft), and a high-velocity zone (limestone) below 12-m depth (40 ft). The very low V_s value (~ 100 m/s) indicates a void filled with soil or very soft soil zone, which is confirmed by the weight of hammer recording at 11 m depth (37 ft) from the SPT. The SPT-seismic FWI effectively characterizes subsurface soil/rock stratigraphy and properties and anomalies at this site.

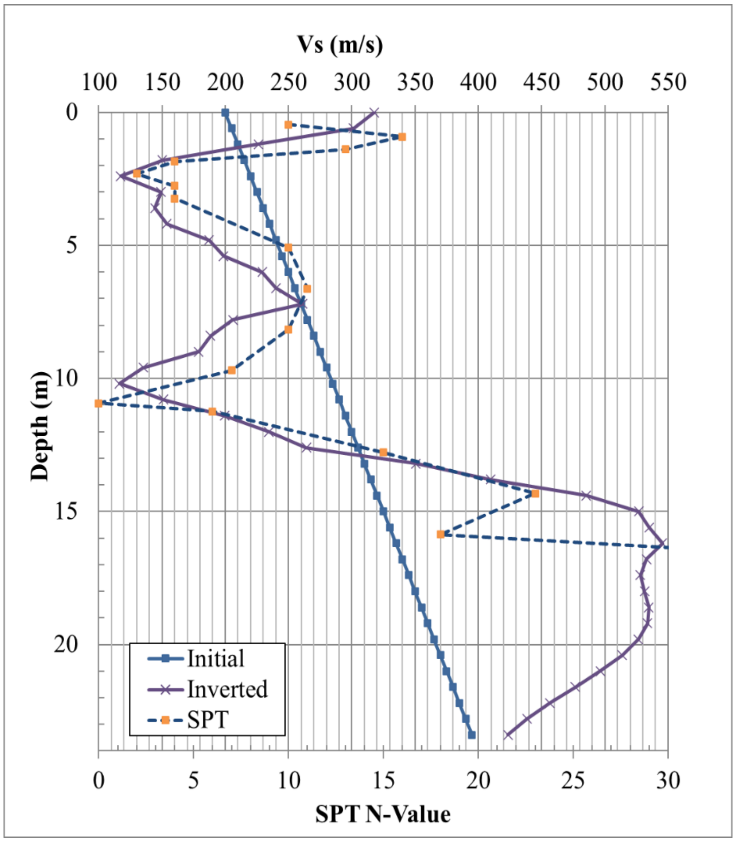

Figure 4.28 Kanapaha site: comparison of V_s with SPT N-values

4.5 Correlation between SPT N-values and V$_s$

To correlate V$_s$ with SPT N_{60} values, it is necessary to interpolate N_{60} to match the V$_s$-measurement depths. This is because SPT data are typically recorded at non-uniform depths, while V$_s$ measurements are taken at uniform depths (e.g., 2 ft cells). Linear interpolation between the nearest SPT points is a straightforward and commonly used approach. For example, SPT-N value at depth z^*, where $z_{\mathrm{low}} \leq z^* \leq z_{\mathrm{high}}$, is determined by a linear interpolation of N_{60} as:

$$N_{60}(z^*) = N_{60,\mathrm{low}} + \left[N_{60,\mathrm{high}} - N_{60,\mathrm{low}}\right] \frac{z^* - z_{\mathrm{low}}}{z_{\mathrm{high}} - z_{\mathrm{low}}}, \tag{4-1}$$

where z^* is the target depth for interpolation (e.g., V$_s$ measurement depth); z_{low} and z_{high} are bounding depths of the SPT data; $N_{60,\mathrm{low}}$ and $N_{60,\mathrm{high}}$ are N_{60} values at z_{low} and z_{high}, respectively. The V$_s$ and interpolated SPT-N data for all 3 sites (Newberry, Bell, and Kanapaha) are shown in Fig. 4.29.

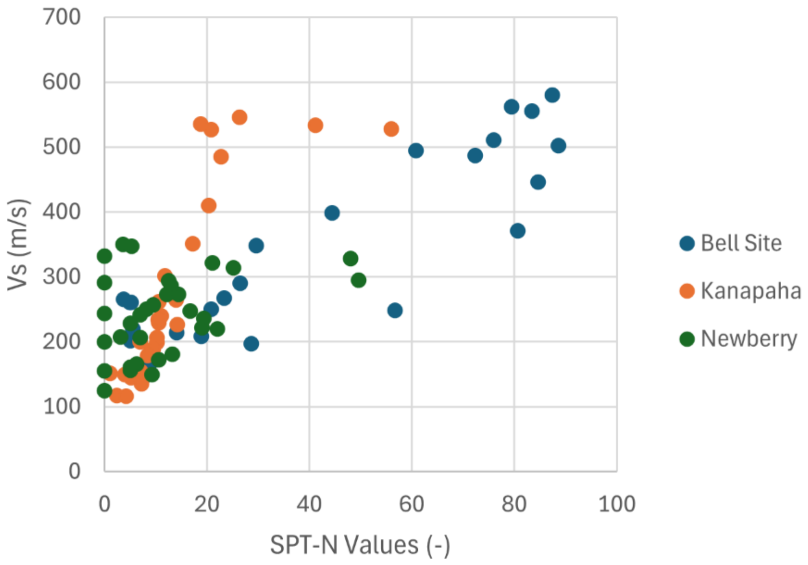

Figure 4.29 SPT-N versus V$_s$ values for all three sites

A popular approach is to assume (Anbazhagan et al., 2012; Rahimi et al., 2020)

$$V_s = a(N_{60})^b. \tag{4-2}$$

Taking the natural logarithm (ln) of both sides transforms the equation into a linear form:

$$\ln(V_s) = \ln(a) + b\ln(N_{60}). \tag{4-3}$$

Let $x = \ln(N_{60})$ and $y = \ln(V_s)$, then the equation becomes:

$$y = \alpha + b\,x, \tag{4-4}$$

where $\alpha = \ln(a)$ and b are determined through linear least-squares fitting.

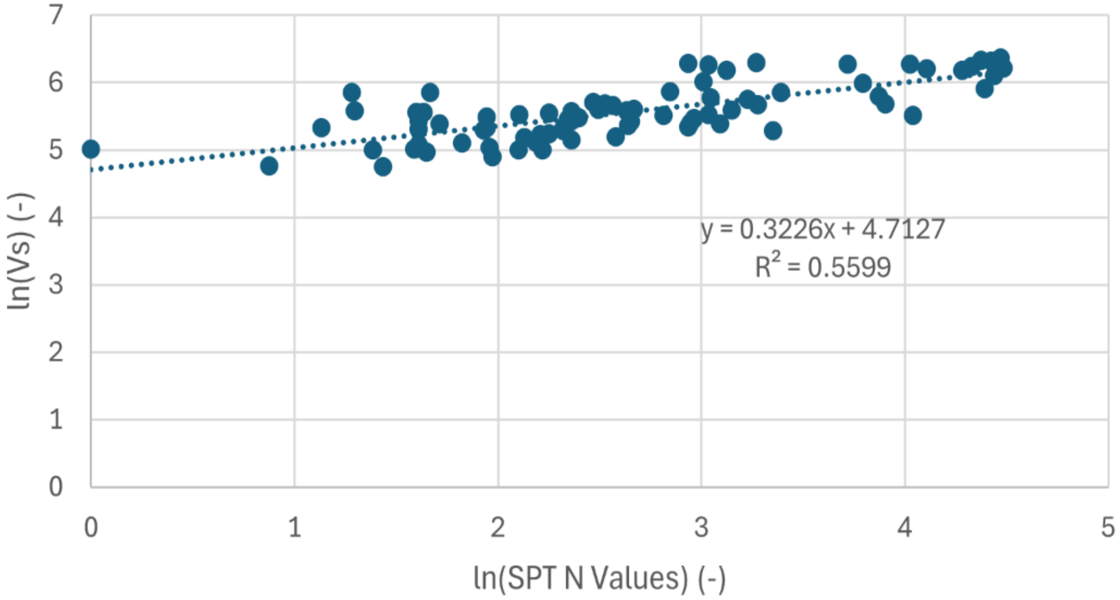

Figure 4.30 Least-squares fitting for finding correlation between SPT-N values and V_s

Based on the least-squares fitting (Fig. 4.30), the linear relation is as:

$$y = 4.7127 + 0.3226\,x \quad \text{with } R^2 = 0.5599. \tag{4-5}$$

From equation 4-5, $\alpha = 4.7127$ and $b = 0.3226$, giving $a = e^{\alpha} = e^{4.7127} = 111.35$. Thus, the power-law relationship is:

$$V_s = 111.35 \times (N_{60})^{0.324}. \tag{4-6}$$

The coefficient of determination R^2 for the model is 0.5599, indicating that approximately 56% of the variation in V_s is explained by the power-law relationship with N_{60}. This correlation provides a practical tool for estimating V_s values from SPT N_{60} or SPT N_{60} from V_s values, aiding in geotechnical analyses and site characterization.

4.6 Conclusion

Field experiments were conducted to verify the capabilities of the SPT-seismic method in imaging voids/anomalies and charactering soil/rock properties and layering. The method relies on 3D FWI of SPT-induced wavefields with in-depth sources and surface receivers. The experiments were performed at 3 sites (Newberry, Bell, and Kanapaha) with two test areas at Newberry site, one area at Bell site, and one area at Kanapaha site. Each test area was 36 × 18 m (120 × 60 ft), with a 2D grid of 72 vertical geophones to record data induced by an SPT at the center of each area. Depths of SPT varied from 51 to 63 ft at sites.

Seismic results suggest that the SPT-seismic method worked effectively at all three test sites. Soil/rock properties and voids can be characterized at sub-meter pixels over a large 3D domain of 24 × 36 × 18 m (80 × 120 × 60 ft in depth × length × width) or (e.g., up to 60 m away from SPT location and 20 ft beyond SPT depth). Multiple voids at various depths from 15 to 55 ft were detected with locations and dimensions consistent with SPT data. The inverted V_s profiles of soil and rock consistently aligned with SPT N-values at all three sites.

Leveraging SPT-induced wavefields predominantly composed of body wave components within rock masses, the method introduces new imaging capabilities for subsurface soil/rock with enhanced accuracy and resolution at varying depths. It enables characterization at sub-meter pixels across a substantial 3D volume. Requiring only a single borehole for 3D imaging, it proved cost-effective and efficient for site characterization, especially for imaging of deep voids within weathered and karst rock.

In addition, the method’s ability in charactering soil/rock around and beyond an SPT borehole is significantly important for design and construction of deep foundations. It allows us to use a single SPT at the center of a pile group to characterize the entire volume of materials supporting all piles in the group (around and below pile tip). It is particularly useful in weathered and karst rock, where both SPT and piles often end near the top of bedrock. For example, piles could socket within the stiff layer above the void due to refusal, leading to insufficient capacity. The ability to image soil/rock beyond the SPT depth can help to reduce the cost of invasive tests, as well as minimize the risk of pile failure/collapse due to unexpected site conditions.

Chapter 5 – IMPLEMENTATION OF 3D SPT- SEISMIC SOFTWARE (TASK 4)

5.1 Introduction

Task 4 entailed the development of a graphical user interface (GUI) software and an accompanying user manual for the 3D SPT-seismic waveform tomography (3D SPT-SWT). The primary focus was on creating software that supports graphical input, analysis, and output, specifically designed for technician-level personnel operating with basic training.

The GUI allows users to input critical parameters such as the dimensions of the analysis domain, locations of receivers (geophones) and sources, as well as field-collected data. Users can perform data conditioning tasks—such as filtering and windowing—and have the capability to exclude poor channels (faulty receivers) or profiles (defective sources) from the dataset prior to inversion analysis.

After data conditioning, the software executes the 3D SPT-seismic FWI algorithm developed in Task 1, producing 3D renderings of subsurface S-wave (V_s) and P-wave (V_p) velocities. These results are displayed within the GUI for user interpretation. Additionally, users can save input geometry and project data—including conditioned data, V_s and V_p values, waveforms, and least-squares error metrics—for future analysis or for transferring analysis files. Saved projects can be reopened in the GUI at any time.

This report includes a comprehensive user manual for operating the software. A summary of the software development process is presented below.

5.2 Summary of software development and validation

The primary objective of developing the GUI software is to enable users to upload data files, analyze the data, and obtain subsurface 3D renderings of S-wave (V_s) and P-wave (V_p) velocities without the need for programming knowledge. To achieve this, the GUI has been developed using MATLAB, the same programming environment utilized for the original code in Tasks 1-3.

To ensure that the GUI functions identically to the original code and to verify its correct implementation without any loss of functionality or introduction of errors, each major computational component of the code has been rigorously validated. The validation process involved running field experimental data from three test sites, Newberry, Bell, and Kanapaha sites, through the GUI and comparing the results with those obtained from the original code in Task 3. In each case, the absolute differences between the GUI results and the original results were calculated, yielding zero or negligible discrepancies. This outcome confirms that the GUI implementation is accurate and that the software is robust across various site conditions.

5.3 Conclusion

A standalone Graphical User Interface (GUI) software for 3D SPT-Seismic Waveform Tomography (3D SPT-SWT) has been successfully developed. Written in MATLAB and compiled into an executable file, the software can be run on computers without the need for MATLAB installation. The required computational time is 4 to 24 hours for a setup involving 24 to 72 geophones, with the total processing time depending on the recording durations and the number of geophones employed. For a small test area of 40 x 60 ft on ground surface with 24 geophones, the software can provide results within 4 hours on a standard computer.

The software encompasses several features that allow users to graphically input geometry, import data, pre-process data, generate an initial model using spectral analysis, and perform inversion to obtain the final outputs of 3D S-wave (V_s) and P-wave (V_p) velocities. For result assessment, the program provides waveform comparisons between observed and estimated data, as well as least-squares error calculations for each iteration. Furthermore, inversion results and input parameters can be saved and reloaded within the program, facilitating future analyses and the transfer of analysis files. A comprehensive user manual for the software is included in the Appendix.

Chapter 6 – SUMMARY

6.1 General

This project advanced the state-of-the-art in geotechnical site characterization by developing and optimizing a novel 3D SPT-seismic method for high-resolution subsurface imaging. Specifically, the method integrates seismic wavefields generated during Standard Penetration Test (SPT) hammer strikes with a 3D FWI framework to capture body wave energy at depth. The framework adopts a hybrid time-frequency domain approach, where forward wave simulations are conducted in the time domain and inversion is performed using selected dominant frequencies, significantly reducing computational memory (RAM) requirements.

The 3D SPT-seismic method was first tested on synthetic datasets created from realistic soil and rock profiles with embedded voids, demonstrating its ability to accurately characterize subsurface anomalies and material properties at depth. It was then applied to field experimental data, successfully imaging voids, weak zones, and variations in soil and rock properties. The results showed that the method could achieve high-resolution 3D images extending 60 ft away from SPT boreholes. The seismic results correlate well with the SPT-N values, confirming the accuracy and reliability of the method.

Additionally, this study explored the practical implementation of the SPT-seismic method, including automation of data collection, optimization of analysis workflows, and validation against field measurements. A standalone GUI software module for the 3D SPT-seismic FWI has been developed and transferred to FDOT for future applications. Further discussions on the individual components and findings of this study are presented in the following sections.

6.2 Development of 3D SPT-seismic FWI algorithm

A novel 3D SPT-seismic FWI algorithm has been developed for advanced geotechnical site characterization. This algorithm integrates seismic waveform data recorded on the surface with FWI techniques to extract detailed 3D material properties, including S-wave (V_s) and P-wave (V_p) velocities, even at significant depths. The method is specifically designed to address challenges in resolving complex subsurface features in geotechnical investigations.

The algorithm was tested on synthetic models simulating typical Florida geology, consisting of soil layers overlying variable limestone with embedded voids. Waveform data were generated using a 2D grid of surface sensors spaced 10 feet apart and in-depth sources placed at 4-foot intervals along a vertical SPT line. These data were analyzed as if collected from actual field experiments. The algorithm successfully characterized material properties (V_s, V_p) in 3D within 60 ft from the SPT line and to depths of 100 ft. It accurately identified void locations, shapes, and layer interfaces, demonstrating its capability to resolve complex subsurface features. These results validate the algorithm's potential for high-resolution subsurface imaging in geotechnical applications.

6.3 Optimization of test configurations for 3D SPT-seismic FWI

Optimization of test configurations (receiver locations and source intervals) has been performed for the 3D SPT-Seismic FWI algorithm. The objective was to determine the minimum number of receivers (maximum spacing) and sources (maximum interval) required for successful characterization of variable layers and embedded voids. Several configurations with receiver spacings from 7.5 ft to 22.5 ft and source intervals of 2 ft and 4 ft were tested on two synthetic models with variable soil or rock layers and embedded voids. The accuracy and resolution of inverted V_s and V_p profiles were compared to identify the optimal configuration.

From the results of the analysis, a receiver spacing of 10 ft and an SPT source interval of 4 ft are recommended for field testing to ensure accurate characterization of both V_s and V_p profiles. If only the V_s profile is required, a receiver spacing of up to 15 ft can be used, although V_p accuracy may be reduced. Reducing the source interval to 2 ft did not improve the results due to data redundancy, confirming that intervals smaller than 4 ft are unnecessary. These optimal configurations are recommended for field experiments. Additionally, for field applications, recording all SPT blows within intervals of 2–4 ft is advised to enhance signal-to-noise ratio and ensure reliable data for accurate subsurface imaging.

6.4 Verification of 3D SPT-seismic method at field test sites

The developed 3D SPT-seismic method has been successfully applied to field experiments for imaging voids and characterizing soil and rock properties. Field tests were conducted at three sites: Newberry (two areas), Bell (one area), and Kanapaha (one area). Each test area measured 36 × 18 m (120 × 60 ft) and utilized a 2D grid of 72 vertical geophones on the surface to record seismic wavefields induced by an SPT at the center, with SPT depths ranging from 51 to 63 ft.

Based on the field experiments and results at the three sites, the 3D SPT-seismic method demonstrated several advantages. First, it accurately characterized soil/rock properties and detected multiple voids at depths of 15–55 ft with sub-meter resolution across a 3D domain of 24 × 36 × 18 m (80 × 120 × 60 ft). Second, the inverted V_s profiles consistently aligned with SPT N-values, confirming the accuracy of the method. Third, the use of SPT-induced wavefields, dominated by body waves, enabled high-resolution imaging at varying depths with minimal additional field equipment.

The method’s ability to characterize materials around and beyond the SPT borehole is particularly beneficial for the design and construction of deep foundations. It allows a single SPT at the center of a pile group to image the entire volume of materials supporting all piles, reducing the need for multiple invasive tests. Additionally, it minimizes risks of pile failure by detecting unexpected conditions, such as voids or insufficiently stiff layers beneath pile tips. The field results confirm that the 3D SPT-seismic method is an effective and cost-efficient tool for geotechnical site investigations, particularly for the design of deep foundations.

6.5 Implementation of 3D SPT-seismic FWI software

A standalone GUI-based software for the 3D SPT-seismic FWI analysis has been developed. The software is written in MATLAB and compiled into an executable file, allowing it to run on computers without requiring MATLAB. The processing time ranges from 4 to 24 hours per dataset, depending on the number of geophones and the depth of SPT testing.

The software includes a user-friendly interface with several features to simplify data input and analysis. Users can graphically input parameters, such as the spacing and number of geophones, and import raw seismic waveform data directly from a hard drive. It also enables users to condition input data through filtering, windowing, and removing bad channels. A quality check feature allows users to review the conditioned data before proceeding with the analysis.

The software outputs detailed subsurface profiles, including S-wave (V_s) and P-wave (V_p) velocities, which are displayed on the GUI and can be exported for reporting purposes. A comprehensive user manual, included in the Appendix, provides step-by-step guidance on using the software, ensuring accessibility for users with minimal training. The manual also includes examples of real seismic waveform datasets to aid in understanding the process and results. This software streamlines the analysis workflow, making the 3D SPT-seismic FWI method practical for geotechnical practitioners.

REFERENCES

Anbazhagan, P., Parihar, A., & Rashmi, H. N. (2012). Review of correlations between SPT N and shear modulus: A new correlation application to any region. *Soil Dynamics and Earthquake Engineering*, 36, 52–69. https://doi.org/doi:10.1016/j-soildyn.2012.01.005

Banton, O., Cimon, M. A., & Seguin, M. K. (1997). Mapping Field-Scale Physical Properties of Soil with Electrical Resistivity. *Soil Science Society of America Journal*, 61(4), 1010–1017. https://doi.org/10.2136/sssaj1997.03615995006100040003x

Butzer, S., Kurzmann, A., & Bohlen, T. (2013). 3D elastic full-waveform inversion of small-scale heterogeneities in transmission geometry. *Geophysical Prospecting,* 61(6), 1238–1251. https://doi.org/10.1111/1365-2478.12065

Farooq, M., Park, S., Song, Y. S., Kim, J. H., Tariq, M., & Abraham, A. A. (2012). Subsurface cavity detection in a karst environment using electrical resistivity (ER): a case study from Yongweol-ri, South Korea. *Earth Sciences Research Journal*, 16(1), 75–82.

Jol, Harry M. (Ed.). (2009). *Ground Penetrating Radar Theory and Applications.* Elsevier Science. Oxford, UK.

Komatitsch, D., & Martin, R. (2007). An unsplit convolutional perfectly matched layer improved at grazing incidence for the seismic wave equation. *Geophysics,* 72(5), SM155-SM167, https://doi.org/10.1190/1.2757586

Mirzanejad, M., & Tran, K. T. (2019). 3D viscoelastic full waveform inversion of seismic waves for geotechnical site investigation. *Soil Dynamics and Earthquake Engineering*, 122, 67–78. https://doi.org/10.1016/j.soildyn.2019.04.005

Mirzanejad, M., Tran, K. T., McVay, M., Horhota, D., & Wasman, S. J. (2020a). Coupling of SPT and 3D full waveform inversion for deep site characterization. *Soil Dynamics and Earthquake Engineering*, 136, 1-12. https://doi.org/10.1016/j.soildyn.2020.106196

Mirzanejad, M., Tran, K. T., McVay, M., Horhota, D., & Wasman, S. J. (2020b). Sinkhole detection with 3D full seismic waveform tomography. *Geophysics*, 85(5), B169–B179. https://doi.org/10.1190/geo2019-0490.1

Mahmoud, M. A. A. N., (2013). Reliability of using standard penetration test (SPT) in predicting properties of silty clay with sand soil. *International journal of civil and structural engineering*, 3(3), 545–556. https://doi.org/10.6088/ijcser.2012030130500

Nolet, G. (Ed.). (1987). *Seismic Tomography with Applications in Global Seismology and Exploration Geophysics.* Springer (Netherlands). https://doi.org/10.1007/978-94-009-3899-1

Pratt, R. G., & Shipp, R. M. (1999). Seismic waveform inversion in the frequency domain, Part 2: Fault delineation in sediments using crosshole data. *Geophysics*, *64*(3), 902–914. https://doi.org/10.1190/1.1444598

Rahimi, S., Wood, C. M., & Wotherspoon, L. M. (2020). Influence of soil aging on SPT-V_s correlation and seismic site classification. *Engineering Geology*, 272, 1-12. https://doi.org/10.1016/j.enggeo.2020.105653

Rawlinson, N., Pozgay, S., & Fishwick, S. (2010). Seismic tomography: A window into deep Earth. *Physics of the Earth and Planetary Interiors*, 178(3–4), 101–135. https://doi.org/10.1016/j.pepi.2009.10.002

Robertson, P. K. (2016). Cone penetration test (CPT)-based soil behaviour type (SBT) classification system — An update. *Canadian Geotechnical Journal*, 53(12), 1910–1927. https://doi.org/10.1139/cgj-2016-0044

Salgado, R. (2022). The Engineering of Foundations, Slopes and Retaining Structures; Second Edition (second). CRC Press, FL, USA. https://doi.org/10.1201/b22079

Tran, K. T., McVay, M., Faraone, M., & Horhota, D. (2013). Sinkhole detection using 2D full seismic waveform tomography. *Geophysics*, 78(5), R175 - R183. https://doi.org/10.1190/GEO2013-0063.1

Tran, K. T., Mirzanejad, M., Horhota, D., & Wasman, S. J. (2024). 3D Full-Waveform Tomography of Standard Penetration Test-Seismic Wavefields in Karst Florida Limestone. *Transportation Research Record*, 2678(10), 248–256. https://doi.org/10.1177/03611981241233295

Tran, K. T., Mirzanejad, M., McVay, M., & Horhota, D. (2019). 3-D time-domain Gauss-Newton full waveform inversion for near-surface site characterization. *Geophysical Journal International*, 217(1), 206–218. https://doi.org/10.1093/gji/ggz020

Tran, K. T., & Sperry, J. (2018). Application of 2D full-waveform tomography on land-streamer data for assessment of roadway subsidence. *Geophysics*, 83(3), EN1–EN11. https://doi.org/10.1190/GEO2016-0550.1

Lai, W. -L., Dérobert, X., & Annan, P. (2018). A review of Ground Penetrating Radar application in civil engineering: A 30-year journey from Locating and Testing to

Imaging and Diagnosis. *NDT and E International*, 96, 58–78. https://doi.org/10.1016/j.ndteint.2017.04.002

Wang, Y., & Rao, Y. (2006). Crosshole seismic waveform tomography - I. Strategy for real data application. *Geophysical Journal International*, 166(3), 1224–1236. https://doi.org/10.1111/j.1365-246x.2006.03030.x

Wazoh, H. N. and Mallo. S. J. (2014). Standard Penetration Test in Engineering Geological Site Investigations-A Review. *The International Journal of Engineering and Science*, 3(7), 40–48.

Zhou, B., & Greenhalgh, S. A. (2003). Crosshole seismic inversion with normalized full-waveform amplitude data. *Geophysics*, 68(4), 1320–1330. https://doi.org/10.1190/1.1598125

Appendix: Software Manual

1. Introduction

Welcome to 3D SPT-Seismic Waveform Tomography (3D SPT-SWT) software program, designed for analyzing SPT-seismic data to extract detailed 3D subsurface P/S-wave velocity profiles. This versatile tool provides new capabilities for comprehensive site characterization of soil/rock and buried anomalies. The software boasts a range of features, including:

- Modifiable parameters.
- Easy data import.
- Convenient pre-processing of measured data.
- Inversion capabilities
- Save and export results.

The program's workflow includes six main components: geometry, import data, preprocessing, dispersion analysis, initial wave velocity models, and inverted results. Importantly, each component depends on the preceding one; for instance, parameters must be imported before generating or importing data. If you have any questions or need assistance with specific aspects of the program, email khiem.tran@essie.ufl.edu.

2. Start Page

Figure 1 shows the first page when you run the software. The main menu includes File, Settings, and View.

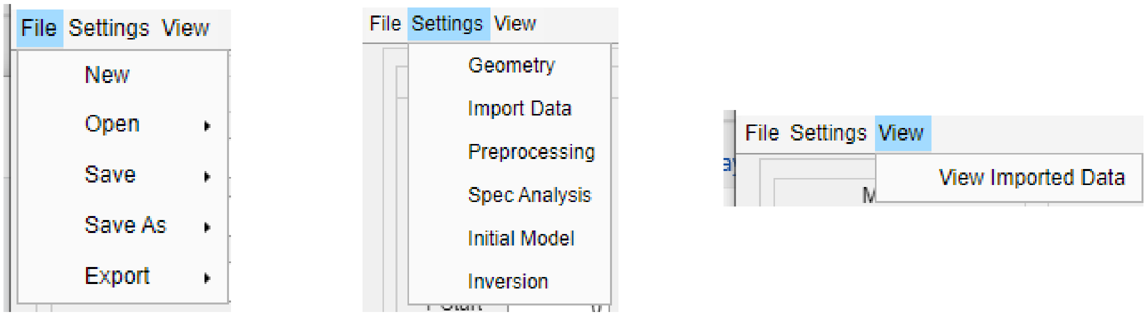

Figure 1. Start Page

There are six required steps for the 3D SWT analysis including:

1. Geometry
2. Input Data
3. Data Pre-processing
4. Spectral Analysis
5. Initial Model
6. Inversion

3. Input Parameters

3.1 New Project

To start a project, choose either:

1. **Settings > Geometry**
2. **Click File > New.**

This action will open the “Geometry” page as seen in Figure 2. On this page, there are required parameters as defined in Table 1.

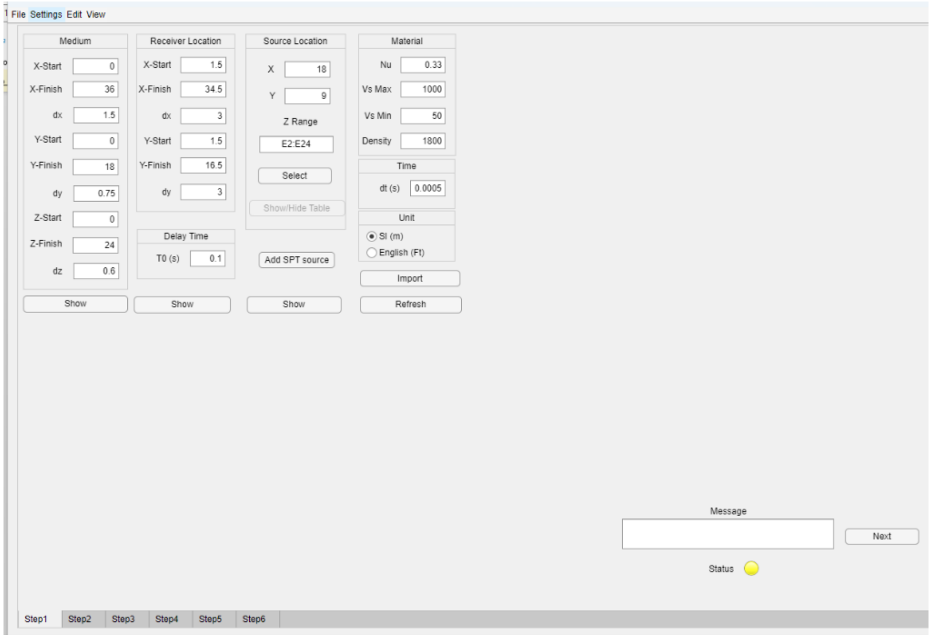

Medium
X-Start 0
X-Finish 36
dx 1.5
Y-Start 0
Y-Finish 18
dy 0.75
Z-Start 0
Z-Finish 24
dz 0.6

Receiver Location
X-Start 1.5
X-Finish 34.5
dx 3
Y-Start 1.5
Y-Finish 16.5
dy 3

Delay Time
T0 (s) 0.1

Source Location
X 18
Y 9
Z Range E2:E24

Material
Nu 0.33
Vs Max 1000
Vs Min 50
Density 1800

Time
dt (s) 0.0005

Unit
● SI (m)
○ English (Ft)

Message

Status ●

Figure 2. Geometry Page

Enter values in editable boxes for the corresponding parameters. As an example, see Figure 3.

Table 1. Geometry settings

Medium		
X/Y/Z-Start	-	Starting location of grid array [m, ft]
X/Y/Z-Finish	-	Ending location of grid array [m, ft]
dx/dy/dz	-	Spacing of grid points in x/y/z direction [m, ft]
Receiver Properties		
X/Y/Z -Start	-	Physical start location of receivers [m, ft]
X/Y/Z -Finish	-	Physical end location of receivers [m, ft]
dx/dy/dz	-	Spacing between receivers [m, ft]
Source location		
X	-	Physical x coordinate location of shots [m, ft]
Y	-	Physical y coordinate location of shots [m, ft]
Z Range	-	Excel cell range to import source depths
Select	-	Import source depth location (Excel files only)
Add SPT Source	-	Add a new SPT Source file
Material properties		
Nu	-	Poisson ratio of material
V_s Max	-	Maximum shear wave velocity of material [m/s]
V_s Min	-	Minimum shear wave velocity of material [m/s]
Density	-	Density of the medium [kg/m^3, lb/ft^3]
Time Properties		
t0	-	Delay Time [s]
dt	-	Sampling rate (time interval) [s]
Unit		
SI	-	m
English	-	ft

After entering required parameters, click **“Import”** button as shown in Figure 4. If parameters are properly imported, there will be a sketch of the analyzed domain displayed in the “Step 1” tab with a message “Parameters parsed successfully”. Otherwise, fix any errors in the parameters.

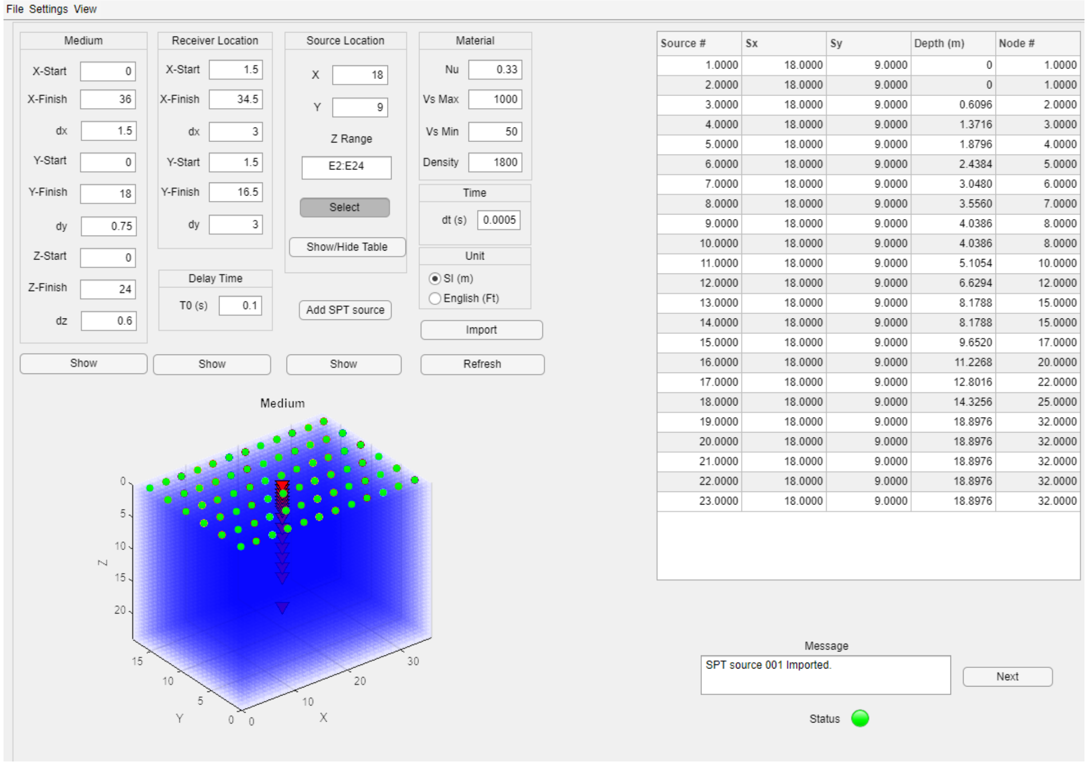

Medium
X-Start 0
X-Finish 36
dx 1.5
Y-Start 0
Y-Finish 18
dy 0.75
Z-Start 0
Z-Finish 24
dz 0.6

Receiver Location
X-Start 1.5
X-Finish 34.5
dx 3
Y-Start 1.5
Y-Finish 16.5
dy 3

Delay Time
T0 (s) 0.1

Source Location
X 18
Y 9
Z Range
E2:E24

Material
Nu 0.33
Vs Max 1000
Vs Min 50
Density 1800

Time
dt (s) 0.0005

Unit
● SI (m)
○ English (Ft)

Source #	Sx	Sy	Depth (m)	Node #
1.0000	18.0000	9.0000	0	1.0000
2.0000	18.0000	9.0000	0	1.0000
3.0000	18.0000	9.0000	0.6096	2.0000
4.0000	18.0000	9.0000	1.3716	3.0000
5.0000	18.0000	9.0000	1.8796	4.0000
6.0000	18.0000	9.0000	2.4384	5.0000
7.0000	18.0000	9.0000	3.0480	6.0000
8.0000	18.0000	9.0000	3.5560	7.0000
9.0000	18.0000	9.0000	4.0386	8.0000
10.0000	18.0000	9.0000	4.0386	8.0000
11.0000	18.0000	9.0000	5.1054	10.0000
12.0000	18.0000	9.0000	6.6294	12.0000
13.0000	18.0000	9.0000	8.1788	15.0000
14.0000	18.0000	9.0000	8.1788	15.0000
15.0000	18.0000	9.0000	9.6520	17.0000
16.0000	18.0000	9.0000	11.2268	20.0000
17.0000	18.0000	9.0000	12.8016	22.0000
18.0000	18.0000	9.0000	14.3256	25.0000
19.0000	18.0000	9.0000	18.8976	32.0000
20.0000	18.0000	9.0000	18.8976	32.0000
21.0000	18.0000	9.0000	18.8976	32.0000
22.0000	18.0000	9.0000	18.8976	32.0000
23.0000	18.0000	9.0000	18.8976	32.0000

Message
SPT source 001 Imported.

Status ●

Figure 3. Geometry Parameters

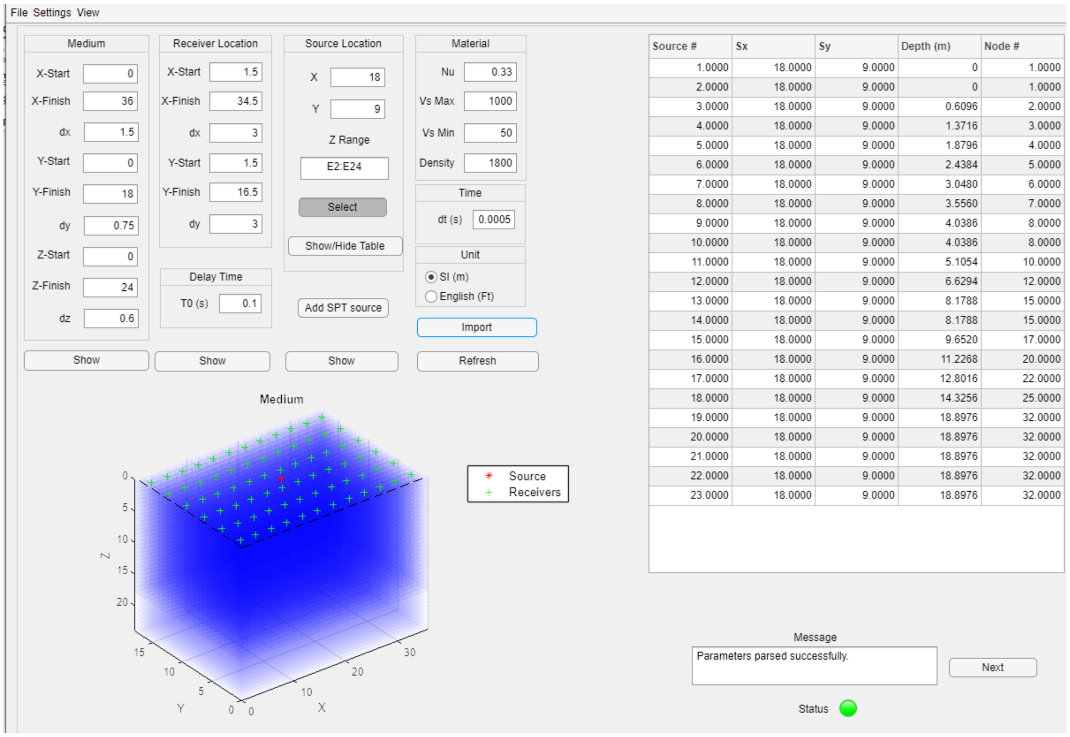

Medium
X-Start 0
X-Finish 36
dx 1.5
Y-Start 0
Y-Finish 18
dy 0.75
Z-Start 0
Z-Finish 24
dz 0.6

Receiver Location
X-Start 1.5
X-Finish 34.5
dx 3
Y-Start 1.5
Y-Finish 16.5
dy 3

Delay Time
T0 (s) 0.1

Source Location
X 18
Y 9
Z Range
E2:E24

Material
Nu 0.33
Vs Max 1000
Vs Min 50
Density 1800

Time
dt (s) 0.0005

Unit
● SI (m)
○ English (Ft)

Source #	Sx	Sy	Depth (m)	Node #
1.0000	18.0000	9.0000	0	1.0000
2.0000	18.0000	9.0000	0	1.0000
3.0000	18.0000	9.0000	0.6096	2.0000
4.0000	18.0000	9.0000	1.3716	3.0000
5.0000	18.0000	9.0000	1.8796	4.0000
6.0000	18.0000	9.0000	2.4384	5.0000
7.0000	18.0000	9.0000	3.0480	6.0000
8.0000	18.0000	9.0000	3.5560	7.0000
9.0000	18.0000	9.0000	4.0386	8.0000
10.0000	18.0000	9.0000	4.0386	8.0000
11.0000	18.0000	9.0000	5.1054	10.0000
12.0000	18.0000	9.0000	6.6294	12.0000
13.0000	18.0000	9.0000	8.1788	15.0000
14.0000	18.0000	9.0000	8.1788	15.0000
15.0000	18.0000	9.0000	9.6520	17.0000
16.0000	18.0000	9.0000	11.2268	20.0000
17.0000	18.0000	9.0000	12.8016	22.0000
18.0000	18.0000	9.0000	14.3256	25.0000
19.0000	18.0000	9.0000	18.8976	32.0000
20.0000	18.0000	9.0000	18.8976	32.0000
21.0000	18.0000	9.0000	18.8976	32.0000
22.0000	18.0000	9.0000	18.8976	32.0000
23.0000	18.0000	9.0000	18.8976	32.0000

Message
Parameters parsed successfully.

Status ●

Figure 4. Import Geometry Parameters

3.2 Open: Geometry or Project

The second way to import geometry is by opening an existing parameter file. To do this, navigate to **File** > **Open** > **Geometry.** If you prefer to open a project containing processed data and inversion results, select **File** > **Open** > **Project.**

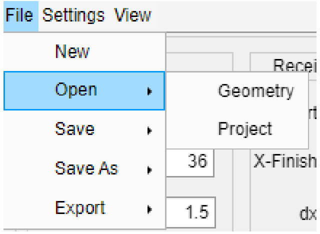

Figure 5. Open Parameters

Depending on your choice, the corresponding screen for opening geometry (Figure 6) or a project (Figure 7) will appear, as shown below.

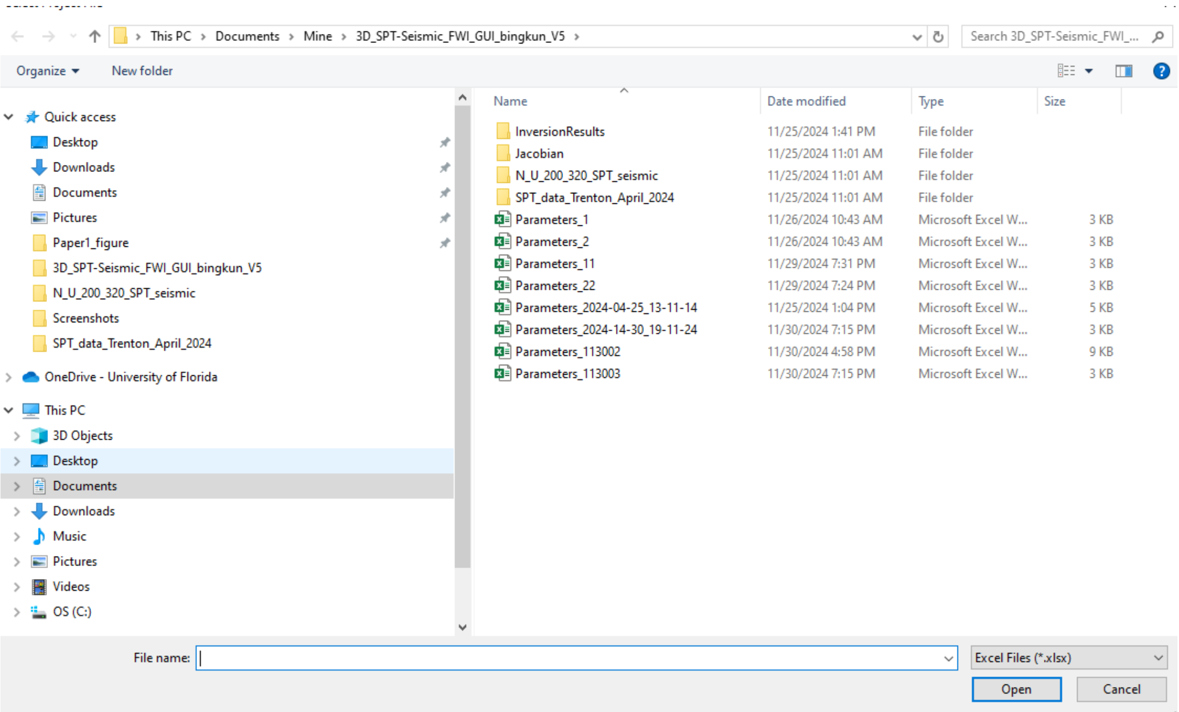

Name	Date modified	Type	Size
InversionResults	11/25/2024 1:41 PM	File folder	
Jacobian	11/25/2024 11:01 AM	File folder	
N_U_200_320_SPT_seismic	11/25/2024 11:01 AM	File folder	
SPT_data_Trenton_April_2024	11/25/2024 11:01 AM	File folder	
Parameters_1	11/26/2024 10:43 AM	Microsoft Excel W...	3 KB
Parameters_2	11/26/2024 10:43 AM	Microsoft Excel W...	3 KB
Parameters_11	11/29/2024 7:31 PM	Microsoft Excel W...	3 KB
Parameters_22	11/29/2024 7:24 PM	Microsoft Excel W...	3 KB
Parameters_2024-04-25_13-11-14	11/25/2024 1:04 PM	Microsoft Excel W...	5 KB
Parameters_2024-14-30_19-11-24	11/30/2024 7:15 PM	Microsoft Excel W...	3 KB
Parameters_113002	11/30/2024 4:58 PM	Microsoft Excel W...	9 KB
Parameters_113003	11/30/2024 7:15 PM	Microsoft Excel W...	3 KB

File name:
Excel Files (*.xlsx)

Figure 6. Open Geometry file(*.xlsx)

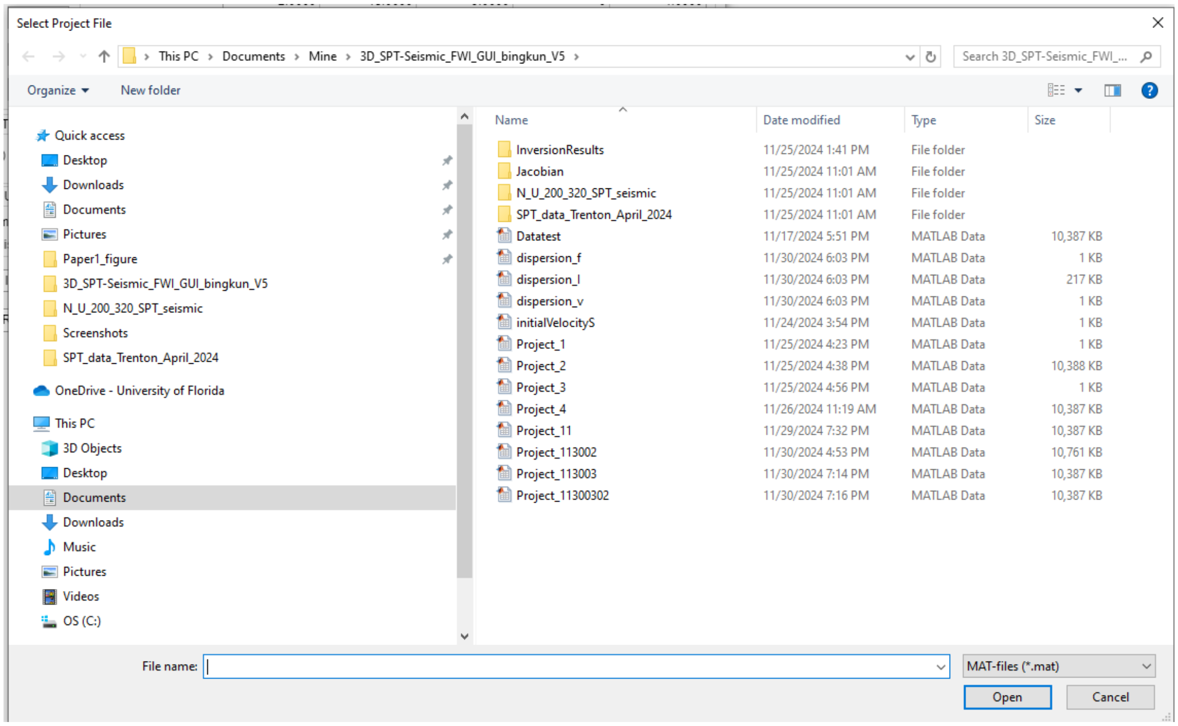

This PC > Documents > Mine > 3D_SPT-Seismic_FWI_GUI_bingkun_V5 >

Search 3D_SPT-Seismic_FWI_...

Name	Date modified	Type	Size
InversionResults	11/25/2024 1:41 PM	File folder	
Jacobian	11/25/2024 11:01 AM	File folder	
N_U_200_320_SPT_seismic	11/25/2024 11:01 AM	File folder	
SPT_data_Trenton_April_2024	11/25/2024 11:01 AM	File folder	
Datatest	11/17/2024 5:51 PM	MATLAB Data	10,387 KB
dispersion_f	11/30/2024 6:03 PM	MATLAB Data	1 KB
dispersion_I	11/30/2024 6:03 PM	MATLAB Data	217 KB
dispersion_v	11/30/2024 6:03 PM	MATLAB Data	1 KB
initialVelocityS	11/24/2024 3:54 PM	MATLAB Data	1 KB
Project_1	11/25/2024 4:23 PM	MATLAB Data	1 KB
Project_2	11/25/2024 4:38 PM	MATLAB Data	10,388 KB
Project_3	11/25/2024 4:56 PM	MATLAB Data	1 KB
Project_4	11/26/2024 11:19 AM	MATLAB Data	10,387 KB
Project_11	11/29/2024 7:32 PM	MATLAB Data	10,387 KB
Project_113002	11/30/2024 4:53 PM	MATLAB Data	10,761 KB
Project_113003	11/30/2024 7:14 PM	MATLAB Data	10,387 KB
Project_11300302	11/30/2024 7:16 PM	MATLAB Data	10,387 KB

File name:

MAT-files (*.mat)

Figure 7. Open Project file (*.mat)

Navigate to the parameter file to open it. This will bring the program back to the same page. The status bar in the bottom right of the screen will say "Parameters Opened" if the parameter file was successfully imported. If needed, modify existing values and reimport them by clicking the **"Import"** button.

4. Data

To ensure accurate results, field data must be carefully imported and, if necessary, pre-processed (Section 5). The program provides a suite of functions to manage this process, including importing, generating, viewing, modifying, and saving the project.

4.1 Open Data

To import data to enter the "Step 2" tab (Figure 8), choose either:

1. **Settings > Input Data**
2. **Click the "Next" button in the "Step 1" tab.**
3. **Click the "Step 2" button in the "Step 1" tab.**

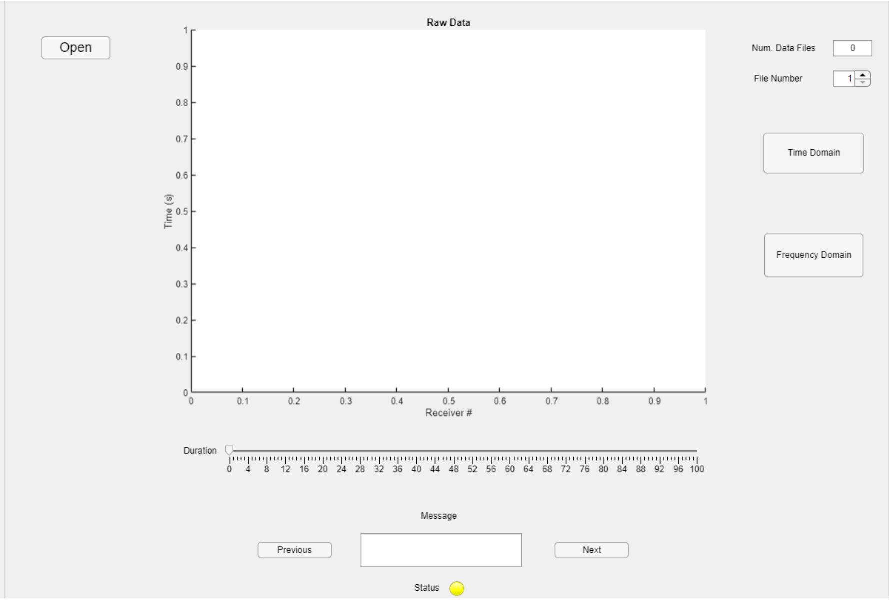

Num. Data Files 0

File Number 1

Figure 8. Input Data

To initiate the process, click the 'Open' button located in the upper left corner. This action prompts 'Select File to Open' window (Fig. 9). Select multiple files by clicking the desired files. Please note that the number of data files corresponds to the sources added in Step 1 during the Excel data import and the files must be named in the numerical order according to their location.

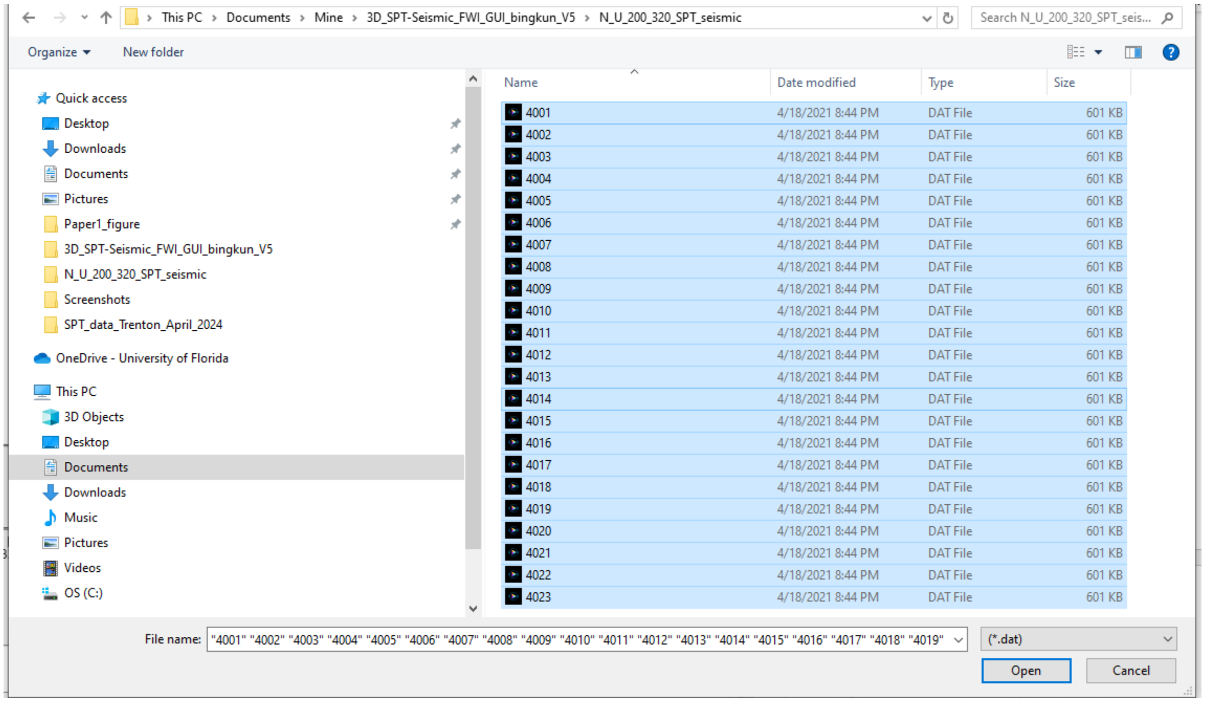

Name	Date modified	Type	Size
4001	4/18/2021 8:44 PM	DAT File	601 KB
4002	4/18/2021 8:44 PM	DAT File	601 KB
4003	4/18/2021 8:44 PM	DAT File	601 KB
4004	4/18/2021 8:44 PM	DAT File	601 KB
4005	4/18/2021 8:44 PM	DAT File	601 KB
4006	4/18/2021 8:44 PM	DAT File	601 KB
4007	4/18/2021 8:44 PM	DAT File	601 KB
4008	4/18/2021 8:44 PM	DAT File	601 KB
4009	4/18/2021 8:44 PM	DAT File	601 KB
4010	4/18/2021 8:44 PM	DAT File	601 KB
4011	4/18/2021 8:44 PM	DAT File	601 KB
4012	4/18/2021 8:44 PM	DAT File	601 KB
4013	4/18/2021 8:44 PM	DAT File	601 KB
4014	4/18/2021 8:44 PM	DAT File	601 KB
4015	4/18/2021 8:44 PM	DAT File	601 KB
4016	4/18/2021 8:44 PM	DAT File	601 KB
4017	4/18/2021 8:44 PM	DAT File	601 KB
4018	4/18/2021 8:44 PM	DAT File	601 KB
4019	4/18/2021 8:44 PM	DAT File	601 KB
4020	4/18/2021 8:44 PM	DAT File	601 KB
4021	4/18/2021 8:44 PM	DAT File	601 KB
4022	4/18/2021 8:44 PM	DAT File	601 KB
4023	4/18/2021 8:44 PM	DAT File	601 KB

File name: "4001" "4002" "4003" "4004" "4005" "4006" "4007" "4008" "4009" "4010" "4011" "4012" "4013" "4014" "4015" "4016" "4017" "4018" "4019"

(*.dat)

Figure 9. Open data files

Then click "Open" to load the selected data files. The software will display the loaded data as shown in Figure 10. When the data is successfully imported, a green status indicator will confirm this. You can use a slider to specify the duration time. With the green status, you're now ready to move on to the next phase of your analysis or configuration.

After importing the data, click "Time Domain" or "Frequency Domain" to view the data in the respective domain if needed. Use the "File Number" spinner to navigate through each shot's data.

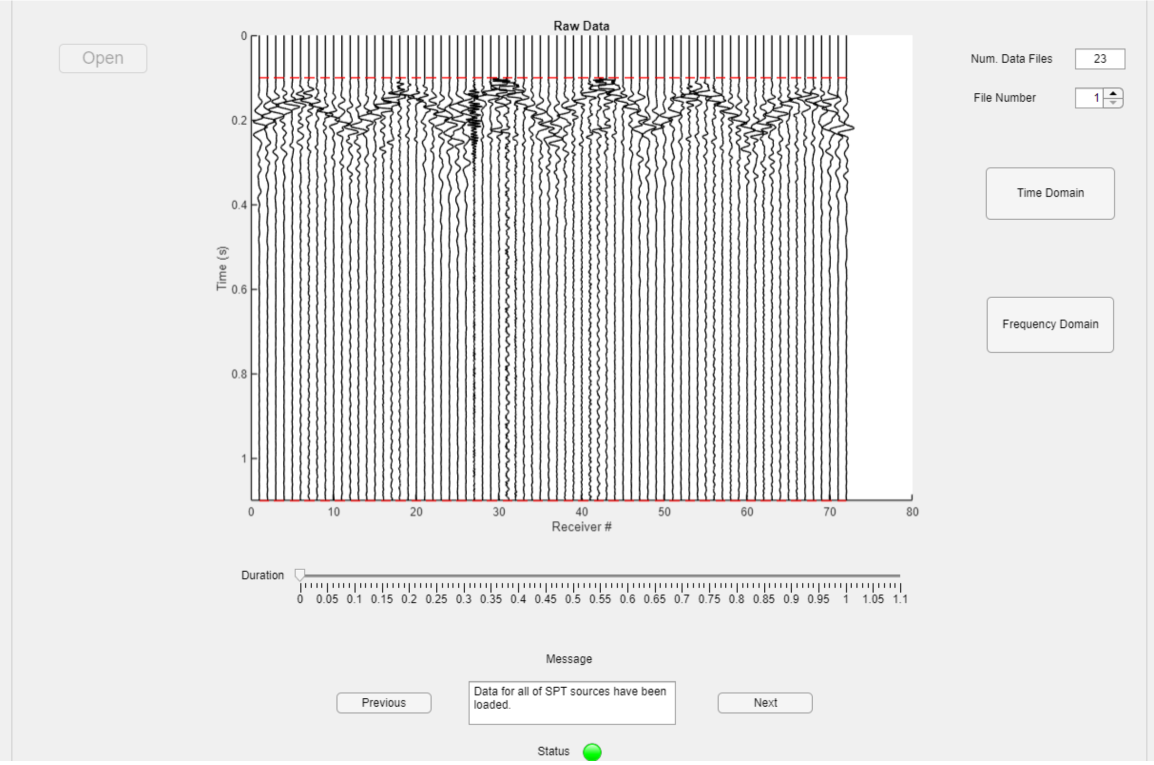

Num. Data Files 23

File Number 1

Message

Data for all of SPT sources have been loaded.

Figure 10. View data

4.2 Viewing Imported Data

To view the data that has been imported/opened into the program, select **View > View Imported Data**. This will produce a window to view the data (Figure 10), which can be seen in time and frequency domains.

5. Data Pre-processing

Step 3 of the 3D SWT analysis is to pre-process the imported data. This needs to be done carefully. Choose either of the below options to open the window as seen in Figure 11.

1. **Settings > Preprocessing.**
2. **Click the “Next” button in the “Step 2” tab.**
3. **Click the “Step 3” button in the “Step 2” tab.**

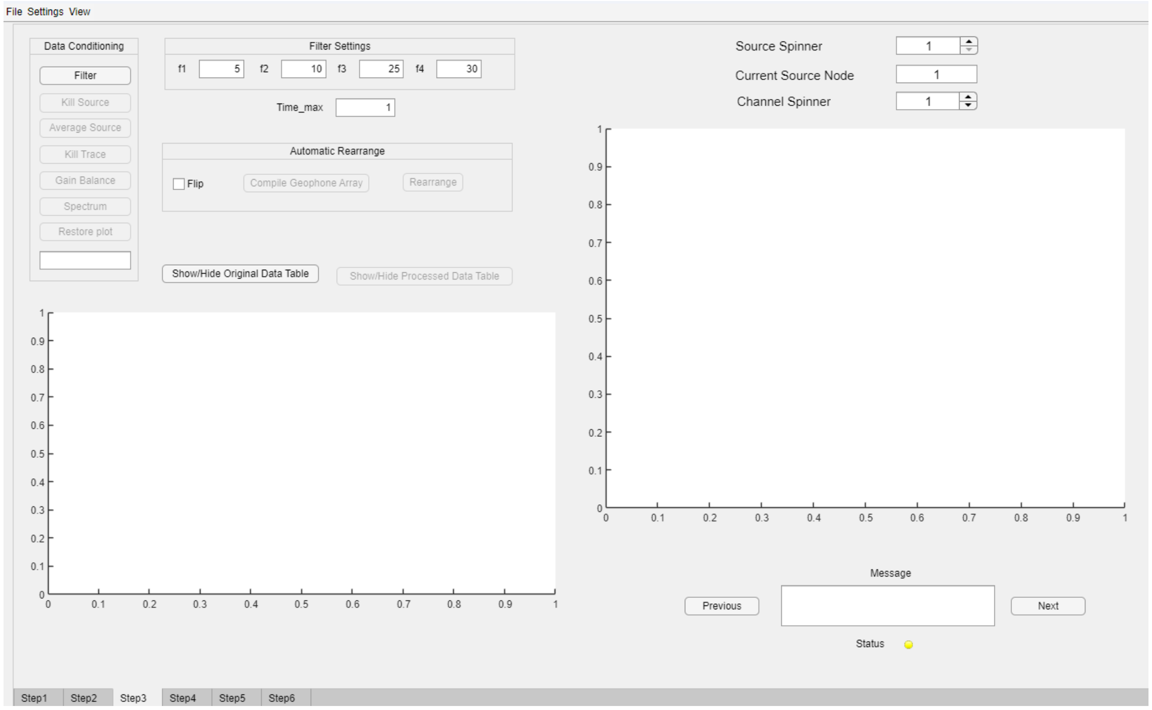
f1 5 f2 10 f3 25 f4 30

Time_max 1

Source Spinner 1

Current Source Node 1

Channel Spinner 1

Figure 11. Data Pre-processing page

The following values are required:

- Set the maximum time (**Time_max**) duration (in seconds) for the input data, making sure it aligns with your collected data's time range.
- Filtering frequencies: **f1, f2, f3, and f4** (Hz) as shown in Figure 12. Configure the filtering frequencies as in Figure 11, adjusting these four values to suit your data processing and inversion requirements.

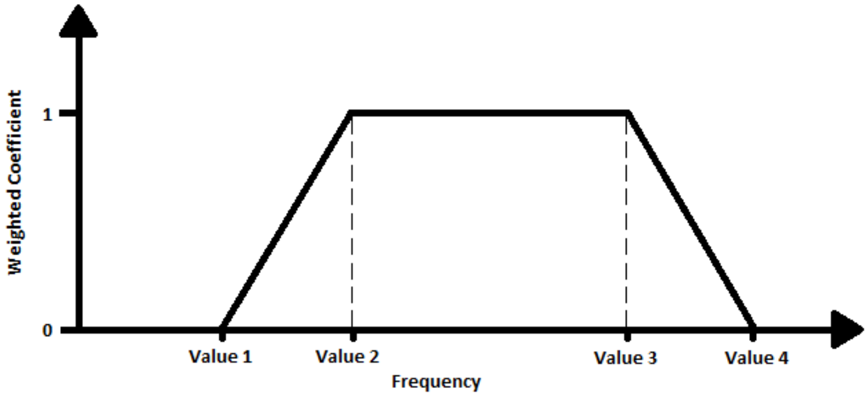

Figure 12. Filtering bandwidth

Take the following steps:

1. Enter values for all the inputs: **Time_max and filters (f1, f2, f3, and f4).**

2. Select “**Filter**” to filter the data (Figure 15).

3. As seismic cables are often looped in field experiments, it is required to rearrange channel locations. For instance, for a data set with 72 channels. The correct geophone array is always as below:

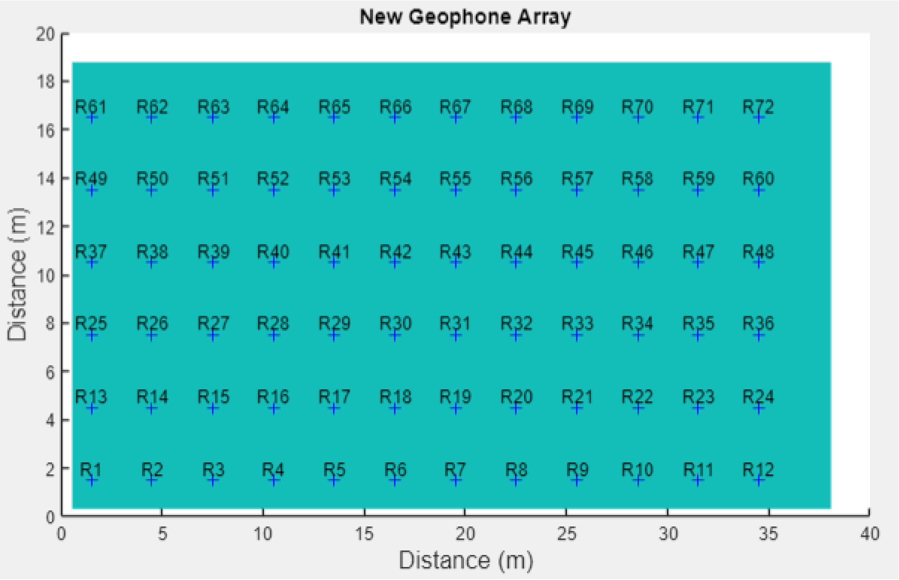

Figure 13. Correct geophone order

However, due to cable looping, the arrangement of geophones in the field can be as Figure 14. Click “**Compile Geophone Array**” to enter the field geophone array into the edit box (specify the first and last geophone on each line, see Figure 14), then click "**Rearrange"** to automatically reorder channels correctly (as shown in Figure 13).

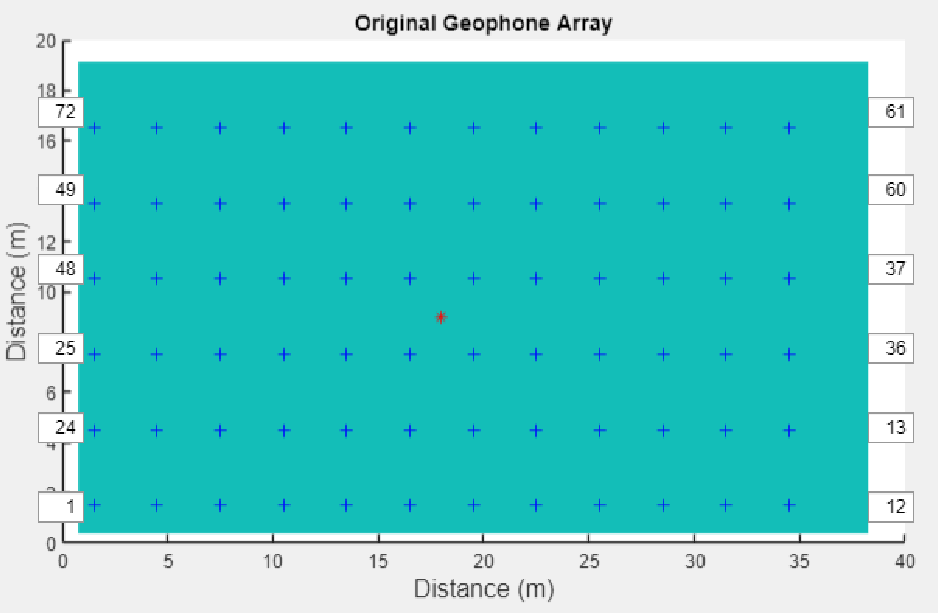

Figure 14. Geophone array in the field

4. Select **"Kill Source**" to kill poor profiles (Figure 16). Click "Kill Source" **again** to "**Unkill Source".**

5. Select "**Average Source**" to average profiles in the same source depth (Figure 17).

6. Select "**Kill Trace**" to kill the poor channels (Figure 18). Click "Kill Trace" **again** to "**Unkill**" the trace.

7. Click on "**Gain Balance**" button to show a gain balance profile (Figure 19).

8. Click on "**Spectrum**" button to check the frequency spectrum (Figure 20).

9. Select "**Restore plot**" to show the raw data before pre-processing.

10. Show original data table, which will give you the shot #, source depth, and source node # of original datasets.

11. Show processed data table, which will give you the shot #, source depth, source node # and average number of source for each node of processed datasets.

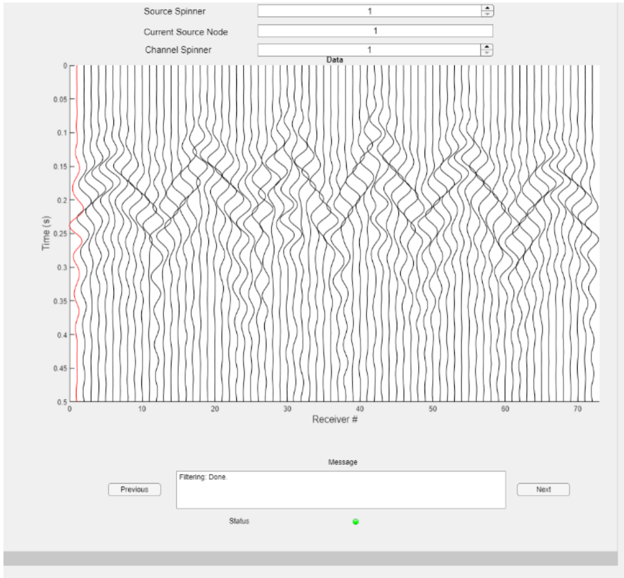

Source Spinner 1
Current Source Node 1
Channel Spinner 1

Message: Filtering: Done.

Figure 15. Filtering data

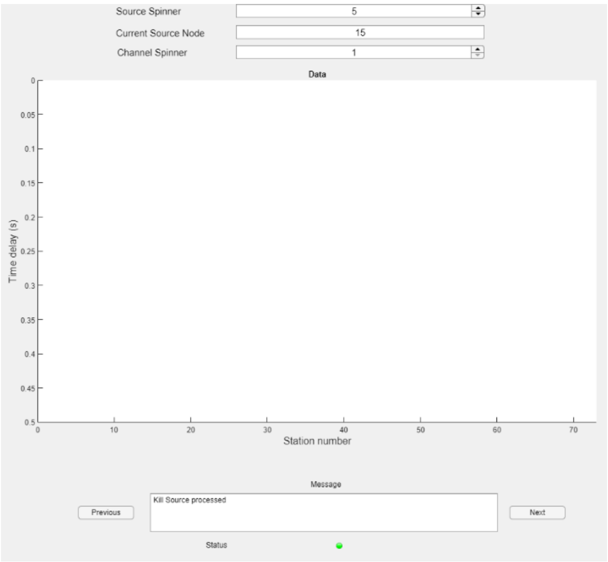

Source Spinner 5
Current Source Node 15
Channel Spinner 1

Message: Kill Source processed

Figure 16. Kill source

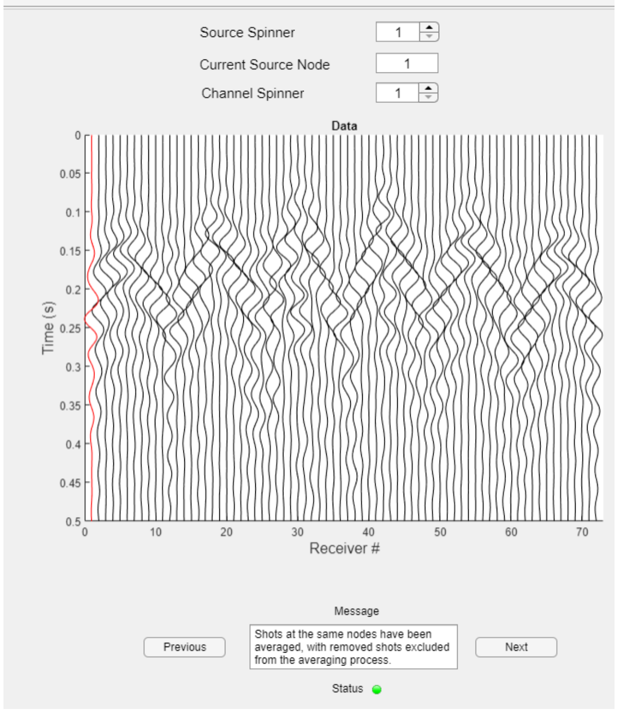

Source Spinner 1
Current Source Node 1
Channel Spinner 1

Message: Shots at the same nodes have been averaged, with removed shots excluded from the averaging process.

Figure 17. Average source

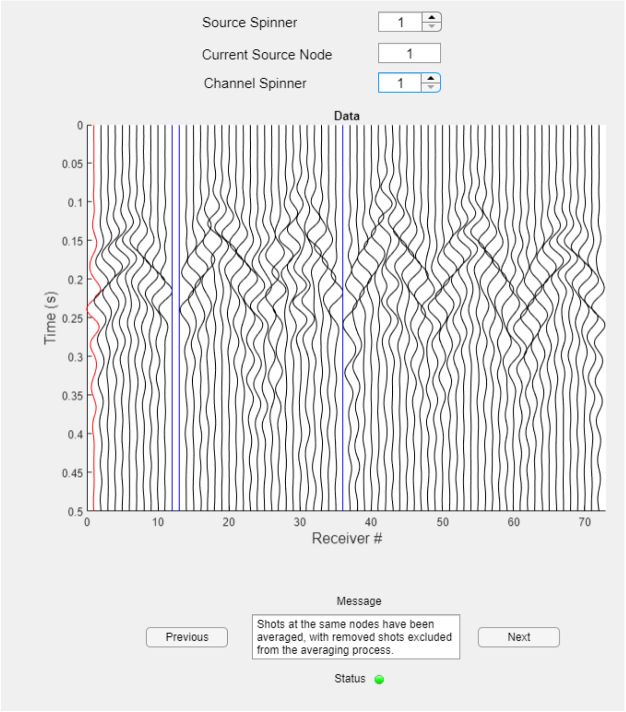

Source Spinner 1
Current Source Node 1
Channel Spinner 1

Message: Shots at the same nodes have been averaged, with removed shots excluded from the averaging process.

Figure 18. Kill trace (blue channels are removed)

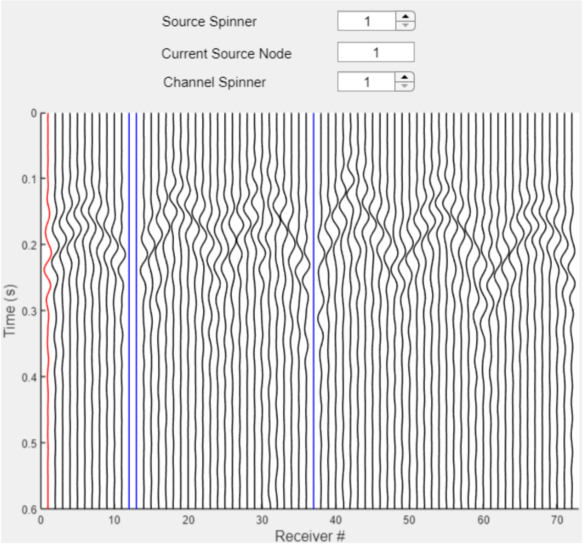

Source Spinner 1
Current Source Node 1
Channel Spinner 1

Figure 19. Gain Balance

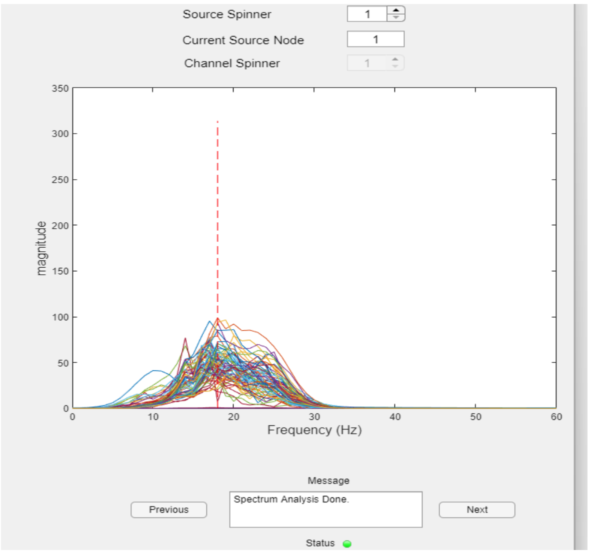

Source Spinner 1
Current Source Node 1
Channel Spinner 1

Message: Spectrum Analysis Done.

Figure 20. Check the Spectrum

6. Spectral Analysis

Step 4 of the 3D SWT analysis is to do spectral analysis. It is optional and can be skipped if the initial model is already known (e.g., reprocessing). This step is to determine the range of S-wave velocity used in the initial model. To do this, choose either:

1. **Settings > Spec Analysis.**
2. **Click the "Next" button in the "Step 3" tab.**
3. **Click the "Step 4" button in the "Step 3" tab.**

This action will bring up a tab as shown in Figure 21.

To do this analysis, follow the steps below:

1) Click **"Open Surface Data**", which triggers a "Select File to Open" window.

2) Select Channels: Enter values for Channels start and Channels end, and then click "**Select**" button. For example, select the first 12 channels (see Figure 22). Only one line of geophones is used for this analysis.

3) Click "**Up sampling**" button to up sample the raw data if necessary. For example, up-sampling twice, the 12 traces will become 48 traces (Figure 23).

4) Data is sometimes backwards with respect to receiver numbers (Figure 24), due to cable looping in the field. To fix it, simply click the **“Flip”** button (Figure 24), to make sure travel time increases with channel numbers as shown in Figure 22.

5) Enter values for “**Velocity max**” and “**Frequency max**” parameters (for analyzing and plotting), where “Velocity max” and “Frequency max” are the maximum velocity and frequency, respectively. For example, we set “Velocity max” as 1000m/s, and “Frequency max” as 30 Hz.

6) Click “**Analyze**” to generate the dispersion curve and the status bar changes to “Running Spectral Analysis”. The status lamp will display yellow, and the gauge will show the calculation progress (see Figure 26).

After completing the Spectral Analysis, use the results to generate a reasonable initial model (refer to the next section).

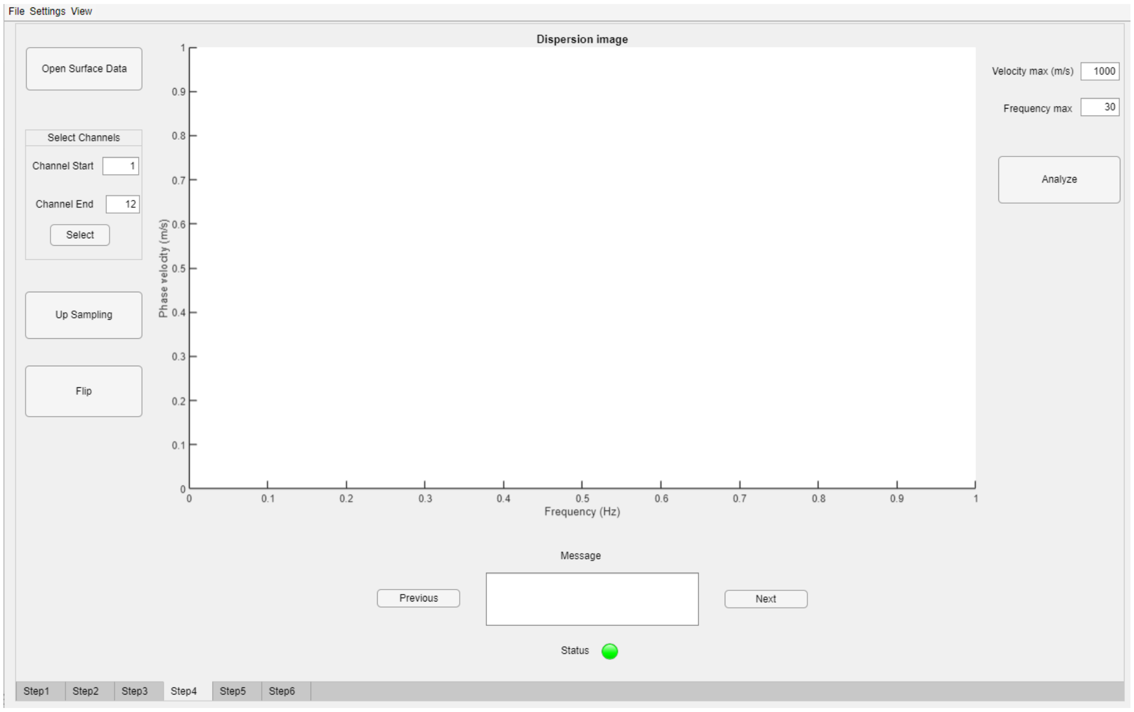

Channel Start 1

Channel End 12

Velocity max (m/s) 1000

Frequency max 30

Figure 21. Dispersion image.

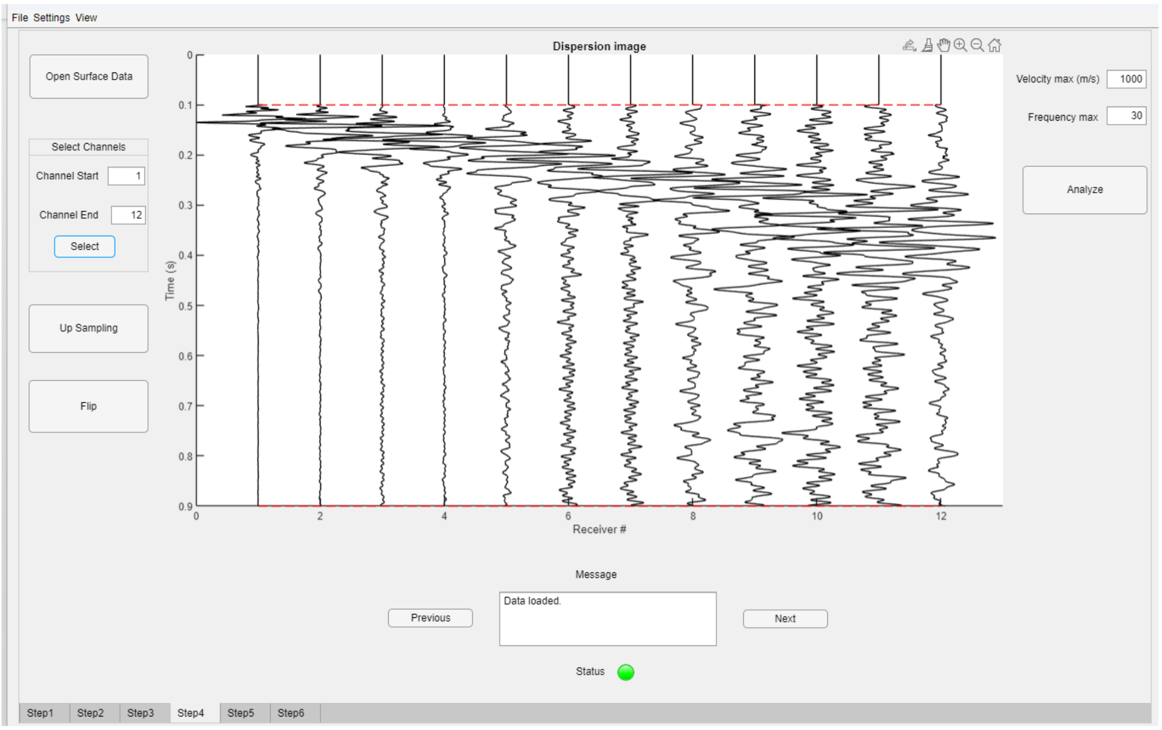

Channel Start 1

Channel End 12

Velocity max (m/s) 1000

Frequency max 30

Message: Data loaded.

Figure 22. Select channels

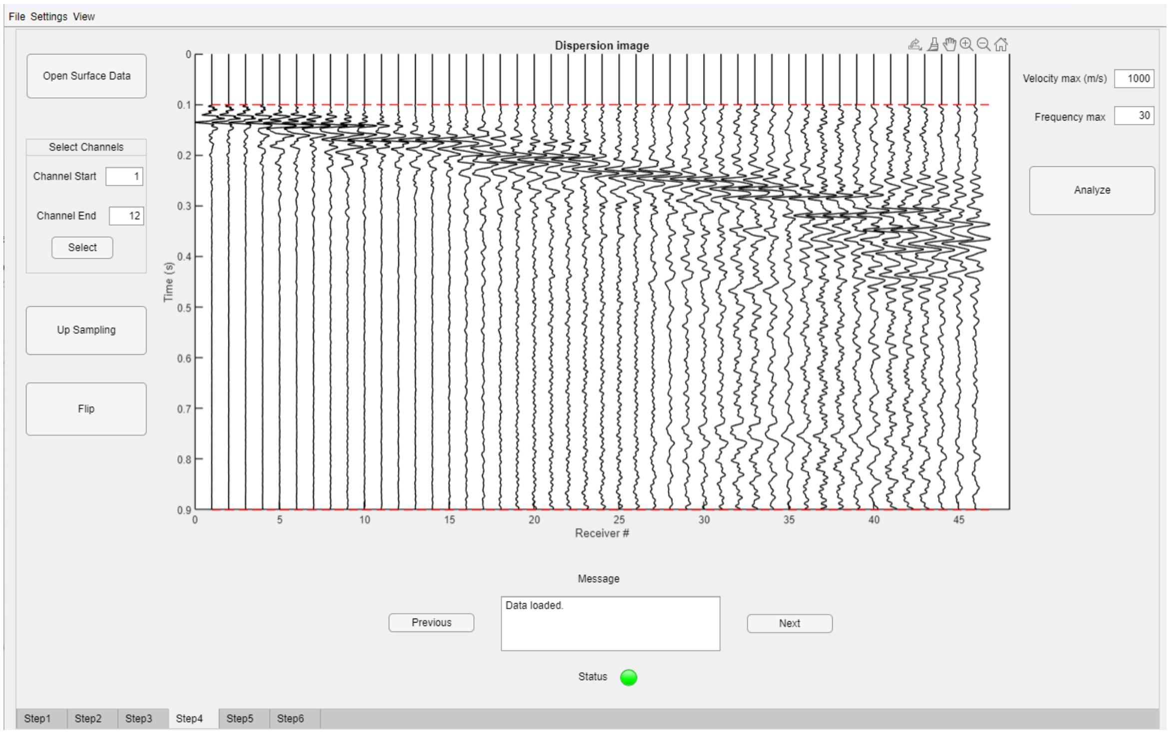

Channel Start 1

Channel End 12

Velocity max (m/s) 1000

Frequency max 30

Message: Data loaded.

Figure 23. Up sampling

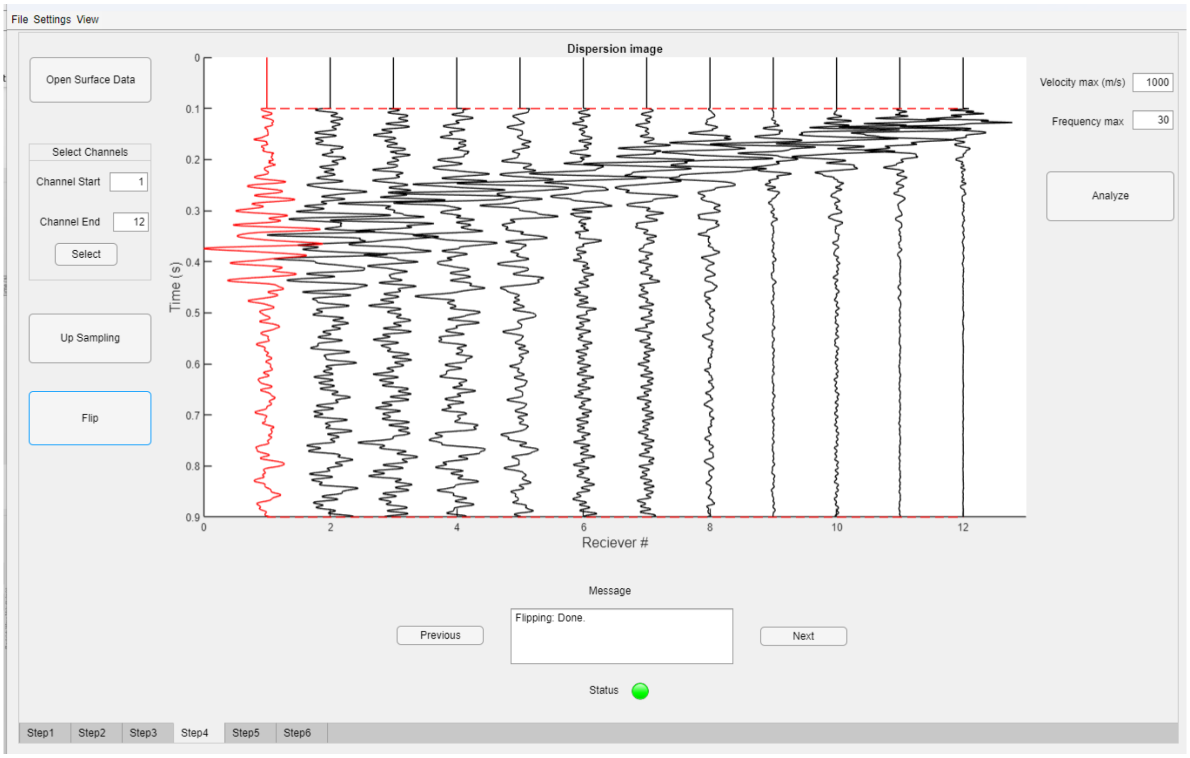

Channel Start 1

Channel End 12

Velocity max (m/s) 1000

Frequency max 30

Flipping: Done.

Figure 24. Flip data

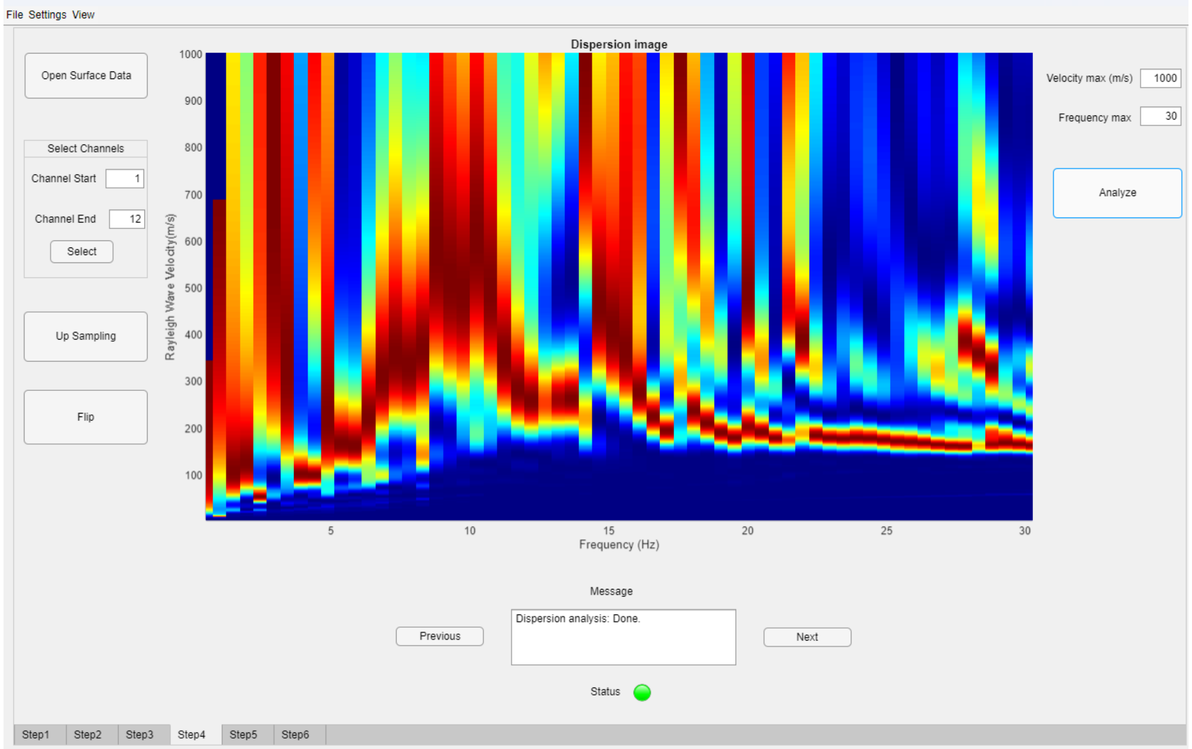

Channel Start 1

Channel End 12

Velocity max (m/s) 1000

Frequency max 30

Dispersion analysis: Done.

Figure 25. Calculated dispersion image

7. Initial model

Step 5 of the 3D SWT analysis is to generate the initial model. To do this, choose either:

1. **Settings > Initial Model**
2. **Click the "Next" button in the "Step 4" tab.**
3. **Click the "Step 5" button in the "Step 4" tab.**

Then:

a) Input S-wave velocity at the surface (V_s top) and the bottom (V_s btm). V_s at the bottom must be larger or equal V_s top.

b) Click "**Generate**" button to generate the initial model (Figure 26).

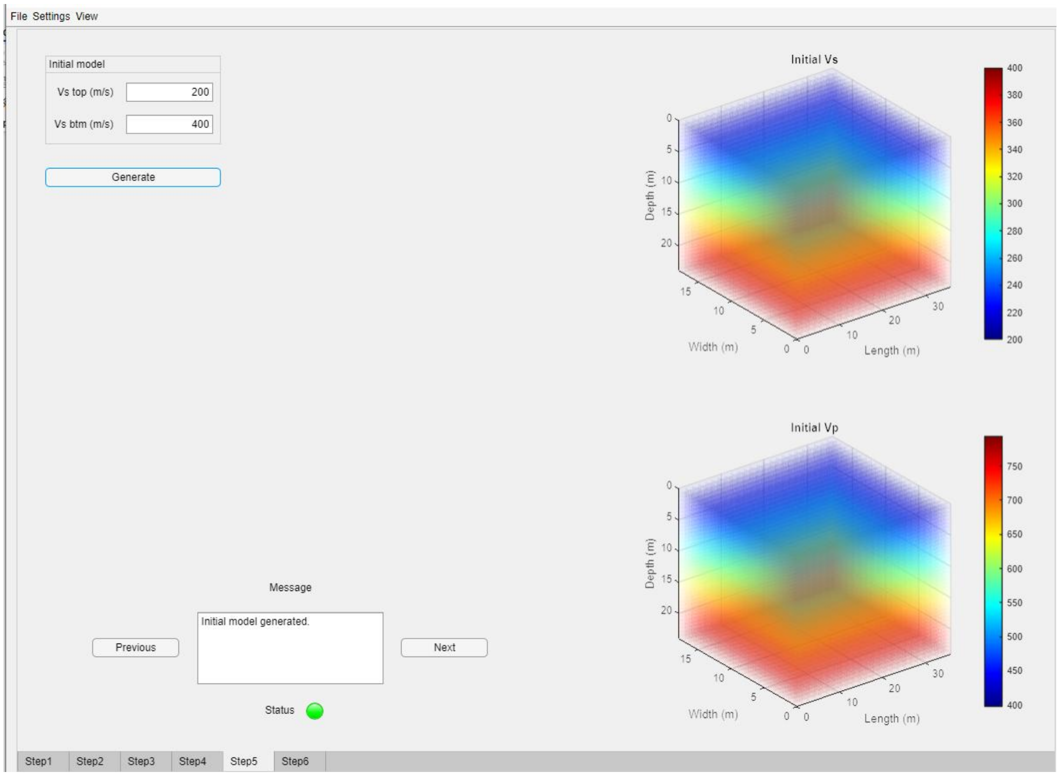

Initial model

Vs top (m/s) 200

Vs btm (m/s) 400

Message

Initial model generated.

Figure 26. Initial model for S- and P-wave velocities.

8. Inversion

The final step (Step 6) of the 3D SWT analysis is to invert data for V_s and V_p profiles. The inversion process combines all previous aspects of the user interface including the parameters, imported data, and initial model. V_s and V_p models are updated iteratively by matching the synthetic data with the field data, and the final V_s and V_p models are created when the inversion is complete. Also, the estimated source, Errors, and Waveform comparisons are plotted for each iteration.

To do this, choose either:

1. **Settings > Inversion**
2. **Click the "Next" button in the "Step 5" tab.**
3. **Click the "Step 6" button in the "Step 5" tab.**

Which will navigate to the inversion page (Figure 27).

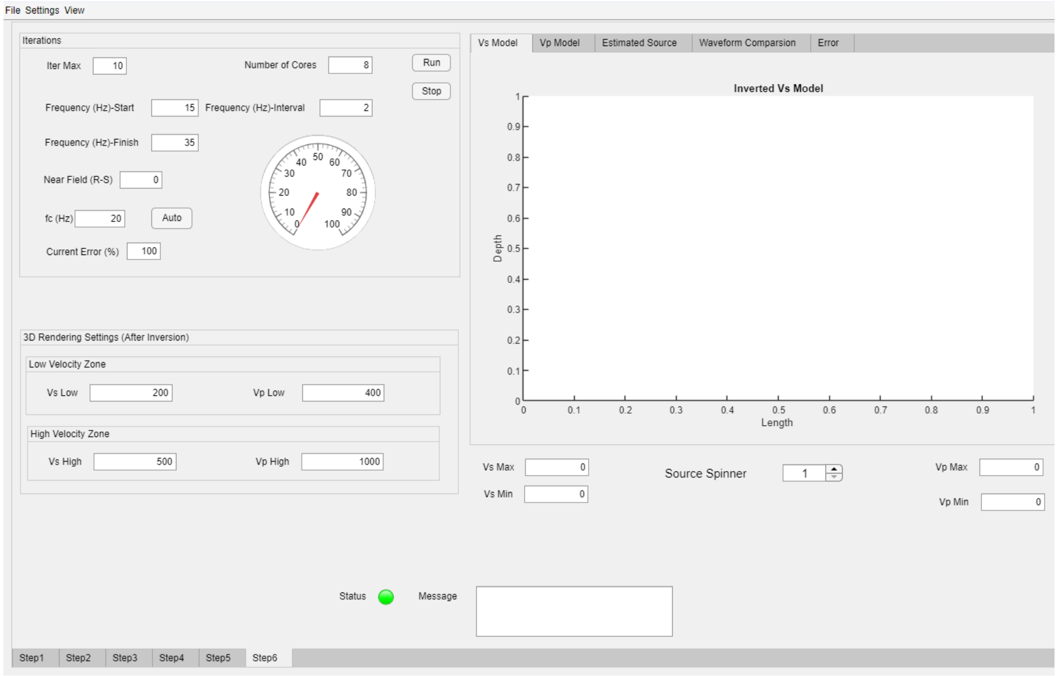

Iter Max 10
Number of Cores 8
Frequency (Hz)-Start 15
Frequency (Hz)-Interval 2
Frequency (Hz)-Finish 35
Near Field (R-S) 0
fc (Hz) 20
Current Error (%) 100
Vs Low 200
Vp Low 400
Vs High 500
Vp High 1000
Vs Max 0
Vs Min 0
Source Spinner 1
Vp Max 0
Vp Min 0

Figure 27. Inversion page

As shown in Figure 27, do the following:

1) In the "**Iterations**" box: Enter the maximum number of iterations (Iter max)

2) Enter the number of cores, ensuring it does not exceed your computer's core count.

3) In the "**Filter**" box: Enter 3 values: Frequency Start, Frequency Interval, and Frequency Finish. Shown in the example (Figure 28), the filtering frequencies are 15 to 35 Hz with 2 Hz frequency intervals. It is wort noting that we simulate the forward modeling waveform in time domain but implement the inversion in the frequency domain to save RAM. These specified frequencies will be used for inversion.
4) Enter near-field distance **(R_nf)** to account for material damping if needed. Default value is 0.
5) Enter the center frequency of filtered data **fc**. Or click the Auto button, which will set the center frequency automatically according to the mean center frequency of filtered data.
6) To do the inversion analysis, click **"Run"** button.
7) To stop the inversion analysis, click **"Stop"** button.

Inverted V_s, V_p, waveform comparison, and error value for each iteration will be displayed during inversion and at the end (Figure 28-31). Throughout the inversion process, the software will provide insights such as inverted V_s and V_p values, waveform comparisons, estimated source, and error values for each iteration. You can monitor these results to assess the inversion's progress and quality.

The **"V_s Max"** box displays the maximum value of the inverted shear wave velocity (Vs_max), while the **"V_s Min"** box shows its minimum value (Vs_min). Similarly, the **"V_p Max"** box indicates the maximum value of the inverted compressional wave velocity (Vp_max), and the **"V_p Min"** box reflects its minimum value (Vp_min).

After completing the inversion, you can adjust the 3D rendering to highlight low and high velocity zones.

1) By editing the **"V_s Low"** box, you can make the low-velocity zone (less than Vs_Low) visible. Similarly, by editing the **"V_s High"** box, you can enhance visibility of the high-velocity zone (more than V_s High).
2) For P-wave velocity, editing the **"V_p Low"** box shows the low-velocity zone (less than Vp_Low), while editing the **"V_p High"** box shows the high-velocity zone (more than Vp_High).

This customization allows for clearer visualization of specific velocity zones in your 3D model.

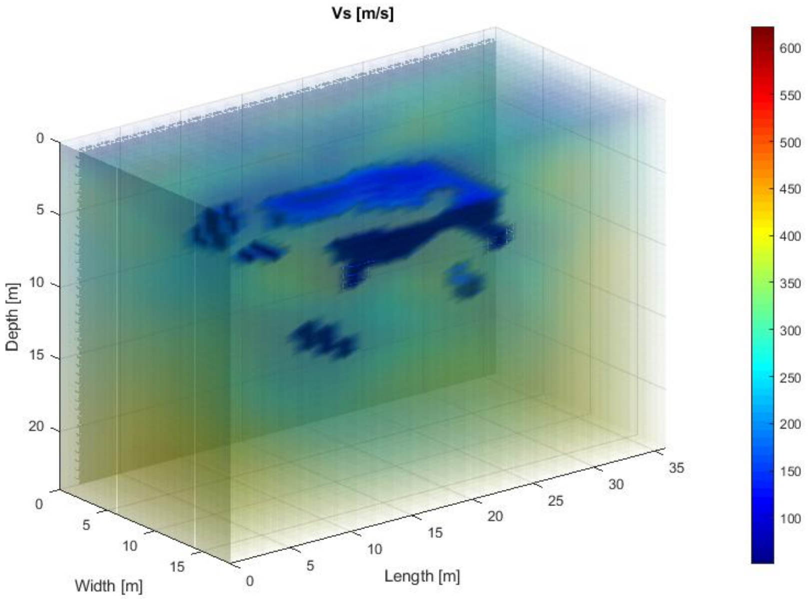

Figure 28. Inverted V_s

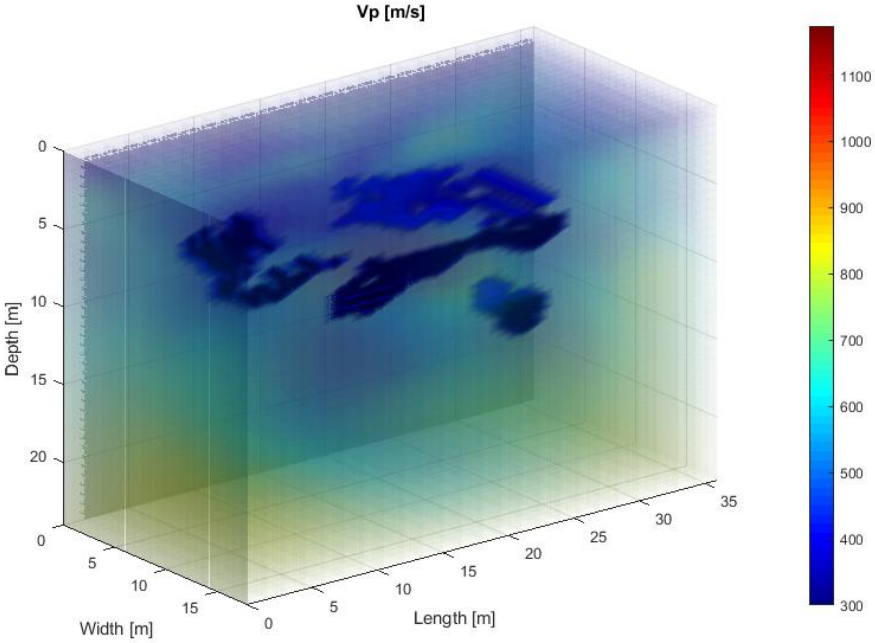

Figure 29. Inverted V_p

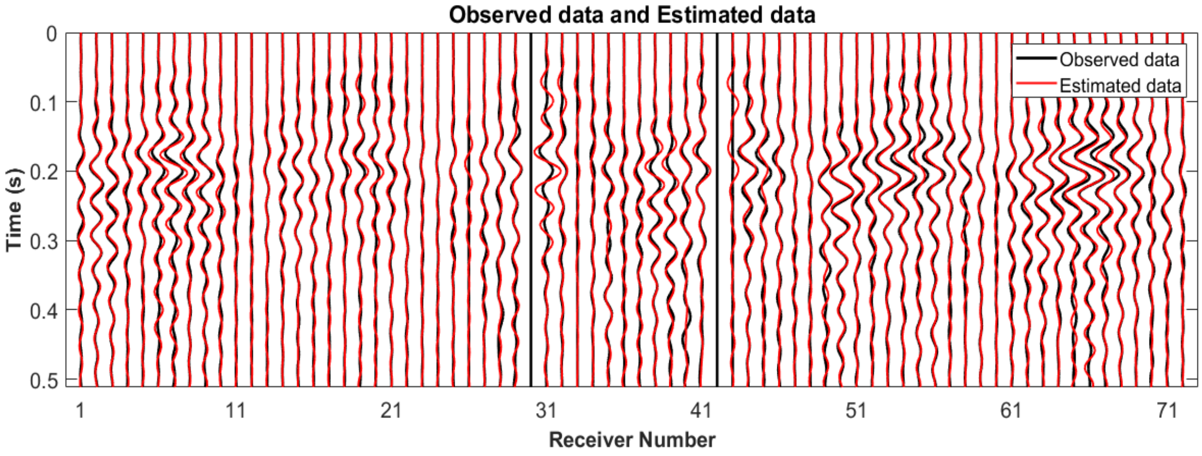

Figure 30. Waveform comparison

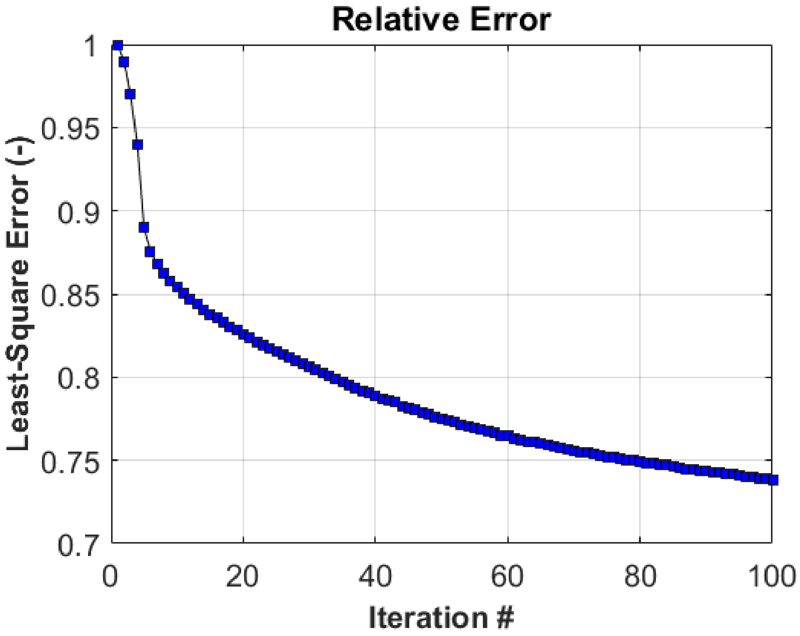

Figure 31. Error

9. Save and Export

9.1 Save: Geometry or Project

To create a parameter file that can later be imported, select **File>Save>Geometry/Project.**

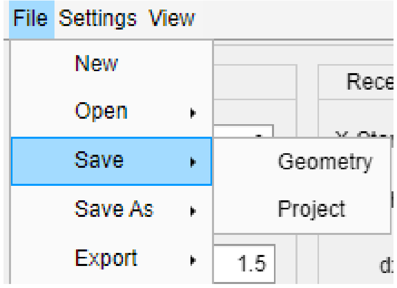

Figure 32. Save parameters

The following dialogue box allows for selection of a location and file name for the parameters.

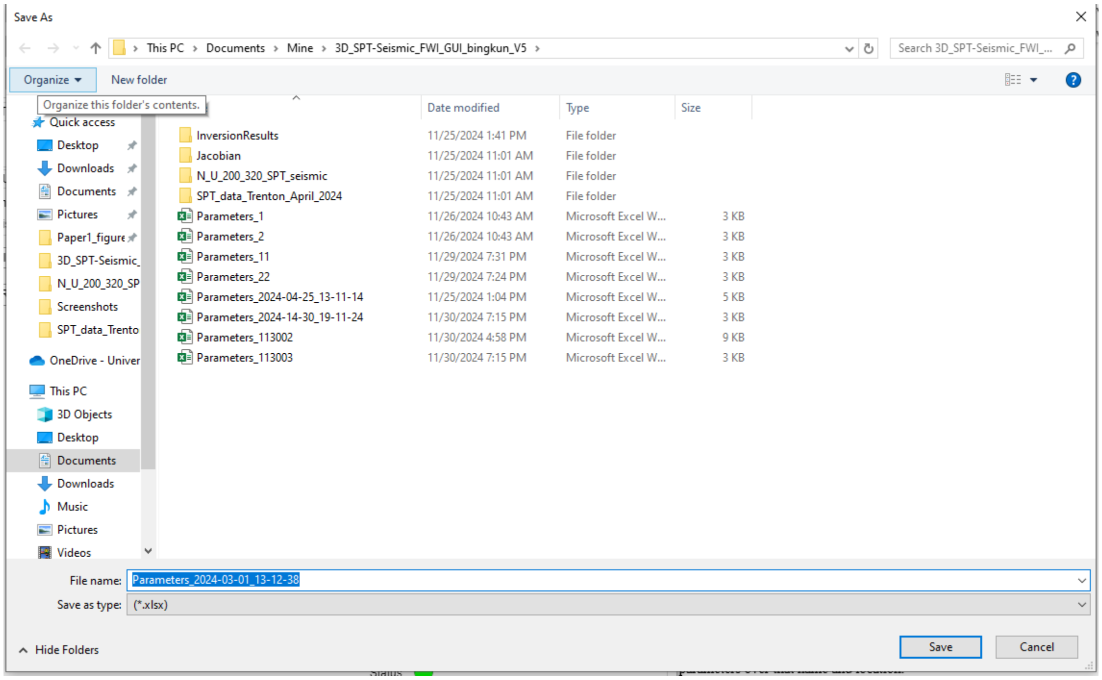

	Date modified	Type	Size
InversionResults	11/25/2024 1:41 PM	File folder	
Jacobian	11/25/2024 11:01 AM	File folder	
N_U_200_320_SPT_seismic	11/25/2024 11:01 AM	File folder	
SPT_data_Trenton_April_2024	11/25/2024 11:01 AM	File folder	
Parameters_1	11/26/2024 10:43 AM	Microsoft Excel W...	3 KB
Parameters_2	11/26/2024 10:43 AM	Microsoft Excel W...	3 KB
Parameters_11	11/29/2024 7:31 PM	Microsoft Excel W...	3 KB
Parameters_22	11/29/2024 7:24 PM	Microsoft Excel W...	3 KB
Parameters_2024-04-25_13-11-14	11/25/2024 1:04 PM	Microsoft Excel W...	5 KB
Parameters_2024-14-30_19-11-24	11/30/2024 7:15 PM	Microsoft Excel W...	3 KB
Parameters_113002	11/30/2024 4:58 PM	Microsoft Excel W...	9 KB
Parameters_113003	11/30/2024 7:15 PM	Microsoft Excel W...	3 KB

File name: Parameters_2024-03-01_13-12-38
Save as type: (*.xlsx)

Figure 33. Save Geometry file (*.xlsx).

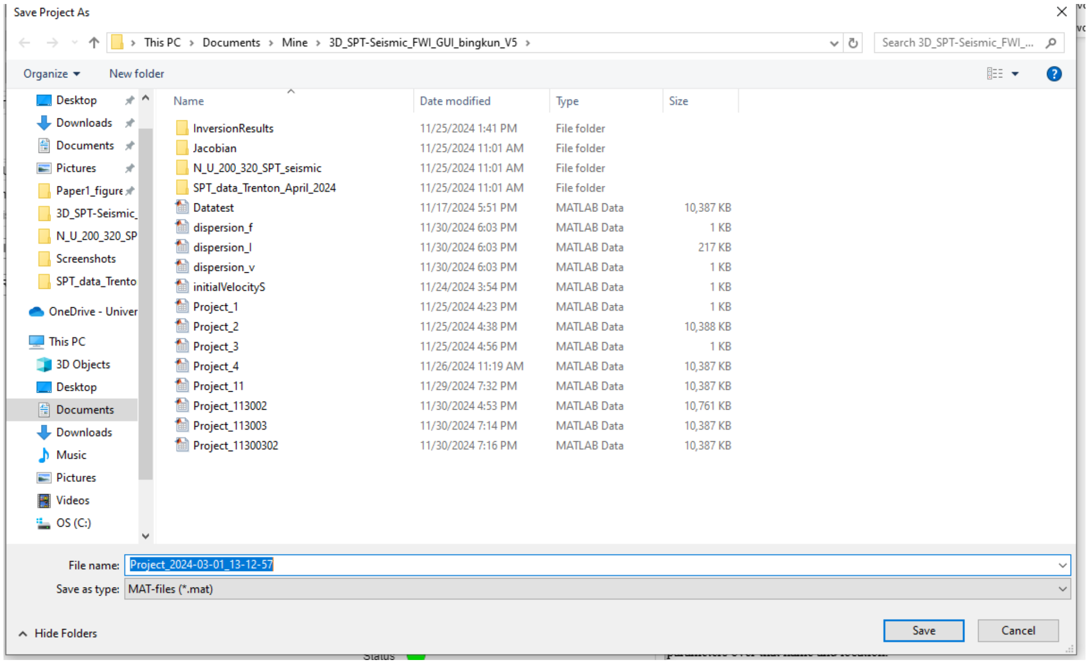

Name	Date modified	Type	Size
InversionResults	11/25/2024 1:41 PM	File folder	
Jacobian	11/25/2024 11:01 AM	File folder	
N_U_200_320_SPT_seismic	11/25/2024 11:01 AM	File folder	
SPT_data_Trenton_April_2024	11/25/2024 11:01 AM	File folder	
Datatest	11/17/2024 5:51 PM	MATLAB Data	10,387 KB
dispersion_f	11/30/2024 6:03 PM	MATLAB Data	1 KB
dispersion_l	11/30/2024 6:03 PM	MATLAB Data	217 KB
dispersion_v	11/30/2024 6:03 PM	MATLAB Data	1 KB
initialVelocityS	11/24/2024 3:54 PM	MATLAB Data	1 KB
Project_1	11/25/2024 4:23 PM	MATLAB Data	1 KB
Project_2	11/25/2024 4:38 PM	MATLAB Data	10,388 KB
Project_3	11/25/2024 4:56 PM	MATLAB Data	1 KB
Project_4	11/26/2024 11:19 AM	MATLAB Data	10,387 KB
Project_11	11/29/2024 7:32 PM	MATLAB Data	10,387 KB
Project_113002	11/30/2024 4:53 PM	MATLAB Data	10,761 KB
Project_113003	11/30/2024 7:14 PM	MATLAB Data	10,387 KB
Project_11300302	11/30/2024 7:16 PM	MATLAB Data	10,387 KB

File name: Project_2024-03-01_13-12-57
Save as type: MAT-files (*.mat)

Figure 34. Save Project file (*.mat).

If a Geometry/Project file location and name are already selected, the save function will overwrite it with the current parameters. Select the desired location and name and click "**Save**". Once saved, the files can be reimported using the open option (Section 3.2).

9.2 Save as: Geometry or Project

The option to save the parameters to a new file location is available by selecting **File>Save As>Geometry/Project.**

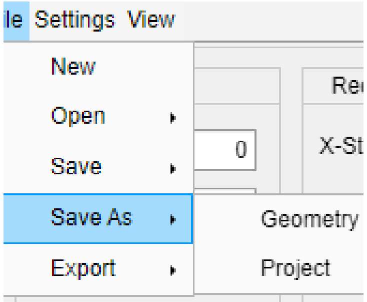

Figure 35. Save As

The below dialogue box allows for selection of a location and file name for the parameters.

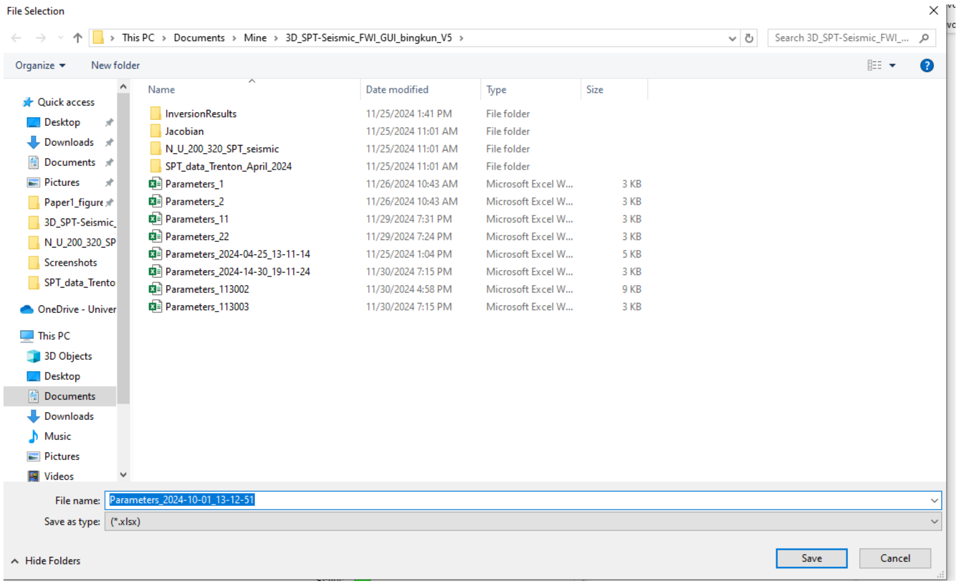

Name	Date modified	Type	Size
InversionResults	11/25/2024 1:41 PM	File folder	
Jacobian	11/25/2024 11:01 AM	File folder	
N_U_200_320_SPT_seismic	11/25/2024 11:01 AM	File folder	
SPT_data_Trenton_April_2024	11/25/2024 11:01 AM	File folder	
Parameters_1	11/26/2024 10:43 AM	Microsoft Excel W...	3 KB
Parameters_2	11/26/2024 10:43 AM	Microsoft Excel W...	3 KB
Parameters_11	11/29/2024 7:31 PM	Microsoft Excel W...	3 KB
Parameters_22	11/29/2024 7:24 PM	Microsoft Excel W...	3 KB
Parameters_2024-04-25_13-11-14	11/25/2024 1:04 PM	Microsoft Excel W...	5 KB
Parameters_2024-14-30_19-11-24	11/30/2024 7:15 PM	Microsoft Excel W...	3 KB
Parameters_113002	11/30/2024 4:58 PM	Microsoft Excel W...	9 KB
Parameters_113003	11/30/2024 7:15 PM	Microsoft Excel W...	3 KB

File name: Parameters_2024-10-01_13-12-51

Save as type: (*.xlsx)

Figure 36. Save as Geometry file (*.xlsx).

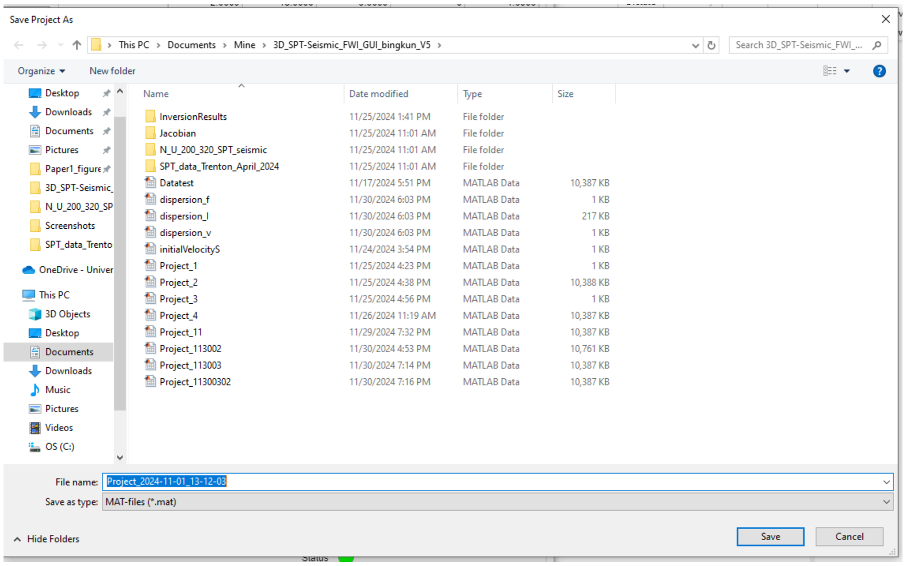

Name	Date modified	Type	Size
InversionResults	11/25/2024 1:41 PM	File folder	
Jacobian	11/25/2024 11:01 AM	File folder	
N_U_200_320_SPT_seismic	11/25/2024 11:01 AM	File folder	
SPT_data_Trenton_April_2024	11/25/2024 11:01 AM	File folder	
Datatest	11/17/2024 5:51 PM	MATLAB Data	10,387 KB
dispersion_f	11/30/2024 6:03 PM	MATLAB Data	1 KB
dispersion_l	11/30/2024 6:03 PM	MATLAB Data	217 KB
dispersion_v	11/30/2024 6:03 PM	MATLAB Data	1 KB
initialVelocityS	11/24/2024 3:54 PM	MATLAB Data	1 KB
Project_1	11/25/2024 4:23 PM	MATLAB Data	1 KB
Project_2	11/25/2024 4:38 PM	MATLAB Data	10,388 KB
Project_3	11/25/2024 4:56 PM	MATLAB Data	1 KB
Project_4	11/26/2024 11:19 AM	MATLAB Data	10,387 KB
Project_11	11/29/2024 7:32 PM	MATLAB Data	10,387 KB
Project_113002	11/30/2024 4:53 PM	MATLAB Data	10,761 KB
Project_113003	11/30/2024 7:14 PM	MATLAB Data	10,387 KB
Project_11300302	11/30/2024 7:16 PM	MATLAB Data	10,387 KB

File name: Project_2024-11-01_13-12-03

Save as type: MAT-files (*.mat)

Figure 37. Save as Project file (*.mat).

Select the desired location and name and click **"Save".** Once saved, the file can be reimported using the open option (Section 3.2).

9.3 Export

To export inversion results, navigate to **File > Export > Inverted V_s/Inverted V_p/Waveform Comparison/Error** (Figure 38). This allows you to generate an image file of the current display. Alternatively, you can export the Inverted V_s, Inverted V_p, or Error data in *.xlsx format. Simply click the desired option, then choose the file location, name, and type to complete the export process.

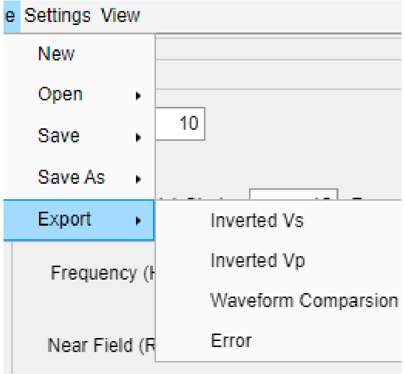

Figure 38. Export image file.